

TECHNISCHE  
UNIVERSITÄT  
DRESDEN

---

# Timing Resistive Plate Chambers with Ceramic Electrodes

for Particle and Nuclear Physics Experiments

Dissertation  
zur Erlangung des wissenschaftlichen Grades  
Doktor rerum naturalium (Dr. rer. nat.)

vorgelegt von

Alejandro Laso García  
geboren am 20.06.1987 in Ferrol, Spanien

Fakultät Mathematik und Naturwissenschaften  
der Technischen Universität Dresden  
2014

Eingereicht am 15.10.2014  
Verteidigt am 9.2.2015

1. Gutachter: Prof. Dr. Eckart Grosse
2. Gutachter: Prof. Dr. Burkhard Kämpfer
3. Gutachter: Prof. Dr. Norbert Herrmann

## Abstract

The focus of this thesis is the development of Resistive Plate Chambers (RPCs) with ceramic electrodes. The use of ceramic composites,  $\text{Si}_3\text{N}_4/\text{SiC}$ , opens the way for the application of RPCs in harsh radiation environments. Future Experiments like the Compressed Baryonic Matter (CBM) at the Facility for Antiproton and Ion Research (FAIR) in Darmstadt will need new RPCs with high rate capabilities and high radiation tolerance.

Ceramic composites are specially suited for this purpose due to their resistance to radiation and chemical contamination. The bulk resistivity of these ceramics is in the range  $10^7 - 10^{13} \Omega \text{ cm}$ . The bulk resistivity of the electrodes is the main factor determining the rate capabilities of an RPC, therefore a specific measuring station and a measurement protocol has been set for these measurements. The dependence of the bulk resistivity on the different steps of the manufacturing process has been studied. Other electrical parameters like the relaxation time, the relative permittivity and the tangent loss have also been investigated.

Simulation codes for the investigation of RPC functionality was developed using the gas detectors simulation framework GARFIELD++. The parameters of the two mixtures used in RPC operation have been extracted. Furthermore, theoretical predictions on time resolution and efficiency have been calculated and compared with experimental results.

Two ceramic materials have been used to assemble RPCs.  $\text{Si}_3\text{N}_4/\text{SiC}$  and  $\text{Al}_2\text{O}_3$  with a thin (nm thick) chromium layer deposited over it. Several prototypes have been assembled with active areas of  $5 \times 5 \text{ cm}^2$ ,  $10 \times 10 \text{ cm}^2$  and  $20 \times 20 \text{ cm}^2$ . The number of gaps ranges from two to six. The gas gap widths were  $250 \mu\text{m}$  and  $300 \mu\text{m}$ . As separator material mylar foils, fishing line and high-resistive ceramics have been used. Different detector architectures have been built and their effect on RPC performance analysed.

The RPCs developed at HZDR and ITEP (Moscow) were systematically tested in electron and proton beams and with cosmic radiation over the course of three years. The performance of the RPCs was extracted from the measured data. The main parameters like time resolution, efficiency, rate capabilities, cluster size, detector currents and avalanche charge were obtained and compared with other RPC systems in the world. A comparison with phenomenological models was performed.

RPCs with an active area of  $10 \times 10 \text{ cm}^2$ , four gaps with  $300 \mu\text{m}$  width per gap and  $10^9 \Omega \text{ cm}$  show an efficiency of 95% up to a flux of  $4 \times 10^5 \text{ cm}^{-2} \text{ s}^{-1}$ . A time resolution better than 100 ps was achieved for the same fluxes. RPCs with an active area of  $20 \times 20 \text{ cm}^2$ , four gaps of  $250 \mu\text{m}$  width per gap and  $10^{10} \Omega \text{ cm}$  present an efficiency of 90% up to fluxes of  $6 \times 10^4 \text{ cm}^{-2} \text{ s}^{-1}$  with a time resolution of 65 ps for the same fluxes.

These results prove that RPCs fulfil the requirements of the CBM Time-of-Flight Wall. In addition, the exceptional performance of RPCs is specially attractive for future accelerator projects and medical purposes.

The results shown in this work represent to date the highest incoming particle fluxes under which an RPC can work.

## Zusammenfassung

Der Schwerpunkt dieser Arbeit ist die Entwicklung und Charakterisierung von Widerstandsplattenzählern (RPCs) mit Keramik-elektroden. Die Verwendung von keramischen Verbundwerkstoffens  $\text{Si}_3\text{N}_4/\text{SiC}$  ermöglicht den Einsatz der RPCs als ratenfeste Flugzeitdetektoren. Das "Compressed Baryonic Matter" (CBM) Spektrometer an der "Facility for Antiproton and Ion Research" (FAIR) in Darmstadt macht den Einsatz ratenfester und strahlungstoleranter RPCs mit exzellenter Zeitauflösung von besser als 100 ps ( $\sigma$ ) sowie hohem Ansprechwahrscheinlichkeit von über 95% notwendig.

Halbleitende Keramik-Verbundwerkstoffe sind im Gegensatz zu Normalglas speziell für diesen Zweck als Elektrodenmaterial geeignet. Sie haben hervorragende Beständigkeit gegenüber ionisierender Strahlung und chemischen Verunreinigungen. Der spezifische Widerstand der Elektroden ist ein wesentlicher Parameter, welcher die Ratendestigkeit des RPC beeinflusst und durch Variation des Herstellungsprozesses im Bereich von  $10^7$  bis  $10^{13} \Omega \text{ cm}$  eingestellt werden kann. Die Änderung der spezifischen Widerstandes in Abhängigkeit von den Prozessparametern wurde an einem dezidierten Messplatz für keramische Proben untersucht. Weitere elektrische Parameter wie die Relaxationszeit, die relative Dielektrizitätskonstante und der Dielektrizitätsverlust wurden ebenfalls untersucht.

Die Funktionalität der Detektoren wurde mit dem Programmpaket GARFIELD++ für verschiedene Gasmischungen simuliert und mit den experimentellen Ergebnissen verglichen. Es besteht eine hinreichende Übereinsimmung der experimentelle Ergebnisse und der Modellrechnungen sowohl für die Zeitauflösung als auch für das Ansprechverhalten.

Mit dem halbleitenden keramischen Verbundwerkstoff  $\text{Si}_3\text{N}_4/\text{SiC}$  wurden RPCs mit aktiven Durchdringungsflächen von  $5 \times 5 \text{ cm}^2$ ,  $10 \times 10 \text{ cm}^2$  und  $20 \times 20 \text{ cm}^2$  sowie mit zwei bis sechs strahlungssensitiven Gasspalten getestet. Verschieden Detektorstrukturen wurden realisiert und ihre einsatztauglichkeit getestet. Hierbei kamen auch  $\text{Al}_2\text{O}_3$ -Keramikplatten mit einer Chromschicht als Electrode zur Anwendung.

Die am HZDR und in Zusammenarbeit mit ITEP (Moskau) entwickelten Detektoren wurden systematisch mit Elektronen- und Protonenstrahlen getestet. Wichtige Detektorparameter wie Zeitauflösung, Ansprechverhalten, Ratenfestigkeit, Cluster-Größe, Detektorstrom und Lawinenladung wurden bestimmt und mit anderen aus der Literatur bekannten Ergebnissen verglichen.

Keramik RPCs (CRPCs) mit einer aktiven Fläche von  $10 \times 10 \text{ cm}^2$ , vier Gasspalten mit je  $300 \mu\text{m}$  Spaltbreite und einem spezifische Widerstand der Keramik von  $10^9 \Omega \text{ cm}$  zeigen ein Wirkungsgrad der Ansprechverhaltens von 95% bei Flüßens von bis zu  $4 \times 10^5 \text{ cm}^{-2} \text{ s}^{-1}$ . Eine Zeitauflösung besser als 100 ps wurde für dieselben Flüße erreicht. Bei CRPCs mit einer aktiven Fläche von  $20 \times 20 \text{ cm}^2$ , vier Spalten von  $250 \mu\text{m}$  breite und spezifische Widerstand der Keramik von  $10^{10} \Omega \text{ cm}$  wurde ein Ansprechverhalten von 90% und eine Zeitauflösung von 65 ps bei Flüßen von bis zu  $6 \times 10^4 \text{ cm}^{-2} \text{ s}^{-1}$  bestimmt.

Diese Ergebnisse beweisen, dass CRPCs die Anforderungen der CBM-Flugzeitwand erfüllen. Darüber hinaus werden CRPC-Prototypen speziell bei medizinische Bestrahlungsanwendungen für die in-vivo-dosimetrie mit Photonenstrahlen getestet.

Die Ergebnisse in dieser Arbeit zeigt, dass die betrachteten Widerstandsplattenzähler aus keramischen Elektroden im weltweiten Vergleich die bisher größte Ratenfestigkeit aufweisen.

# Contents

|  |           |
|--|-----------|
| <b>1. Introduction</b>   | <b>7</b>  |
| 1.1. Development of Resistive Plate Chambers . . . . .                                     | 7         |
| 1.2. RPCs around the world . . . . .   | 8         |
| 1.2.1. Trigger RPCs . . . . .  | 9         |
| 1.2.2. Timing RPCs . . . . .   | 9         |
| 1.3. The Compressed Baryonic Matter experiment . . . . .                                   | 12        |
| 1.3.1. The Time of Flight Wall . . . . .   | 16        |
| 1.3.2. Specifications of the CBM-ToF . . . . .   | 16        |
| 1.4. Outline of this thesis . . . . .  | 18        |
| <b>2. Resistive Plate Chambers</b>   | <b>21</b> |
| 2.1. Parallel Plate Geometries . . . . .   | 21        |
| 2.2. Gas ionization by charged particles . . . . .   | 21        |
| 2.3. Avalanche formation and signal induction processes . . . . .                          | 23        |
| 2.3.1. Cluster formation . . . . .   | 23        |
| 2.3.2. Avalanche multiplication . . . . .  | 24        |
| 2.3.3. Signal induction . . . . .  | 26        |
| 2.3.4. Total charge and induced charge . . . . .   | 28        |
| 2.3.5. Signal read out . . . . .   | 28        |
| 2.3.6. Relaxation time . . . . .   | 29        |
| 2.4. Efficiency . . . . .  | 30        |
| 2.5. Time resolution and the streamer limit . . . . .                                      | 30        |
| 2.6. Rate capabilities . . . . .   | 31        |
| <b>3. Ceramic Composites for RPC Electrodes</b>  | <b>33</b> |
| 3.1. The quest for new materials . . . . .   | 33        |
| 3.2. Manufacturing process of ceramic materials . . . . .                                  | 34        |
| 3.3. Characterization of $\text{Si}_3\text{N}_4/\text{SiC}$ ceramics . . . . .             | 35        |
| 3.3.1. Mechanical properties . . . . .   | 35        |
| 3.3.2. Bulk resistivity . . . . .  | 35        |
| 3.3.3. Electrical parameters . . . . .   | 46        |
| 3.3.4. Radiation hardness . . . . .  | 48        |
| 3.4. Characterization of $\text{Al}_2\text{O}_3$ ceramics . . . . .                        | 49        |
| <b>4. Ceramic Detector Prototypes</b>  | <b>53</b> |
| 4.1. Dual two gap RPC with $\text{Si}_3\text{N}_4/\text{SiC}$ ceramic electrodes . . . . . | 54        |
| 4.1.1. Two-gap RPC with $\text{Al}_2\text{O}_3$ ceramic electrodes . . . . .               | 56        |

|           |  |            |
|-----------|--|------------|
| 4.1.2.    | The Rogowski profile . . . . .                                     | 56         |
| 4.1.3.    | Differential readout prototypes . . . . .                          | 62         |
| 4.2.      | Gas mixtures for ceramic RPCs . . . . .                            | 62         |
| 4.3.      | Dark current comparison . . . . .                                  | 63         |
| 4.4.      | Front End Electronics . . . . .                                    | 65         |
| 4.4.1.    | FOPI amplifying electronics . . . . .                              | 65         |
| 4.4.2.    | PADI - Preamplifier and discriminator . . . . .                    | 66         |
| <b>5.</b> | <b>In-beam Tests of CRPCs</b>                                      | <b>67</b>  |
| 5.1.      | Basic concepts of trigger systems . . . . .                        | 67         |
| 5.2.      | Test in electron beams . . . . .                                   | 68         |
| 5.2.1.    | Accelerator details . . . . .                                      | 68         |
| 5.2.2.    | Test set-up for CRPCs . . . . .                                    | 70         |
| 5.2.3.    | Electron Beam profile . . . . .                                    | 72         |
| 5.2.4.    | Systematics on the beam profile . . . . .                          | 76         |
| 5.2.5.    | Average flux estimation . . . . .                                  | 77         |
| 5.3.      | Tests in proton beams . . . . .                                    | 78         |
| 5.3.1.    | Experimental set-up . . . . .                                      | 78         |
| 5.3.2.    | Beam properties . . . . .  | 79         |
| <b>6.</b> | <b>Performance of CRPCs</b>  | <b>81</b>  |
| 6.1.      | Calculating the electric field as a function of the flux . . . . . | 81         |
| 6.2.      | Definition of parameters and conditions . . . . .                  | 83         |
| 6.2.1.    | Event definition . . . . .   | 83         |
| 6.2.2.    | Parameter definition . . . . .                                     | 84         |
| 6.2.3.    | Time-walk correction . . . . .                                     | 85         |
| 6.3.      | Currents and charges induced by avalanches . . . . .               | 85         |
| 6.4.      | Working curve . . . . .  | 86         |
| 6.4.1.    | CRPC3b . . . . .   | 86         |
| 6.4.2.    | ITEP1 and ITEP2 . . . . .  | 88         |
| 6.5.      | Rate scan . . . . .  | 89         |
| 6.5.1.    | CRPC2b . . . . .   | 89         |
| 6.5.2.    | CRPC3b . . . . .   | 91         |
| 6.6.      | Position resolution . . . . .                                      | 93         |
| 6.7.      | Cluster size . . . . .   | 95         |
| <b>7.</b> | <b>Conclusions and Outlook</b>                                     | <b>99</b>  |
| <b>A.</b> | <b>Flux estimation for non-uniform beams</b>                       | <b>103</b> |
| <b>B.</b> | <b>FEE influence in efficiency estimation</b>                      | <b>105</b> |

# 1. Introduction

Particle detection has been one of the main fields in experimental physics in the last century. Nowadays, natural and artificial radiation sources have numerous applications in basic science, medicine, industry and electricity production. Particle detectors are developed to understand and exploit the properties of this radiation.

Medicine has greatly benefited from the development of radiation detectors. Tools like x-rays and photon emission tomography are widely used to diagnose health issues. Radiation therapy is a common treatment for cancer patients. In the industry, radiation is used for material analysis, smoke detection, soil density measurement, etc., among a vast number of applications [1]. For several decades now, nuclear fission has been used for electricity production. Its main drawback, however, is the long lived radioisotopes produced. Therefore, monitoring of the radiation levels of nuclear power plants and nuclear waste storage facilities are of utmost importance.

Particle detectors have provided huge advances in the field of particle physics. Currently, hundreds of different particles are known to exist or be created in high energy particle or nuclear reactions. New ones are still being discovered like a boson predicted by the Standard Model [2, 3] recently observed in proton-proton collisions at the LHC at CERN [4]. This boson is tentatively interpreted as the Higgs boson. These discoveries supposed a challenge due to the extreme technological requirements imposed by high precision measurements. Since the discovery of the first subatomic particles, the electron (Thompson, 1897), the proton (Rutherford, 1918) and the neutron (Chadwick, 1932), new and more complex techniques employed to investigate the subatomic world have been developed.

Nowadays, insight into the tiniest parts of the Universe is obtained by the use of the largest and most complex machines ever developed by mankind. Large particle accelerators provide the environment to study elemental particles, their nature and their interactions. The effects of these interactions are determined through measurements done by particle detectors. These installations require investments of hundreds of millions of Euro and years of planning. Thus, detector developments have not only focused on obtaining the best performance possible but also on building the most affordable detector. It is in the spirit of good performance and low economical requirements that Resistive Plate Chambers (RPCs) have become widely spread in high energy physics.

## 1.1. Development of Resistive Plate Chambers

Resistive Plate Chambers were inspired by parallel plate chambers (PPCs). In 1981, Santonico and Cardarelli showed that substituting the metallic plates in a PPC by a high-resistive material reduced the sparks and confined the avalanches to local discharges [5]. The material chosen was bakelite painted with a linseed oil-based semiconductor paint

with a bulk resistivity of  $10^{10} - 10^{11} \Omega \text{ cm}$ . The realization of the detector was extremely simple. The two bakelite plates were placed parallel with respect to each other and kept separated by a rectangular frame of polyvinyl chloride (PVC) with a thickness of 1.5 mm. Conductive foils were pasted to the outside faces of the electrodes. A uniform electric field was established by applying high voltage (10 kV) to these foils. A gas mixture of argon and iso-butane (50%/50%) at normal pressure circulated through the gap between the electrodes. This simple detector showed a 97% efficiency and about 1 ns time resolution when exposed to cosmic radiation. In a later paper [6], they presented the performance of a double layered RPC with an improved time resolution.

The efficiency in this kind of detector is dependant on the number of primary ionization clusters generated by the incoming charged particles and the amplification of the signal. Therefore, a wide gap RPC (with a gap in the order of mm) can be operated at an electric field of a few tens of kV/cm without losing efficiency. However, the variation on the position of the primary ionization introduces an additional time uncertainty. Thus, a wide gap RPC has limited time resolution, typically in the order of nanoseconds. The reduction of the gas gap leads to an improved time resolution. However, a reduced gas gap also means a decreased detector efficiency and lower induced charge, making necessary the use of special amplification electronics to read out the signals.

A multi-gap RPC was later developed [7], inspired by the previously existing multi-gap PPC. The multi-gap described in [7] had three gas gaps of 3 mm width each instead of a single 9 mm gap. The efficiency was close to 100% while the time resolution was 4 ns. This detector presented multiple gaps in the same RPC. The charged particle crossing the detector generated an ionisation in one or more of the gaps and the combined induced signal generated by the avalanches in each of the gaps was read. This meant that, while the signals generated by each avalanche independently were not enough to cross a certain threshold, the combined induced signal did. This development opened the way to sub-mm gap RPCs with efficiency close to 100% (due to the increased number of gaps) and time resolution in the order of hundreds of picoseconds (due to the small gap size).

## 1.2. RPCs around the world

RPCs have been present, and are still present, in many large-scale experiments around the world. Their spread can be attributed to several factors: *i*) they present a cheap alternative to other detection methods like scintillating detectors, thanks to the commercially available materials (normal silica glass for the electrodes and fishing line for spacing), *ii*) they have a simple mechanical structure that allows for an easy assembly and most importantly *iii*) their high efficiency and good time resolution fulfil the technical requirements of many experiments. Therefore, RPCs present a suitable architecture to build large area detectors subjected to low particle fluxes.

In the following, a summary of large-scale RPC systems is presented.



### 1.2.1. Trigger RPCs

Trigger RPCs are wide-gap detectors used for triggering purposes. Depending on the incoming particle rate, they can be used in streamer mode in low-rate experiments or in avalanche mode when the rate is higher. A trigger RPC is characterized by its wide gap (1-3 mm) and high charges contained in the discharge in the order of hundreds of pC [8]. The timing resolution of this kind of RPC is in the nanosecond scale, due to the gap width. The high charges collected in streamer mode make the usage of trigger RPCs easy, as no special amplification electronics is needed to detect the signals.

Trigger RPCs are used in several running CERN experiments like ATLAS [9], CMS [10] and ALICE [11]. They have also been used in previous experiments like L3 [12] at LEP.

#### ATLAS Muon Trigger

A Torodial LHC Apparatus, ATLAS, is one of the four main experiments at the Large Hadron Collider (LHC) at CERN. Its main goal is to investigate head-on proton collisions at high energies. The detector is arranged in a barrel configuration (see Figure 1.1) with the Muon Spectrometer comprised of Resistive Plate Chambers covering the outermost part of it [13, 14]. RPCs are used to fulfil the requirements of high efficiency ( $\sim 97\%$ ), time resolution of  $\sim 2-3$  ns, rate capabilities of  $\sim 100$  cm<sup>-2</sup>s<sup>-1</sup> and a measurement of the azimuthal coordinate with a spatial resolution of 5-10 mm. These RPCs are built with bakelite electrodes with their internal surfaces treated with linseed oil with a bulk resistivity of  $(1-4)\times 10^{10}$   $\Omega$  cm. The gas mixture used is C<sub>2</sub>H<sub>2</sub>F<sub>4</sub>/C<sub>4</sub>H<sub>10</sub>/SF<sub>6</sub> in fractions of 94.7%/5%/0.3%.

#### ALICE Trigger

ALICE, A Large Ion Collider Experiment, is dedicated to the study of nucleus-nucleus collisions at LHC. One of the sub-detectors, the di-muon spectrometer uses RPCs operated in streamer mode. These RPCs are made of bakelite with a bulk resistivity of  $3\times 10^9$   $\Omega$  cm [16]. There are four RPC planes each with strips in the  $x$  or  $y$  direction. Thus track reconstruction is possible [17]. The time resolution of these detectors is better than 2 ns. The gas mixture is Ar/C<sub>2</sub>H<sub>2</sub>F<sub>4</sub>/i-C<sub>4</sub>H<sub>10</sub>/SF<sub>6</sub> at the percentages 50.5%/41.3%/7.2%/1.0%, for RPC streamer mode. Another gas mixture of C<sub>2</sub>H<sub>2</sub>F<sub>4</sub>/i-C<sub>4</sub>H<sub>10</sub>/SF<sub>6</sub> is used at percentages 89.5%/10%/0.5%, to operate RPCs in saturated avalanche mode. The two mixtures are used depending on the rate, their purpose being the minimization of ageing effects in long p-p collision runs [18].

### 1.2.2. Timing RPCs

With the improvement of electronics, new applications for RPCs were found. Thanks to fast amplifying electronic systems it was possible to operate RPCs in avalanche mode at reduced gas gap sizes. This important step described in [19] opened a new field for RPCs detectors and their applications. Since then, Time-of-Flight systems (ToF) have been developed to improve particle identification in different high-energy physics experiments.

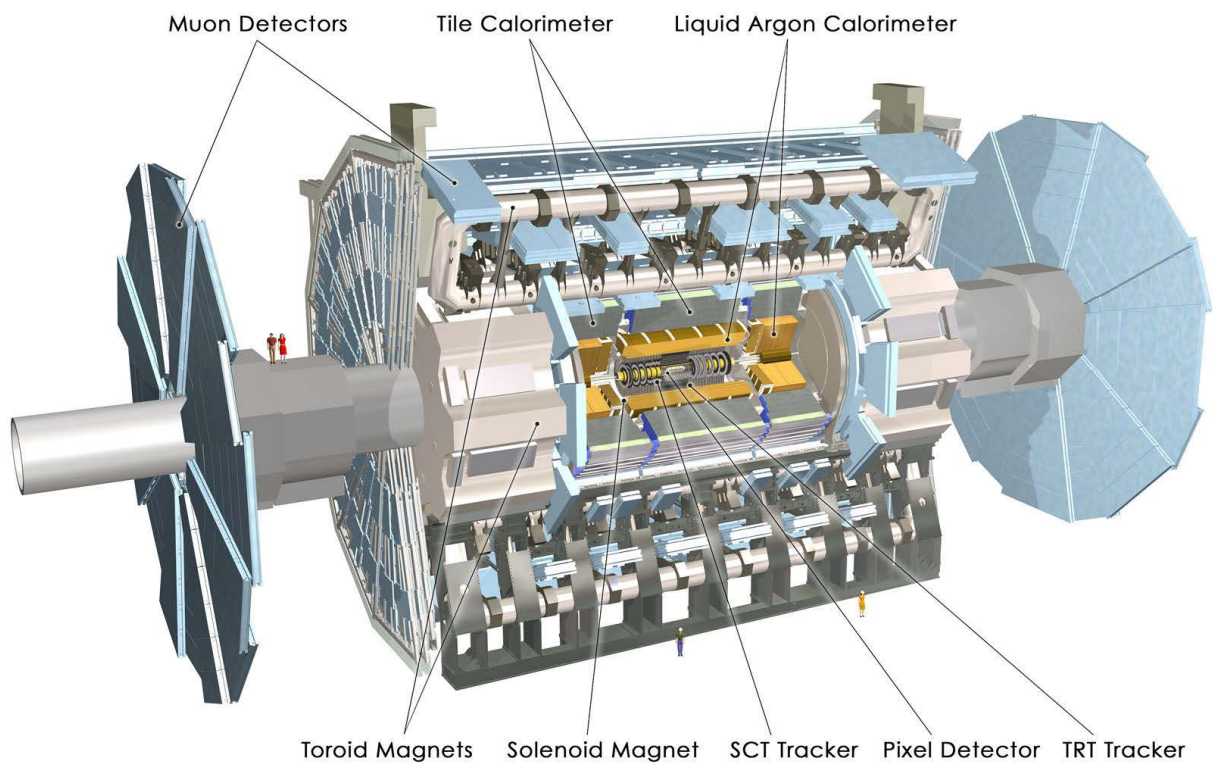


Figure 1.1.: A computer generated image of the ATLAS detector displaying its sub-detectors. The muon detectors are located at the outermost part of the barrel and at the end-caps. They are depicted in light blue. Each of the volumes is a module containing the RPCs inside. Taken from [15].

## ALICE ToF

The Time-of-Flight detector of the ALICE experiment is one example of timing RPCs used for particle identification. This is achieved by combining the time information with particle momentum and track length measured by the magnetic spectrometer. ALICE has a barrel-like configuration, with the ToF system having a full coverage in the azimuthal angle  $\phi$  and a polar acceptance  $|\theta - 90^\circ| < 45^\circ$ . It is comprised of 90 modules containing the RPCs [20]. The RPCs are arranged in two stacks of five gaps of  $250 \mu\text{m}/\text{gap}$  (see Figure 1.2). The electrodes consist of "soda-lime" glass ( $\rho \sim 10^{13} \Omega \text{cm}$ ) with thickness of  $400 \mu\text{m}$  for the internal plates and  $550 \mu\text{m}$  for the external ones. The results achieved with this configuration are 99.9 % efficiency and a time resolution better than 50 ps.

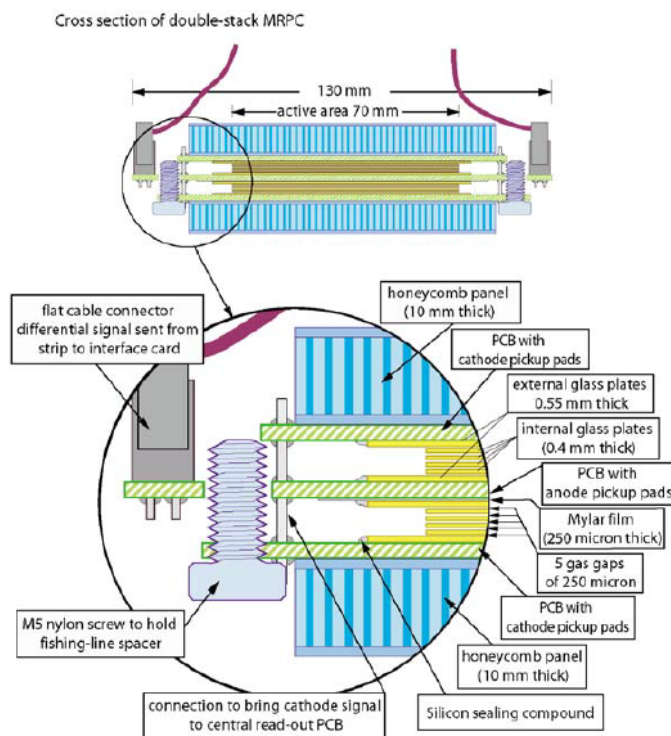


Figure 1.2.: A detailed schema of the interior of an ALICE timing RPC, from [21].

## HADES RPC-ToF

The High Acceptance Di-Electron Spectrometer (HADES) is located at the Helmholtzzentrum für Schwerionenforschung (GSI). It was designed to investigate matter at high density. This is achieved through the study of dilepton decay channels (therefore the name Di-Electron Spectrometer) of vector mesons.

During its working lifetime, this detector has undergone several upgrades. One of them consisted in the installation of a Time-of-Flight wall using RPCs. The main points of the research of these RPCs can be found in [22].

The RPC wall covers an area of  $8\text{ m}^2$  at polar angles in the range  $18\text{--}45^\circ$ . The fluxes expected at this region are up to  $10^3\text{ cm}^{-2}\text{ s}^{-1}$  for the lower polar angles [23]. The RPCs used have 4 gaps  $270\text{ }\mu\text{m}$  wide. A particular detail in the module construction is the shielding of each single RPC to minimize cross-talk. This feature reduces crosstalk to 2.3% at the fully shielded region as compared to 6.9% of the rest of the detector.

### FOPI RPC Barrel

The  $4\pi$  experiment (FOPI) was an apparatus installed at GSI. Its purpose was to study relativistic heavy-ion collisions at energies up to 2 AGeV. The FOPI collaboration studied in-medium effects and strangeness production in hot and dense nuclear matter. The detector was assembled in a barrel configuration. The RPC Time-of-Flight wall was located in a cylindrical shell 94 cm around the beam radius. It covered full azimuthal angle [24].

The RPCs used in this detector consisted of 8 gaps ( $2\times 4$ ) with a gap width of  $220\text{ }\mu\text{m}$ . The material used as electrodes was silica glass with a bulk resistivity of  $7\times 10^{12}\text{ }\Omega\text{ cm}$ . This material was chosen due to the low fluxes expected at the wall ( $< 100\text{ cm}^{-2}\text{ s}^{-1}$ ) [25].

## 1.3. The Compressed Baryonic Matter experiment

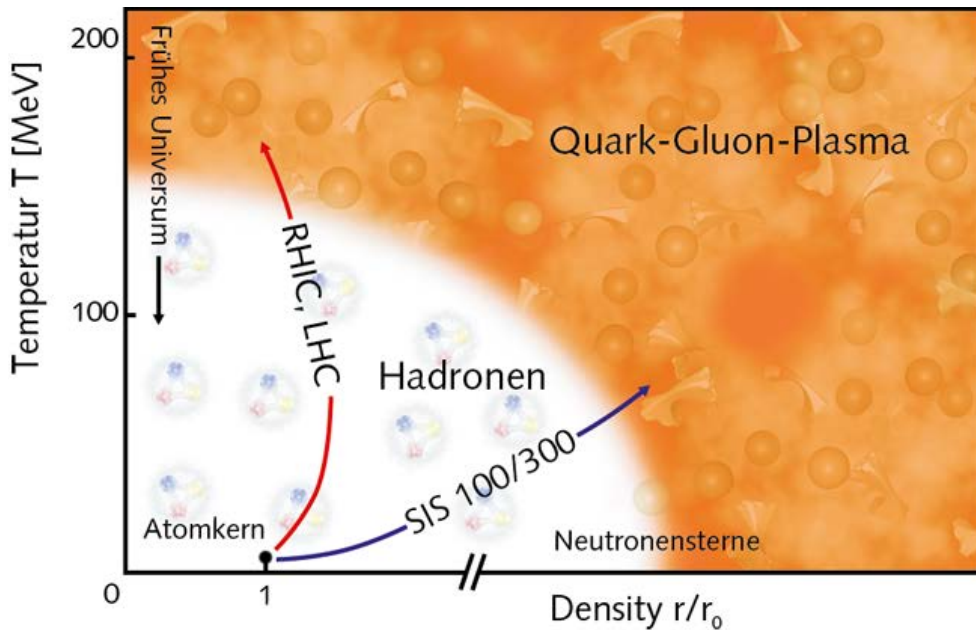


Figure 1.3.: Qualitative representation of the phase diagram of strongly interacting matter. The red line shows the scans done in recent years at RHIC and LHC. The blue line represents the intended scan at the future SIS-100/300 accelerators. Taken from [26].

In the previous section a brief overall description of RPCs has been given, as well as their application in current and past experiments. All the systems mentioned had electrodes made of glass or bakelite with bulk resistivities in the order of  $10^9 - 10^{13}\text{ }\Omega\text{ cm}$ . These RPCs

have proven suitable for their applications in low-rate environments, where the fluxes are  $\phi < 10^3 \text{ cm}^{-2} \text{ s}^{-1}$ .

However, with the future Facility for Antiproton and Ion Research (FAIR) in particular at the Compressed Baryonic Matter (CBM) experiment the term "high rate environment" acquires a new meaning.

FAIR will be located in Darmstadt, Germany, sharing premises with the current GSI. The facility will encompass a group of accelerators which will provide the tools for research in a wide range of fields. At the core of the facility two synchrotrons, SIS-100 and SIS-300, will accelerate protons and ions and deliver them to the corresponding experiments [27].

The CBM experiment is designed to study the properties of hadrons in nuclear matter at maximum net baryon density achievable in laboratory [28]. This will provide insights into the phase diagram of strongly interacting matter. A qualitative representation is introduced in Figure 1.3. This phase diagram is one of the fundamental issues to be answered in subatomic physics today. What happens inside neutron stars? Is there a phase transition at high densities of nuclear matter? How are the properties of hadrons modified at these high densities? What is deconfinement?

The study of the phase diagram has been a part of the physics program in several experiments as ALICE, CMS and ATLAS at CERN or STAR and PHENIX at RHIC. All these experiments have been oriented to very high temperatures  $T$  and low net baryon densities. Also, at RHIC a beam energy scan at moderate  $T$  and high-net baryon densities was done.

The CBM experiment is designed to acquire empirical data which will aid in the resolution of these questions. The CBM will be a fixed-target experiment with a modular spectrometer which will allow the structure to be modified depending on the physics case. Thus, it is possible to speak of two different configurations: an electron/hadron configuration (seen in Figure 1.4 upper panel) or the muon configuration (shown in Figure 1.4 lower panel). Furthermore, the very high interaction rates (up to 10 MHz), with charged particle multiplicities up to 1000 per event, will allow for a systematic study of the phase diagram through the analysis of rare probes with sufficient statistics.

However, at the same time, these high multiplicities and harsh radiation environment pose a challenge to current particle detection methods. Thus, an intense research and development process has taken place in the past eight years. Here, a short description of each of the sub-detectors is presented.

- The Silicon Tracking System (STS). It is considered the heart of the CBM detector. A detailed description can be found in the Technical Design Report [30]. The main requirements for this detector are: a high particle multiplicity detection, up to 1000 particles per event, an efficiency better than 95% and momentum reconstruction with a resolution of  $\Delta p/p = 1\%$ . In addition, simulations show a non-ionizing dose for the points closest to the beam-line of  $10^{14} n_{eq} \text{ cm}^{-2} \text{ per year}^1$ . The solution proposed in

---

<sup>1</sup>The non-ionizing energy loss, NIELS, is defined for charged particles as the energy lost by the particle traversing matter due to displacements, vacancies or interstitials in the material. In the case of neutrons, this energy loss is non-ionizing dose. The non-ionizing dose has units of  $\text{MeV cm}^{-2} \text{ s}^{-1}$ . However, it can also be referred to 1 MeV neutrons. Thus it can be expressed as equivalent to a certain flux of 1 MeV neutrons,  $n_{eq}$  per unit of area per unit of time. A working CBM year is estimated as

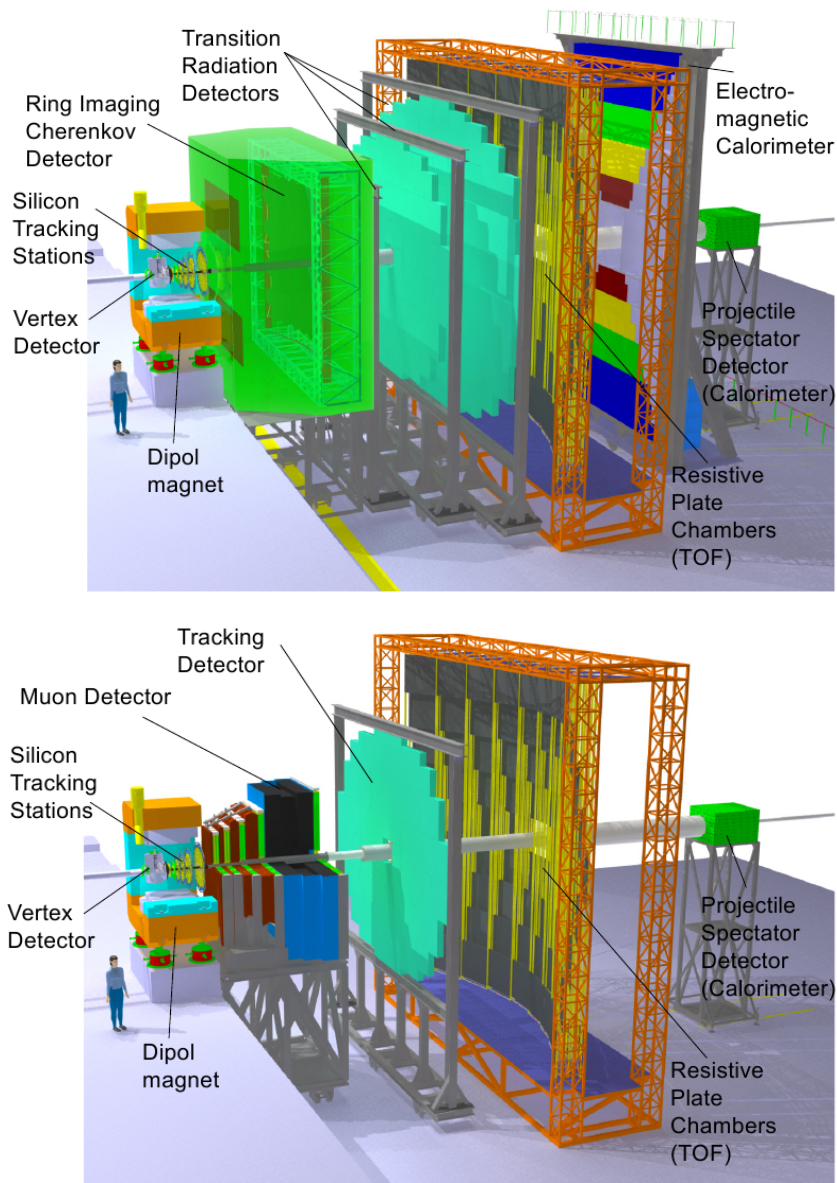


Figure 1.4.: Two configurations for CBM at SIS-100/SIS-300. Upper panel shows the configuration for electron detection. The detector chain is: Micro-Vertex Detector, Silicon Tracking System, Ring Imaging Cherenkov, Transition Radiation Detector, Time of Flight, Electromagnetic Calorimeter and Particle Spectator Detector. Lower panel shows the configuration for muon detection. Some of the sub-detectors have been substituted for an absorber. The detector chain is: Micro-Vertex Detector, Silicon Tracking System, Muon Chamber system, Time of Flight and Particle Spectator Detector. Taken from [29].

the Silicon Tracker Technical Design Report is that of 8 layers of silicon micro-strip detectors with low-mass budget. Prototypes with a spatial resolution in the order of

---

$5 \times 10^{-13}$  gold beam ions at the MVD station [31].

35  $\mu\text{m}$  have been successfully tested with proton beams.

- The Micro-Vertex Detector (MVD). Secondary vertex detection with high precision is needed for the study of  $D$  mesons. This requires a dedicated detector in addition to the STS. This detector will be composed by Monolithic Active Pixel Sensors (MAPS). These sensors have a very low material budget ranging from 300  $\mu\text{m}$  of silicon equivalent for the sensors and supports in the smallest detector stations to 500  $\mu\text{m}$  for the largest stations [28, 32]. The radiation environment for this detector is expected to be  $10^{13} n_{eq} \text{ cm}^{-2}$  per year.
- The Ring Imaging Cherenkov Detector (RICH). Its purpose will be the identification of electrons and suppression of pions in a momentum range  $< 8 \text{ GeV}/c$ . To achieve this, the RICH will be built with  $\text{CO}_2$  as radiator and multi-anode photomultipliers for readout. The goal is to have more than 20 photons per Cherenkov ring and a pion suppression in the order of 500-1000 for momenta below  $8 \text{ GeV}/c$ . These detectors will have a geometrical acceptance of  $\pm 25^\circ$  vertically and  $\pm 35^\circ$  horizontally [28, 33].
- The Transition Radiation Detector (TRD). It will be used for particle tracking and identification of electrons and positrons with momenta  $> 1.5 \text{ GeV}/c$  [28, 34]. Depending on the configuration it is expected to have 4 detection layers at SIS-100 with a pion suppression factor of 10 and 10 detection layers at SIS-300 with a pion suppression of 100. The highest particle fluxes for this detector are estimated to be on the order of  $10^5 \text{ cm}^{-2} \text{ s}^{-1}$ .
- The Muon Chamber System (MuCh). It is a hadron absorber/tracker combination. The hadron absorber will be segmented with a tracking system in-between each two consecutive absorber segments. The goal is to measure low-momentum muons to study charmonium decays. The challenge is to create an absorber compact enough to minimize the number of muons generated by vector meson decays in the detector while providing a good background suppression. GEM technology, with physical detection processes similar to the ones in RPCs, has been proposed as part of this detector [28, 35].
- The Time-of-Flight Wall (ToF). The identification of hadrons will be performed via time of flight. A detailed description of this system is provided in the next section.
- The Electromagnetic CALorimeter (ECAL). Its goal is the identification of photons and neutral mesons decaying into photons [28]. It is a well-established technology already used in experiments like HERA-B [36] and LHCb [37].
- The Projectile Spectator Detector (PSD). Its goal will be the determination of collision centrality and orientation of the reaction plane [28].

### 1.3.1. The Time of Flight Wall

#### Particle identification via Time of Flight

Particle identification is a crucial step in the analysis of high-energy physics experiment data. A way of classifying particles is through two basic properties: their charge and their rest mass. The charge of a particle can be determined through the sign of the curvature of the trajectory of the particle when crossing a region with a magnetic field. Magnetic spectrometers measure the rigidity  $R = p/z$ , where  $p$  is the momentum of the particle and  $z$  its charge. One of the methods used for particle mass determination is the time of flight technique, which is explained in the following [38].

The momentum,  $p$ , of a particle is related to its rest mass,  $m_0$ , by the expression

$$p = m_0 \beta \gamma c, \quad (1.1)$$

where  $\beta = v/c$  is the velocity of the particle in units of the speed of light  $c$  and  $\gamma$  is the Lorentz contraction factor  $\gamma = 1/\sqrt{1 - \beta^2}$ . A particle travelling a distance  $L$  will need a time  $t$ . Putting all this together, it is possible to reach an equation which relates the mass of the particle with the time it requires to travel a certain distance:

$$m_0 = \frac{p}{\beta \gamma c} = \frac{p}{c} \sqrt{\frac{c^2 t^2}{L^2} - 1}. \quad (1.2)$$

This equation describes a way of determining the mass of a single particle in terms of measured parameters. However, according to eq. (1.1), two particles with different masses can have the same momentum. The difference will be the time required by each particle to cross the same distance. This fact imposes a requirement in the precision of the time of flight measurement. If the precision of the system is worse than the time difference of the particles, it will not be possible to identify correctly each particle. This condition can be summarized in the following equation for equal path lengths of the two particles:

$$t_2 - t_1 = \frac{L}{c} \left| \sqrt{1 + \frac{m_2^2 c^2}{p^2}} - \sqrt{1 + \frac{m_1^2 c^2}{p^2}} \right| \approx \frac{Lc}{2p^2} (m_2^2 - m_1^2), \quad (1.3)$$

where the approximation  $E \approx pc$  for relativistic particles was done.

The physics performance of the CBM Time-of-Flight wall was studied through Monte Carlo simulations. The particle identification of protons, pions and kaons is shown in Figure 1.5. The simulation is of  $10^5$  Au+Au collisions at 10 AGeV. The three structures displayed correspond from left to right to pions ( $m^2 \approx 0.019 \text{ GeV}^2/c^4$ ), kaons ( $m^2 \approx 0.24 \text{ GeV}^2/c^4$ ) and protons ( $m^2 \approx 0.87 \text{ GeV}^2/c^4$ ), respectively.

### 1.3.2. Specifications of the CBM-ToF

The Time-of-Flight wall of the CBM experiment will provide charged hadron identification through time measurement and momentum (in conjunction with the STS) determination [40]. It has been divided in different regions according to the particle fluxes expected. The wall will be placed at a distance from the target that depends on the energy of the



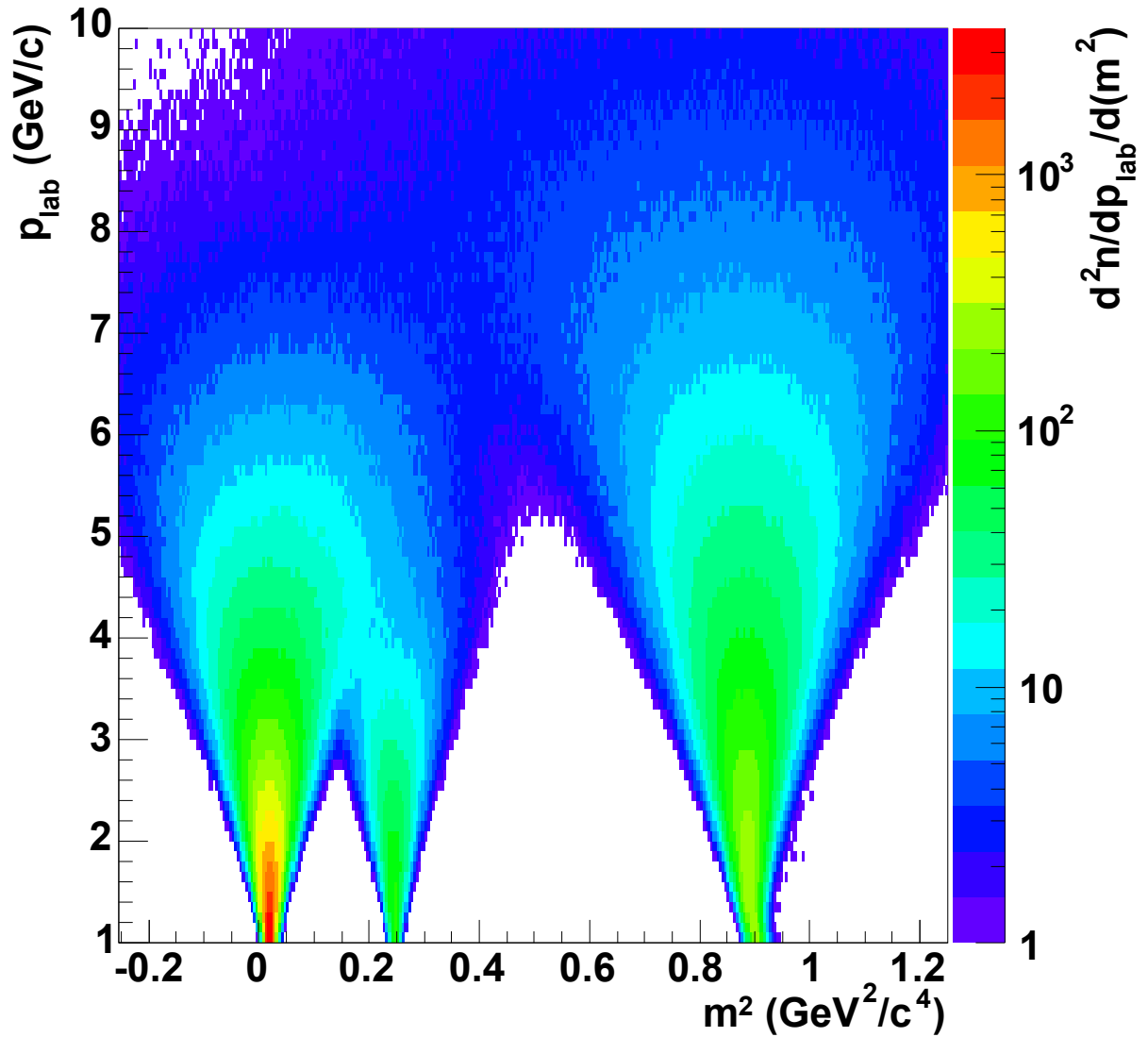


Figure 1.5.: Monte Carlo simulation results of the performance of the ToF wall. The square of the rest mass versus the momentum of the particles is plotted. The wall is located 10 meters away from the target. The time resolution is assumed to be 80 picoseconds. From [39].

primary beam. Since the primary goal is proton, kaon and pion separation, and due to the short lifetime of the kaons, for the lower energies, the wall will be placed at 6 m from the interaction point, with the possibility to shift it up to 10 m. Therefore, the fluxes on the regions not only depend on the interaction rate and particle multiplicities but also on the position of the wall itself. Thus, for Au+Au collisions at 25 AGeV, in the outermost regions fluxes of  $< 10^3 \text{ cm}^{-2} \text{ s}^{-1}$  are expected while in the innermost part, close to the beam pipe, the simulations predict a value of  $< 3 \times 10^5 \text{ cm}^{-2} \text{ s}^{-1}$ . These results are shown in the upper panel of Figure 1.6. These fluxes are orders of magnitude higher than the typical bakelite or float glass RPC can withstand. Not only these high fluxes pose a challenge in RPC development but also the global requirements of the ToF detector. The main requirements are efficiency of  $> 95\%$ , time resolution of  $\sim 80 \text{ ps}$  and low occupancy,  $< 5\%$ . To fulfil these requirements new materials have been investigated as well as very highly granular read-out architectures designed.

Table 1.1 summarizes the different fluxes for each of this sections. A different solution is proposed for each region.

| Zone | Expected flux [ $10^3 \text{ cm}^{-2} \text{ s}^{-1}$ ] | Material proposed     |
|------|---|-----------------------|
| A    | $< 1.9$   | silica glass          |
| B    | $< 3.2$   | low resistivity glass |
| C    | $< 6.0$   | low resistivity glass |
| D    | $< 27$  | low resistivity glass |
| E    | $< 82$  | ceramics              |

Table 1.1.: Classification of zones of the ToF wall according to the fluxes and the corresponding electrode material proposed.

## 1.4. Outline of this thesis

The CBM experiment will be a next generation experiment. The special requirements for its Time-of-Flight wall, specifically the radiation tolerance and rate capabilities, has motivated the research on new materials. The Hadron Physics group at HZDR actively participates in this project through research and development of RPCs with ceramic electrodes. This thesis will present the results of these new detectors and how they fulfil the requirements for the CBM-ToF. Special attention will be given to the high-rate tests with electron and proton beams with the results of an increase of RPC rate capabilities by at least two orders of magnitude. These detectors, as of this day, exhibit the highest rate capabilities in the field.

The outline of this thesis is as follows:

- Chapter 2 will be devoted to the physics of RPCs. A brief description of avalanche formation and signal induction will be given. The theoretical considerations pertaining the main parameters of RPCs (efficiency, time resolution, rate capabilities) are also described.

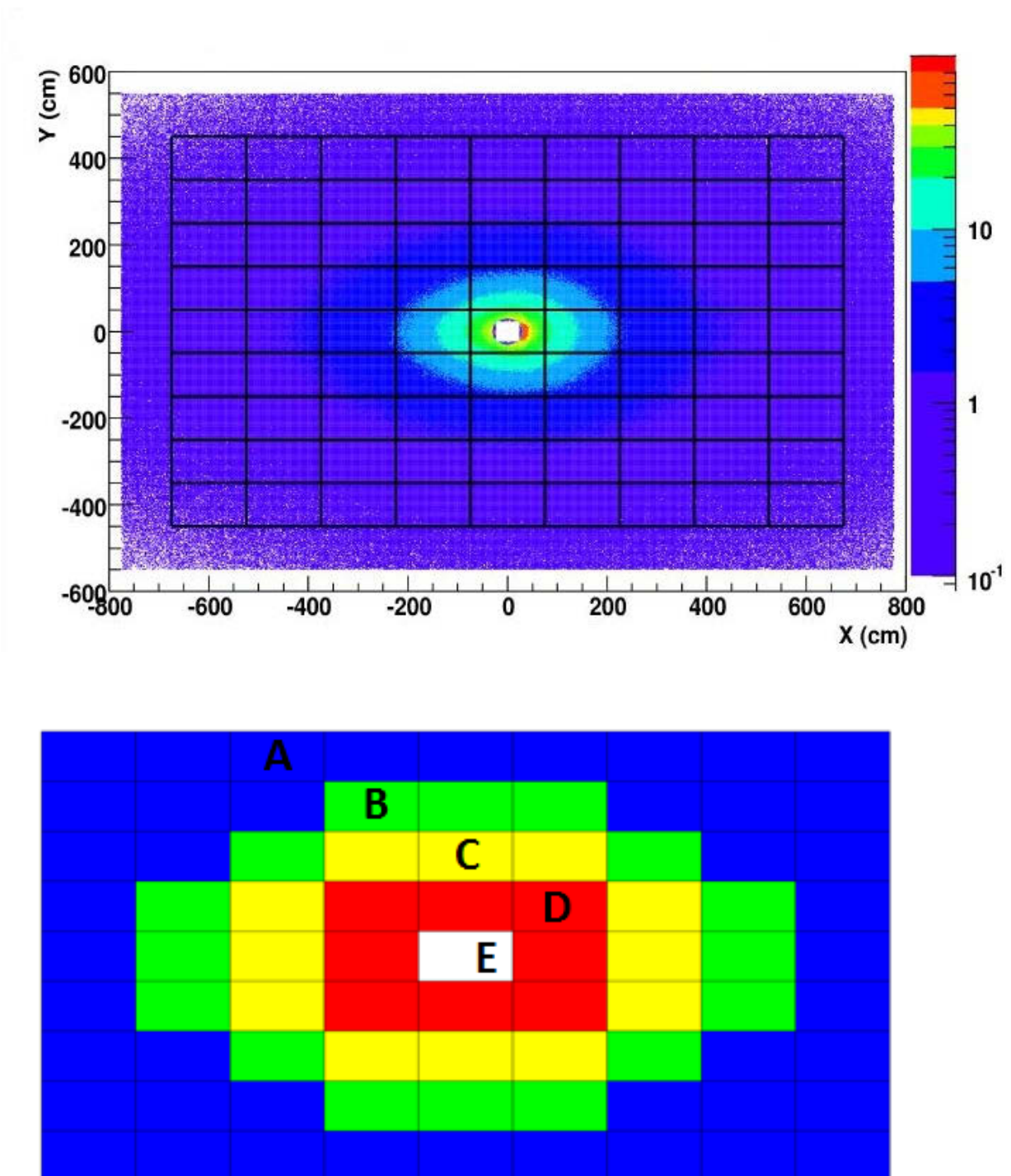


Figure 1.6.: Upper panel: Simulation of the fluxes (in units of  $10^3 \text{ cm}^{-2} \text{ s}^{-1}$ ) to which the ToF wall will be subjected. The square panel in the centre is a hole in the ToF wall corresponding to the beam-pipe. Lower panel: Separation of the ToF wall in five regions depending on the flux predictions based on simulations. Taken from [41].

- Chapter 3 will introduce the new  $\text{Si}_3\text{N}_4/\text{SiC}$  ceramic composites. It will address the results of the measurements of the electrical properties like bulk resistivity and electrical permittivity of these ceramics. A description of  $\text{Al}_2\text{O}_3$  ceramics is also given.
- Chapter 4 will describe the prototypes assembled and tested at HZDR. The prototypes will be compared with each other. The benefits and drawbacks of each architecture will be analysed.
- Chapter 5 describes the experimental set-up used in the tests of the RPCs. A way to calculate the incoming particle fluxes for non-uniform irradiation is proposed.
- Chapter 6 shows the results of the measurements. The deduced parameters of RPCs are then compared to theoretical models to understand the behaviour of semiconductive ceramics as RPC electrodes.
- Chapter 7 will summarize the results of this thesis and discuss how the improvement of rate capabilities open the doors to the usage RPCs in high irradiation environments in future accelerator experiments.

## 2. Resistive Plate Chambers

### 2.1. Parallel Plate Geometries

A RPC is a detector with a parallel plate geometry. A sketch of a single-gap RPC is shown in Figure 2.1. The resistive plates depicted in blue are placed parallel to each other. The gap in-between is built by means of a high-resistive separator like fishing line, mylar or ceramics. The dimensions of this separator define the gas gap size. The gas flows through the gaps in-between the resistive plates. For example, RPCs used for timing measurements have sub-millimetre gas gaps which increases the time resolution by one order of magnitude, from nanoseconds to a few hundred picoseconds or better. Triggering RPCs, where time resolution is not so critical, use millimetre-sized gas gaps. The high voltage is applied to the outer part of the RPC, by connecting the supply to metallic electrodes. These electrodes cover the whole RPC area, either by a single uniform electrode [42] or by a segmented scheme following the geometry of the readout strips [43]. The typical material for these electrodes is copper, although graphite layers are also used. Thus an homogeneous high electric field is established in the gaps. In contrast to other gas detectors, like the drift chambers, RPCs use very high voltages in the order of several kilovolts to generate charge multiplication. The reason is that the electric field in a parallel plate geometry is constant, while in the drift chamber, the wires generate a logarithmic field strength distribution for which only few hundreds of Volts are needed. Thus the field in the anode wire in a drift chamber is strong enough to induce charge multiplication.

### 2.2. Gas ionization by charged particles

A fast charged particle traversing a gas can collide with the atoms or molecules of the gas. In the collision the particle will transfer part of its energy to the atom. The atom can change to an excited state or can become ionized. The energy required for the creation of an ion-electron pair,  $W$ , is related to the energy deposited by the traversing particle,  $\langle dE/dx \rangle$ , as [44]

$$W \langle N \rangle = L \left\langle \frac{dE}{dx} \right\rangle, \quad (2.1)$$

where  $\langle N \rangle$  is the average number of ion-electron pairs created along the path of length  $L$ . This energy varies with gas composition and density, as well as the nature of the incoming particle.

It is important to establish a difference between the primary ionization created by the primary incoming particle and secondary ionization created by the electrons liberated during the primary ionization process. In the primary ionization process, a small number

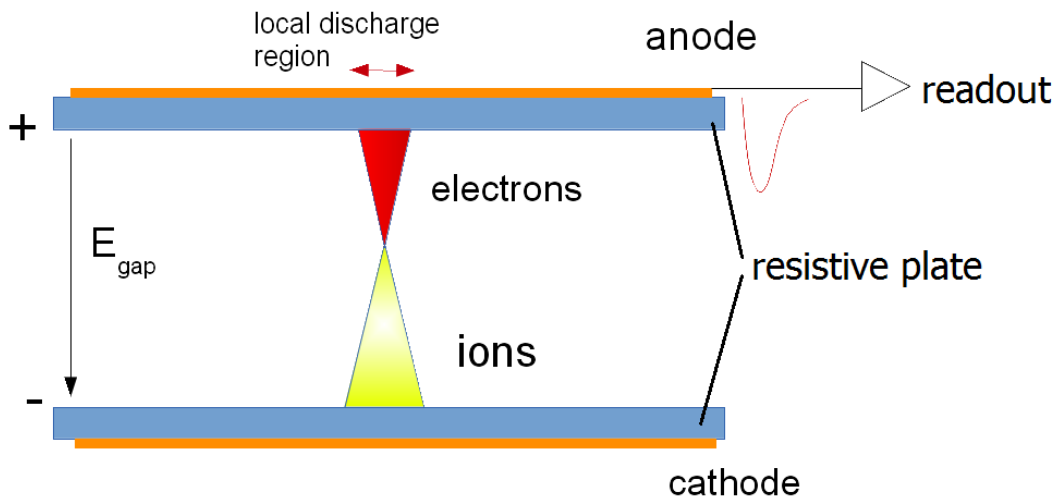


Figure 2.1.: Depiction of a single gap RPC and the avalanche development inside. For a complete description see the text.

of electrons is separated from the atom. This secondary electrons can ionize other atoms from the gas. They can also get attached to the atoms of the gas.

When the energy lost by the incoming particle is not enough to ionize the atoms, they will get into an excited state. During the de-excitation process, and depending on the electronic transition, a high-energetic photon can be created. If the energy of this photon is high enough, it can ionize an atom from the gas.

The search for a good gas composition for RPCs is still ongoing. There is no "standard" mixture. Instead, each experiment or development group might choose the one most suited for their purposes. However, the gas mixtures used have all some common characteristics. In particular, the mixture should provide a good amplification of the signal, while preventing the formation of streamers, and limiting the lateral distribution of the avalanche. Many studies have been done to investigate the efficiency and time resolution dependence on the gas mixture (cf. [45–47]).

## 2.3. Avalanche formation and signal induction processes

As gas detectors, RPCs rely heavily on the ionization parameters of the gas. Therefore, a detailed understanding of the physics of avalanche formation and signal induction is necessary to explain the detector properties, the most important ones being the efficiency and the time resolution. Such a monumental task was undertaken successfully by Lippmann and Riegler who, through detailed implementation of physical processes in gases in simulations, managed to explain the physical phenomena during avalanche formation and relate it to the performance of the detector [48–51].

### 2.3.1. Cluster formation

When an energetic charged particle reaches the gas gap, it will ionize the atoms of the gas with a certain probability given by the ionization cross section  $\sigma_{ion}$ . In each ionization there is a certain probability that one or more electrons will be released. The group of liberated electrons during one ionization receive the name of ionization clusters. Each cluster can contain one or more electrons depending on the gas composition.

On average, the distance that a particle travels in a medium before ionizing an atom is given by the mean free path  $\lambda$ . The mean free path is related to the ionization cross section as

$$\lambda = \frac{A}{\rho N_A \sigma_{ion}(\beta)}, \quad (2.2)$$

with  $A$  the atomic mass number of the medium,  $\rho$  its density,  $N_A$  Avogadro's constant and  $\sigma_{ion}(\beta)$  the ionization cross section depending on the particle velocity  $\beta$ . Once the mean free path is known, it is possible to calculate the distance between each of these ionization clusters. If one assumes that a collision happening in time is independent of the previous one, the probability of a collision after a path length  $z$  takes the form of an exponential distribution

$$P(z) = \frac{1}{\lambda} e^{-\frac{z}{\lambda}}. \quad (2.3)$$

Following this result, it is useful to calculate the cluster size distribution. Knowing the probability of a collision after a distance  $z$  we now focus on the number of clusters  $n$  that are created after a distance  $g$  (typically the gas gap). This probability is given by a Poisson distribution:

$$P(n) = \frac{1}{n!} \left(\frac{g}{\lambda}\right)^n e^{-\frac{g}{\lambda}}, \quad (2.4)$$

where the average number of clusters is  $\bar{n} = g/\lambda$ . This number varies with the gas composition and the velocity of the particle. This quantity was calculated for two gas mixtures. The program used is HEED++ developed by Smirnov at CERN [52]. HEED is a Monte Carlo simulation program which models the ionization and photoabsorption processes. The simulation was done in a 1 mm wide gap with an electric field strength of 100 kV/cm. The incoming particles were electrons. This version of program is linked to the Garfield++

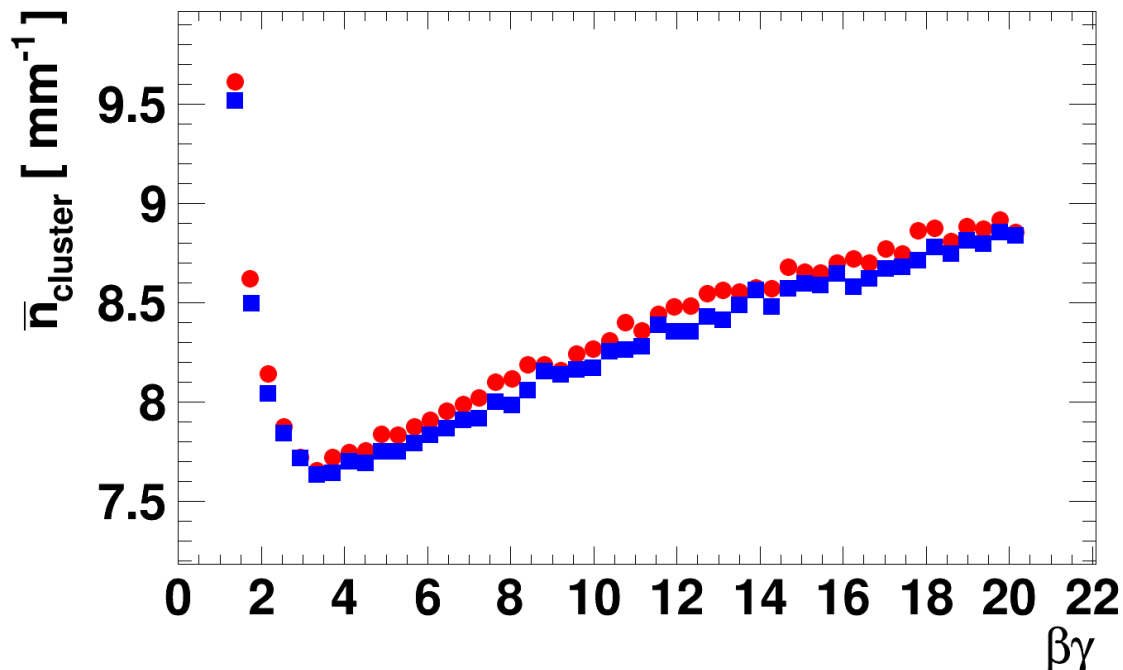


Figure 2.2.: Simulated primary cluster number as a function of the product  $\beta\gamma$  with the program HEED++. The red bullets,  $\bullet$ , represent the results for a mixture 85% $\text{C}_2\text{H}_2\text{F}_4$ /10% $\text{SF}_6$ /5% $i\text{-C}_4\text{H}_{10}$  and the blue squares  $\blacksquare$  correspond to a mixture 90% $\text{C}_2\text{H}_2\text{F}_4$ /10% $\text{SF}_6$ .

software. Garfield was also developed at CERN to simulate the behaviour of gaseous detectors [53].

The results of the simulation are collected in Figure 2.2. The number of clusters per length unit  $\bar{n}$  is drawn as a function of the combination  $\beta\lambda$ , with  $\beta$  the velocity of the incoming particles and  $\gamma$  the Lorentz factor associated. The minimum number of clusters generated is reached for  $\beta\gamma \approx 3$  corresponding to minimum ionizing particles (MIPs). There is a marginal difference between the two gas mixtures used.

### 2.3.2. Avalanche multiplication

Once the primary clusters are formed, the electrons in them will start drifting due to the electric field towards the anode, while the ions drift towards the cathode with a much slower velocity, producing secondary ionizations on their paths and forming an avalanche. In a RPC, the average motion direction will be along electric field vector.

In a microscopic theory of collisions, each of the electrons will be accelerated by the electric field gaining a kinetic energy until it is enough to ionize another atom. In-between collisions, the electrons will acquire an average kinetic energy

$$T = e|\vec{E}|\Delta z. \quad (2.5)$$



Then, it will lose this energy in a collision by excitation or recoil, and afterwards the process will start again. Consider the ionization potential for pure Argon,  $W = 15.76$  eV [44] and an electric field strength in the RPC gas gap of  $E_{gap} = 100$  kV/cm. After being ionized, an electron will start accelerating. The minimum distance it must travel to be able to ionize another molecule will be  $\lambda > 2 \mu\text{m}$ .

However, there is also a chance that the electron is attached to an ion, thus breaking its drift towards the anode. On average, the variation of the number of electrons (ions) in an avalanche can be expressed as

$$\frac{d\bar{n}}{dz} = (\alpha - \eta)\bar{n}, \quad (2.6)$$

where  $\bar{n}$  is the average number of electrons in the avalanche,  $\alpha$  is the first Townsend coefficient<sup>1</sup> providing the probability of ionization per unit of length and  $\eta$  is the attachment coefficient accounting for the probability of electron attachment per unit of length. In Figure 2.3, four gas parameters are plotted as a function of the electric field strength for two gas mixtures. No significant difference between both mixtures are observed.

After a distance  $z$  the number of electrons in the avalanche is

$$\bar{n} = n_0 e^{(\alpha - \eta)z}. \quad (2.7)$$

This is yet an incomplete picture of the physics of the gases in RPCs. Considering an example of a timing RPC with a gas gap of  $300 \mu\text{m}$  with a mixture of 85%  $\text{C}_2\text{H}_2\text{F}_4$ /10% i-butane/5%  $\text{SF}_6$  operating at 100 kV/cm, one can calculate the number of electrons in an avalanche and obtains  $\bar{n} \sim 10^{13}$  which corresponds to an induced charge of  $\sim 10^7$  pC, to be compared with a value of a few pC collected in normal timing RPCs.

The explanation given by Lippmann [48] is that there is an effective cut-off on the growth of the avalanche. This cut-off is due to the space-charge effect. This term was first coined by Raether [55]. The avalanche can grow so large that the charges inside start affecting the electric field in the gap and effectively reduce the values of the ionization and attachment coefficients.

The cut-off establishes the maximum gain attainable before the growth of the avalanche is stopped. This limit is given by the product of the effective Townsend coefficient  $\alpha_{eff}$  and the gas gap  $g$

$$\alpha_{eff}g \approx 18, \quad (2.8)$$

$$n_e = e^{\alpha_{eff}g} \approx 10^7. \quad (2.9)$$

Therefore, the maximum number of electrons  $n_e$  in the avalanche before the growth is affected by the space-charge is in the order of  $10^7$ . Recent measurements, however, show that the performance of RPCs might not require the space-charge effect for an explanation. The space-charge effect was introduced to effectively cut the grow of the avalanche due to the large number of electrons generated. In [56], measurements done at high electric fields and normal pressure show the Townsend coefficient to be much smaller than predicted by

---

<sup>1</sup>The second Townsend coefficient is defined as the probability that a photo-electron per electron in the avalanche is produced [54].

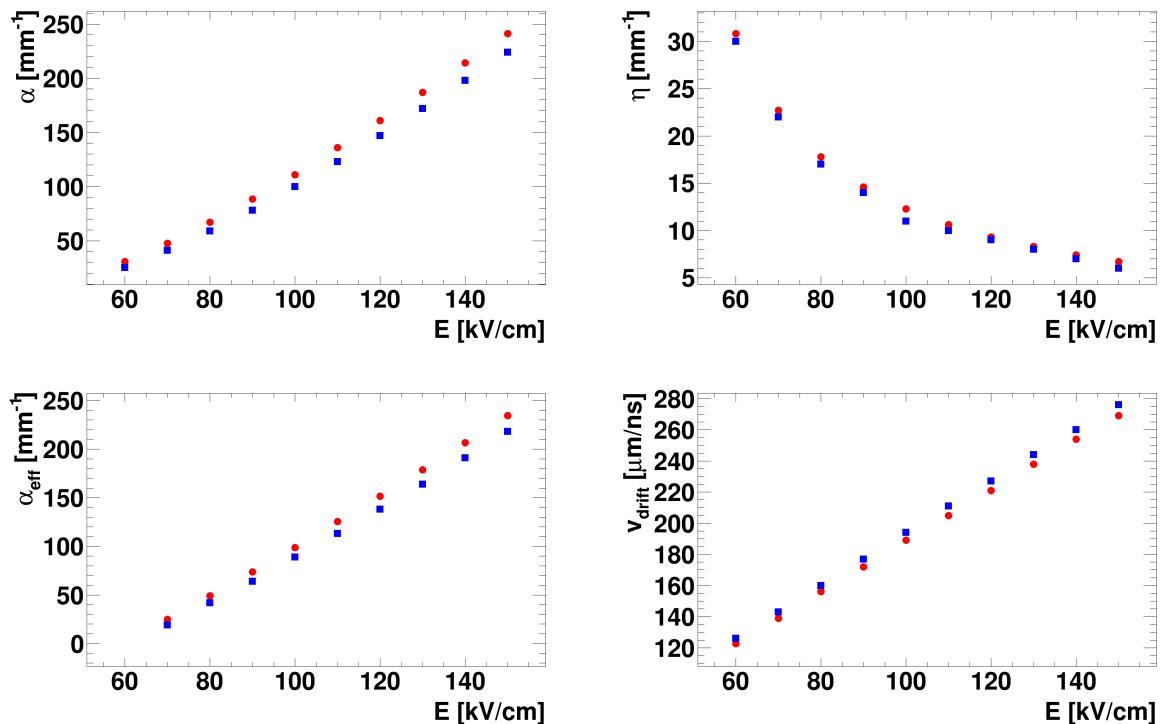


Figure 2.3.: Compilation of results of gas parameter simulations as a function of the electric field strength. The red bullets  $\bullet$  correspond to a gas mixture 85% $\text{C}_2\text{H}_2\text{F}_4$ /10% $\text{SF}_6$ /5%i- $\text{C}_4\text{H}_{10}$  and the blue squares  $\blacksquare$  to 90% $\text{C}_2\text{H}_2\text{F}_4$ /10% $\text{SF}_6$ . Upper left panel: The first Townsend coefficient. Upper right: the attachment coefficient. Lower left: the effective Townsend coefficient. Lower right: the electron drift velocity in the gas.

simulations. Thus the avalanche would not grow so large as to modify the electric field in the gap. To quote a number, in [56],  $\alpha = 20.7 \text{ mm}^{-1}$  is determined. Considering a gas gap of  $300 \mu\text{m}$ , one obtains  $\alpha g = 6.21$  which is much smaller than the established Raether limit [55]. However, the large difference between simulated and measured value remains unexplained. At the same time, in [56], the drift velocity of the electrons was determined obtaining a very good agreement with simulations.

### 2.3.3. Signal induction

The signal read-out from the detector is generated by the motion of the charged particles in the avalanche. The main component of the induction will be the drift of the electrons; the ions contribute in a very small way due to their small drift velocity. To obtain the current induced by the moving charges one uses Ramo's theorem [57] in the form

$$i_{\text{tot}}(t) = q_e N(t) v_{\text{drift}} E_w(x(t)), \quad (2.10)$$

where  $q_e$  is the elementary electric charge,  $N(t)$  is the number of electrons in the avalanche at a given time,  $v_{\text{drift}}(t)$  is the drift velocity and  $E_w$  is the weighting field at the point  $x(t)$ .

This is the current induced for each of the clusters generated during the passage of the primary ionizing particle. The total current induced in the readout electrodes is the sum of all the currents generated by the avalanches started by the individual clusters. That is,

$$i(t) = \sum_{j=1}^{n_{cluster}} i_j(t). \quad (2.11)$$

where  $i_j(t)$  is calculated as in eq. (2.10) and  $n_{cluster}$  is the number of primary clusters generated by the ionizing particle. From Figure 2.2 one deduces an average number of clusters of  $\bar{n}_{cluster} \approx 2$  for a  $300 \mu\text{m}$  and a minimum ionizing particle. Thus the total current is the sum of the current induced by each of the two clusters.

The weighting field  $E_w$  is not in itself a measurable quantity. It is an actual construct to calculate induced signals in electrodes. It is calculated by setting the electrode of interest at a potential of one volt and all the others to ground. An example of calculating the weighting field for an infinite parallel plane RPC is given in the following. Consider an RPC with  $k$  gaps and  $k + 1$  resistive plates between anode and cathode. This system can be considered as a capacitor consisting of  $2k + 1$  layers. Let us set the potential between anode and cathode to  $V_w$ . The electric field inside the RPC will be such that

$$\sum_{i=1}^{2k+1} E_i d_i = V_w, \quad (2.12)$$

i. e., the sum of the potential drops  $E_i d_i$  in each of the layers is the external potential. At the interfaces between layers, the continuity of the electric field applies:

$$E_i \epsilon_i = E_j \epsilon_j, \quad (2.13)$$

where  $i$  and  $j$  denote the adjacent media. Assume that resistive plates all have the same thickness  $b$  and relative permittivity  $\epsilon_r$ . Assume also that the gas gaps are all homogeneous with width  $g$  and that the gas has relative permittivity  $\epsilon_r \approx 1$ . The electric field strength in every gas gap will be  $E_g$  and the one in every plate  $E_b$ . Equations (2.12) and (2.13) become

$$V_w = (k + 1)bE_b + kgE_g, \quad (2.14)$$

$$E_g = E_b \epsilon_r. \quad (2.15)$$

The combination of both equations gives the final expression for the weighting field of a single strip of infinite extension in the static case:

$$\frac{E_g}{V_w} = \frac{\epsilon_r}{(k + 1)b + kg\epsilon_r}. \quad (2.16)$$

A numerical example of the weighting field is provided here for the case of  $\text{Si}_3\text{N}_4/\text{SiC}$  ceramics. The parameters in this case are:  $\rho \approx 10^9 \Omega \text{cm}$ ,  $\epsilon_r \approx 12$ ,  $b = 2 \text{mm}$ ,  $n = 2$ , and  $g = 250 \mu\text{m}$ . The weighting field in this case is  $E_w = 1 \text{mm}^{-1}$ . This value can be compared to  $E_w = 0.43 \text{mm}^{-1}$  in the case of a 8-gap glass RPC developed for the CBM-ToF Wall [58].

The final quantity measured is the induced charge. As described above, the motion of electrons and ions induce a current in the readout electrodes. The integral of this current gives the charge induced in the pick up strips:

$$q_{induced} = \int_0^T dt \sum_{p=1}^{n_{cluster}} E_w(x_p(t)) v_p(t) q_e N_p(t), \quad (2.17)$$

where the sum is over the clusters in the avalanche.

### 2.3.4. Total charge and induced charge

At this point it is important to establish the difference between the induced charge,  $q_{induced}$ , and the prompt charge,  $q_{prompt}$ . The induced charge is collected during the drift of both electrons and ions. The first electron/ion pairs are generated at distance  $\sim 1/\alpha$  from the anode. Therefore, there is a fast signal component generated by the electron drift. However, most of the signal corresponds to ion induction due to the long drift of these species towards the cathode. The ratio  $q_{prompt}/q_{induced}$  follows approximately the relation

$$\frac{q_{prompt}}{q_{induced}} \sim \frac{1}{\alpha g}, \quad (2.18)$$

therefore, the charge induced during the drift of the ions constitutes most of the charge collected in the RPC. This fact is important when designing amplification electronics for RPCs. The ion induction process occurs at such a large time scale compared to the electron induction that it is filtered out. Therefore the signal read finally in the latest stages of the data acquisition is  $q_{prompt}$ . This charge is in the order of femtocoulombs. The total induced charge can be estimated considering the current flowing through the detector and the incoming particle flux (see Chapter 6). This charge is in the order of picocoulombs.

### 2.3.5. Signal read out

The signal is then transported through the strip outside the detector and into the front end electronics. Depending on the type of RPC, electronics might not be needed, such as in the case of trigger RPCs. However, for timing RPCs, due to the small size of the signal and the small charge collected, amplifying techniques are required to operate the detectors. As an example, for ceramic RPCs the Front End Electronics (FEE) developed for the FOPI collaboration were used. They will be discussed more in detail in Section 4.4.1. An example the signal after amplification for a ceramic RPC exposed to 30 MeV electrons is shown in Figure 2.4.

One important effect which needs to be addressed is the so called time-charge correlation or time-walk. The signals read out into the electronics need to be discriminated to separate the signal of the avalanche from the noise inherent to the detector. This discrimination is typically done by a certain voltage threshold, thus only the signals with a voltage level higher than the threshold will be digitized. The signal rise time is dependent on the charge contents of the signal. Thus signals with a higher charge (and therefore higher maximum voltage) will cross the threshold earlier than signals with lower charge content.

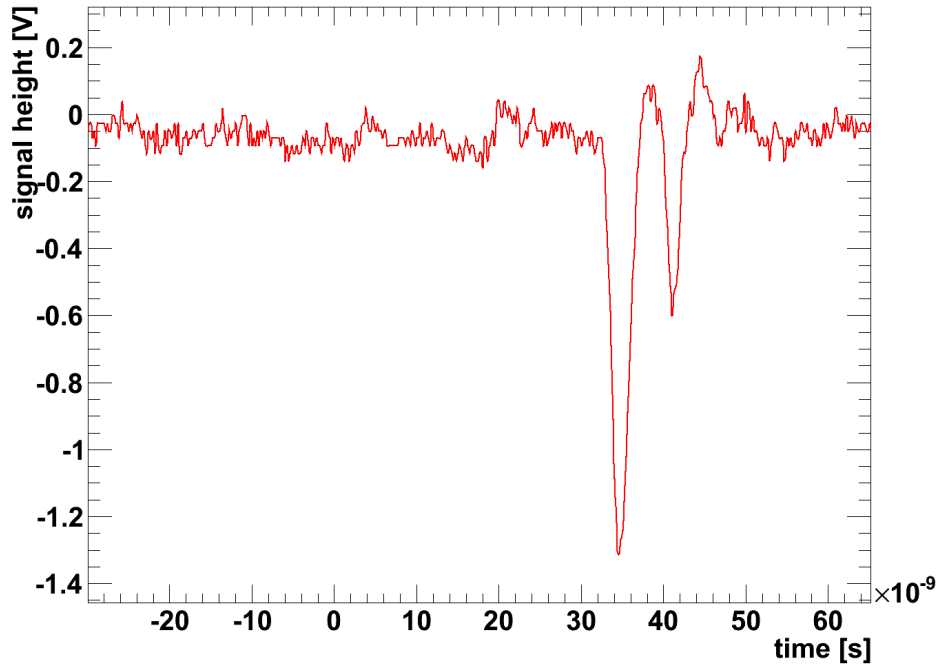


Figure 2.4.: A signal as seen in an oscilloscope after being amplified. The second valley corresponds to a secondary discharge, most probably generated at the edge of the readout electrode strip.

This translates into a dependence of the signal timing information with the charge. This effect must be corrected and can lead to an improvement of the timing properties of the RPC up to 20 ps approximately. In Chapter 6, the correction procedure is described.

### 2.3.6. Relaxation time

The main difference between a resistive plate chamber and a parallel plate chamber is the use of highly resistive materials. This prevents the formation of sparks and confines the avalanche to a very small region in the detector. However, this region will be unusable for a small period of time due to the drop in the electric field in a cylindrical volume described by the lateral extension of the avalanche when reaching the anode.

We have explained how an avalanche is created, develops and induces a signal on the pick up electrodes. When it reaches the surface of the anode electrode, the charges will take some time to “dissipate”. This time period is called the relaxation time. The final expression of this parameter is

$$\tau = 2R_b(2C_b + C_g) = 2\rho_b\epsilon_0 \left( 2\epsilon_r + \frac{b}{g} \right), \quad (2.19)$$

with  $R_b$  the resistance of the electrode material,  $C_b$  the capacitance of the electrode material,  $C_g$  the capacitance of the gas gap,  $\rho_b$  the bulk resistivity of the electrode material,  $\epsilon_r$

the relative permittivity,  $b$  the thickness of the resistive plate and  $g$  the width of the gas gap. With the values discussed below in Chapter 3,  $\epsilon_r \approx 12$ ,  $b = 2 \text{ cm}$ ,  $g = 250 \mu\text{m}$  and  $\rho \approx 10^9 \Omega \text{ cm}$ , the single electrode-gap-electrode structure has a time constant  $\tau \sim 20 \text{ ms}$ .

## 2.4. Efficiency

The efficiency of a single-gap RPC is intrinsically dependent on the number of clusters detected by an RPC. From eq. (2.4) it is possible to calculate the maximum efficiency of the system as

$$\epsilon_{max} = 1 - e^{-\bar{n}}, \quad (2.20)$$

where  $\bar{n}$  is the maximum number of clusters formed in the gas gap. From this equation and considering the gas mixtures used in RPCs one can calculate the maximum efficiency for a single gap RPC for several gap sizes. The current RPCs structures however, consists of stacks of several gas gaps. Considering each gas gap independent from the others, the maximum efficiency can then be calculated as

$$\epsilon_n = 1 - (1 - \epsilon_1)^n, \quad (2.21)$$

where  $n$  is the number of gaps,  $\epsilon_1$  is the efficiency of one gap and  $\epsilon_n$  is the efficiency of  $n$  gaps.

In practice, the efficiency determined in an experiment is smaller than these theoretical values. The discriminator threshold, used to separate signals from noise, effectively reduces the number of clusters detected by the RPCs. This is equivalent to place a threshold on the gas gap, indicating a minimum distance that the avalanche needs to travel to achieve the necessary charge to surpass the threshold.

Considering this threshold, the efficiency can be analytically described as

$$\epsilon = 1 - e^{-(1-\frac{\eta}{\alpha})n_0} \left( 1 + \frac{\alpha - \eta}{E_w} m_t \right)^{\frac{n_0}{\alpha g}}, \quad (2.22)$$

where  $n_0$  is the number of clusters formed in the gas gap,  $E_w$  the weighting field and  $m_t$  the charge threshold. The value for  $m_t = 10^5$  is typical of timing RPCs where the induced charge reaches tens of fC. The values of the parameters for this equation are all available. The value of  $n_0 = 4$  is taken from Figure 2.2 considering MIPs as primary particles and two gas gaps of  $250 \mu\text{m}$ . If the electric field strength in the gas gaps is  $E_g = 100 \text{ kV/cm}$  the values of  $\alpha = 105$  and  $\eta = 12$  are taken from Figure 2.3. The weighting field has been calculated above obtaining a value of  $E_w = 1 \text{ mm}^{-1}$  for  $\text{Si}_3\text{N}_4/\text{SiC}$  ceramic electrodes. The efficiency for a  $2 \times 2$  gap is then  $\epsilon \approx 89\%$ . This result is compatible to the efficiency estimate during in-beam tests of CRPCs (see Chapter 6).

## 2.5. Time resolution and the streamer limit

The time resolution is a parameter which shows the advantages of RPC technology. As discussed in Chapter 1, the development of timing-RPC has pushed the time resolution of

this detectors up to the frontier of 50 ps. This experimental result obtained for glass RPCs is already on the edge of what is theoretically possible for an RPC with a 200-300  $\mu\text{m}$  gas gaps [43].

The value of the time resolution is intrinsically dependent on the avalanche growth properties of the gas, which are at a given time and for a chosen gas mixture, defined by the electric field in the gas gap. Thus it is of interest to operate the RPC at the highest electric field possible.

There is a drawback however. The saturated avalanche regime in an RPC is limited to a region of a few hundred volts of applied voltage. Going beyond this region, the avalanche grows so large that it is not quenched or constraint to a small region in the RPC. This effect is called a streamer and has a completely different physical explanation as the avalanche. A streamer is characterised by an extremely large charge being orders of magnitude higher than the charge contained in an avalanche. The gas mixtures used in RPCs are specially selected because of the good timing achieved through a higher streamer-free region at high electric fields.

In developing RPCs for high rate environments, it has been observed that the bulk resistivity of the electrodes might not be enough to quench the streamers. This has been observed for bulk resistivity in the order of  $10^8 \Omega\text{cm}$  and will be further discussed in Chapter 4.

## 2.6. Rate capabilities

With the cell time constant  $\tau$  calculated as in eq. (2.19) one can estimate the rate capabilities in a very naïve way. The single cell time constant can be associate with the maximum frequency that discharges can have before the RPC properties deteriorate. One can obtain an estimation of the rate capabilities of the cell obtaining  $rate_{discharges} \sim 50 s^{-1}$ . However the measurements indicate that the RPC can work at much higher rates. This difference is due to the localization of the avalanche. The typical time constant for a ceramic RPC is 20 ms. The duration of the induction process is a few nanoseconds (see Figure 2.4). Therefore the resistive plates behave as insulators when faced with these discharges. Thus the avalanche is constraint to a very small cylinder in the gas gap. This small region will have its potential decreased until the charges dissipate over its surface and the normal potential on the surface is achieved. This is the main advantage of using resistive plates. Only a very small region is affected by the avalanche while the rest of the detector can operate in a normal way. Thus the rate capabilities are increased.





# 3. Ceramic Composites for RPC Electrodes

## 3.1. The quest for new materials

The importance of the resistive material in the electrodes of a RPC is essential. Together with the gas mixture they define most of the parameters of this kind of detectors. Therefore, the research and development of suitable electrode materials is tightly related to the evolution of RPCs throughout the years. Starting with the first RPC developed in the late eighties, several high-resistive electrode materials have been developed and tested: silica glass (also known as float glass), bakelite, semiconductor-doped glass and ceramics are some of the examples of these materials.

Bakelite as electrode material is used in trigger RPCs due to its low costs. Furthermore, it needs a coating to minimize surface inhomogeneities. Silica glass is used in timing RPCs. The selection of glass for timing RPCs is due to several reasons: *i*) it is possible to build large-scale plates in a cost-efficient way and *ii*) the surface inhomogeneities are negligible when compared with the gas gap width. The silica glass has a bulk resistivity of approximately  $10^{13} \Omega \text{ cm}$ . RPCs with silica glass electrodes are used in experiments such as HADES [23] or FOPI [59] at GSI, HARP [60] or ALICE [61] at CERN. These RPCs, however, cannot be operated at fluxes higher than a few hundred particles per square centimetre and second. This limit can be pushed up to one thousand particles per square centimetre and second if the RPCs are heated, due to the decrease of the bulk resistivity with increasing temperature. For future high-rate experiments, such as the one envisaged by the CBM collaboration, new materials have been developed. An example is the semiconductor-doped glass developed at Tsinghua University. This glass is doped with semiconductor components, lowering the bulk resistivity down to  $10^{10} \Omega \text{ cm}$  and increasing the rate up to  $60 \times 10^3 \text{ cm}^{-2} \text{ s}^{-1}$  [62].

The research of ceramic materials as electrodes for RPC detectors was initiated by Fonte and colleagues [63]. They used a very small sample of  $\text{Al}_2\text{O}_3$  achieving high rate capabilities. Unfortunately, the production of this material was terminated. Thus, it was not possible to test a large-area demonstrator with these ceramics. Afterwards, several groups have been working on ceramic materials like ITEP in Moscow, or HZDR in Dresden both of which will be addressed in this work.

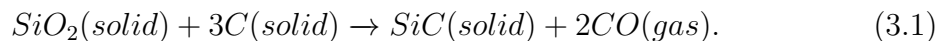
In developing new materials, several parameters must be closely monitored. For example, the bulk resistivity must be such that the RPC can operate at the desired fluxes. The material thickness must be as small as possible to reduce the material budget while at the same time it must ensure the mechanical stability of the electrodes. The radiation hardness must be tested to check the deterioration of the electrodes after operation, etc.

Ceramic composites exhibit many good qualities which makes them good candidates as RPC electrodes. The ceramic manufacturing is a well established technology. They are used in the most demanding environments such as electronics, space-shuttles, and nuclear reactors. Therefore ceramic materials have been proven as radiation hard materials. These results will also be presented in this chapter. Furthermore, the chemical resistance of ceramics is higher than in glass. A higher resistance against HF acid is expected. HF is formed by chemical reactions in the gas mixture during gas discharges. It has been shown that normal glass is extremely sensitive against HF attack, as well as certain types of bakelite [64].

## 3.2. Manufacturing process of ceramic materials

The manufacturing process of ceramic materials is well established by the industry. Depending on the required final characteristics of the ceramic object and its use, there are several routes to reach the final product starting from the powder formation. There is always an ongoing research on these processes to achieve higher purity, better materials, and lower costs, among other reasons. In this section, a very brief description of a general manufacturing cycle is given, based on [65, 66]. This cycle is as follows:

- **Ceramic powder synthesis** is the initial step in the chain. It is used to obtain the desired ceramic chemical composition from initial chemical systems. There are different ways to do this: through solid-state reactions, liquid-state reactions, physical vapour deposition or chemical vapour deposition. As an example, it is possible to obtain SiC through the solid-state reaction at more than 2500 °C



This initial step allows the manufacturer to specify the purity, particle size distribution and other parameters of the powder.

- **Powder compactation** involves high pressure and sometimes high temperature. It compacts the initially loose powder into a more compact body. Two different methods can be singled out. Uni-axial dry pressing uses pressure on a single axis to compact the powder. It is a highly efficient method, however it can lead to density variations on the system, specially in large ceramic pieces. Isostatic dry pressing uses a container placed inside a larger one filled with pressurized liquid. This way, the compactification is performed homogeneously around the ceramic shape. Both methods required a previous granularization of the powder due to the high flowability characteristics of fine powder.
- **Sintering** results in the densification of the powder in its final bonding system. High temperatures and pressures are used typically to achieve a compact ceramic piece. In this process, defects in the material are accentuated, therefore it is very important to have obtained a good quality powder in the previous steps. Depending on the final properties of the system, several sintering processes are available. It will be shown

in this chapter, how the bulk resistivity of the ceramic composites is dependent on the sintering temperature and duration.

- **Finishing** is the last step in the manufacturing chain. The ceramic pieces are mechanically milled or polished to achieve the final desired shape. The main drawback of this process is the increase of the costs of the ceramic piece. All the material which is milled is discarded, and sometimes, due to the hardness of the ceramic, cutting of the pieces is a challenge. The latter process can involve as much as 60-80% of the final costs.

### 3.3. Characterization of $\text{Si}_3\text{N}_4/\text{SiC}$ ceramics

$\text{Si}_3\text{N}_4/\text{SiC}$  composites are advanced ceramic materials with many applications, specially those requiring high temperature in excess of  $1500^\circ\text{C}$ . In these composites,  $\text{Si}_3\text{N}_4$  acts as a matrix substrate with SiC added as a doping component. Depending on the composition, the final parameters of the ceramic material can be modified.

#### 3.3.1. Mechanical properties

A photograph of a ceramic wafer during a manufacturing cycle is exhibited in Figure 3.1. After the full cycle, the wafer is cut into plates.  $\text{Si}_3\text{N}_4/\text{SiC}$  ceramic sheets appear a grey colour; the good optical reflection due to the surface polishing is shown in Figure 3.2. These plates have dimensions ranging from  $2\times 2\text{ cm}^2$  up to  $20\times 20\text{ cm}^2$ . All these plates have a thickness of 2 mm.

Mechanically, these plates are very stable, resistant to deformation and scratches. This property is of the utmost importance. Due to the high fields which a RPC gap is subjected to, special care must be taken into the homogeneity of the gas gap. A small deformation can change drastically the local electric field strength, facilitating the formation of streamers and/or discharges. The material can be then subjected to an extra stress, which can lead to damage in the material or, in the worst case, it can lead to the breakdown of the detector.

#### 3.3.2. Bulk resistivity

One the most attractive properties of  $\text{Si}_3\text{N}_4/\text{SiC}$  ceramic composites its the possibility of tuning the bulk resistivity of the material during the manufacturing process. There are two methods to achieve this goal: either by modifying the SiC weight in the mixture or by modifying the temperature and duration of the sintering phase. It will be shown here, how these two processes allow for the modification of the bulk resistivity by several orders of magnitude.

#### Experimental set-up for resistivity measurements

To facilitate the characterization of the bulk and surface resistivity of materials a dedicated set-up has been implemented [67]. A detailed scheme is shown in Figure 3.3. The

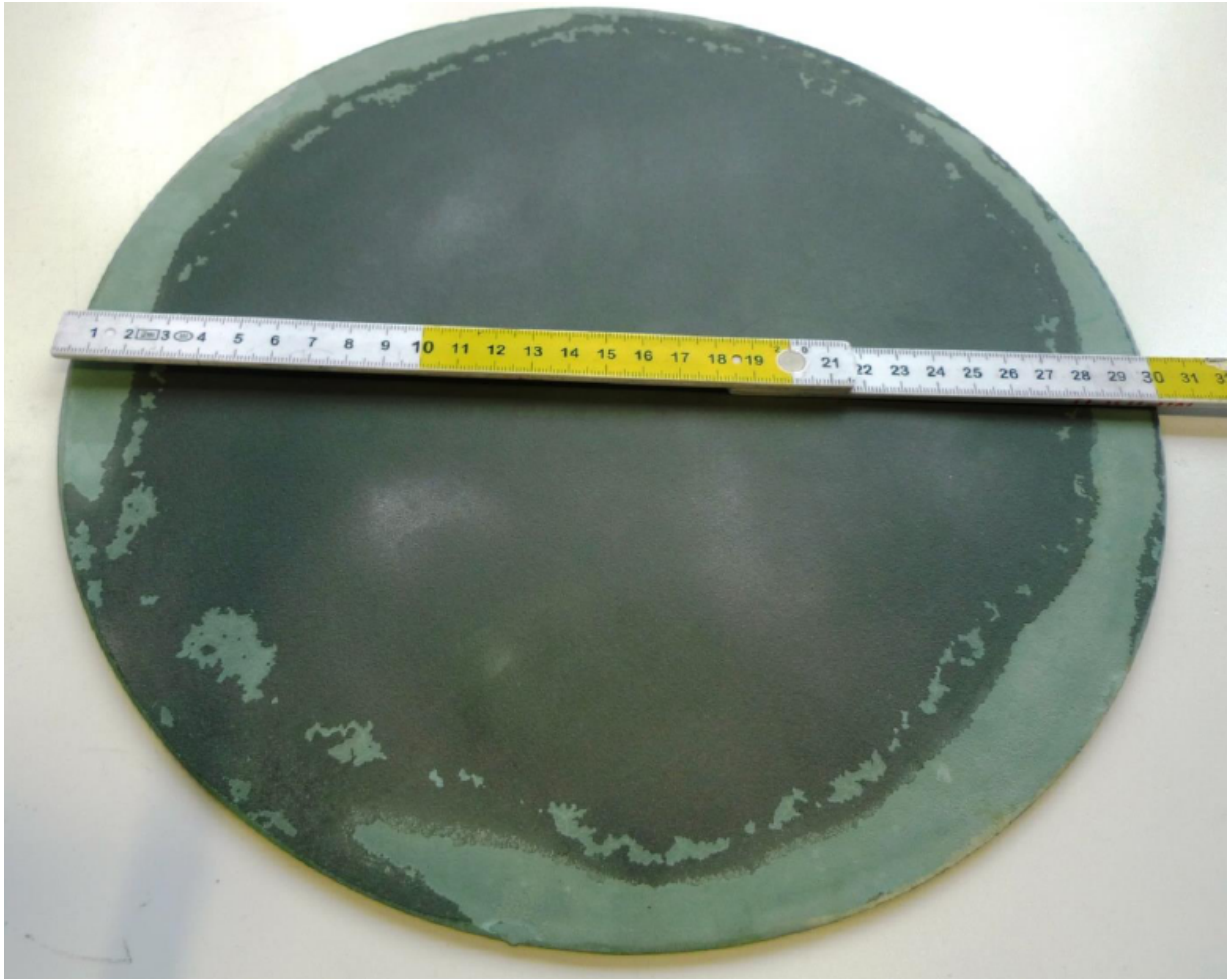


Figure 3.1.: A Si<sub>3</sub>N<sub>4</sub>/SiC ceramic wafer during manufacturing. The picture was taken after the compactation step. This picture was provided by the Fraunhofer Institute for Ceramic Technologies and Systems, IKTS, in Dresden.

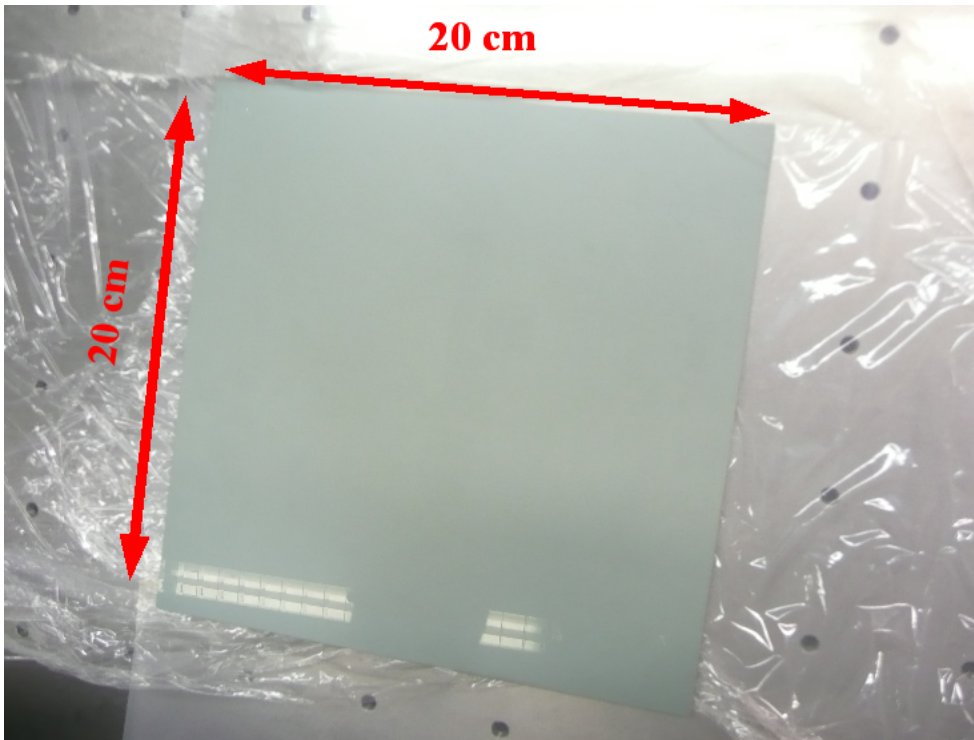


Figure 3.2.: A  $20 \times 20 \text{ cm}^2$  ceramic plate after delivery. The surface is so well polished that reflections are created on the plate by the room lighting in the lower part of the plate. The interruption of the light reflection corresponds to the shadow of the photographer. This plate was used as an electrode in an HZDR RPC prototype.

main component is a Keithley 485 pico-ammeter<sup>1</sup>, which can supply up to 1000 V to the measurement probe and provides a current measurement with a precision of 0.1 pA [68]. A external voltage supply can also be used when studies at higher voltages are needed. The material under study is mounted in a support. The probe is placed on the same position on both sides of the ceramic plate. It is composed of three rings of conducting material. One ring is on one side of the probe. Two rings are on the other side. From these to rings, the external one acts as a protection electrode while the central one is the measurement electrode. A voltage is applied and the current flowing through the material measured. The results are monitored on a laptop using Labview supplied by the pico-ammeter manufacturer. At the same time, a table with the results is recorded for the off-line analysis.

The bulk resistivity is calculated as

$$\rho = R \frac{S}{d} = \frac{V S}{I d}, \quad (3.2)$$

where  $R = V/I$  is the resistance of the volume in which the current  $I$  flows due to a voltage

<sup>1</sup>pico-ammeter is the commercial brand of pico-amperemeters developed by Keithley

$V$ . This volume is given by the area  $S$  of the measuring electrode and the plate thickness  $d$ .

With this set-up, the bulk resistivity dependence on the voltage, the time and the cleaning process was studied. The complete procedure is described in the following.

1. The ceramic plates are first visually inspected for scratches, broken corners or any defect that can render them unusable. A first measurement is taken from some of the plates to check the order of magnitude in which the bulk resistivity lies.
2. A cleaning of the plates is performed. It is done in an ultrasonic bath with ionized water for a few hours. After this, the plates are heated at 150 °C for another few hours and left to cool down overnight.
3. The bulk resistivity is measured for each plate. Four equidistant points are selected and each of them is measured twice. The analysis is performed calculating the average for each point and then an average on the whole plate. For quality assurance purposes, some plates are measured in five to nine different points.

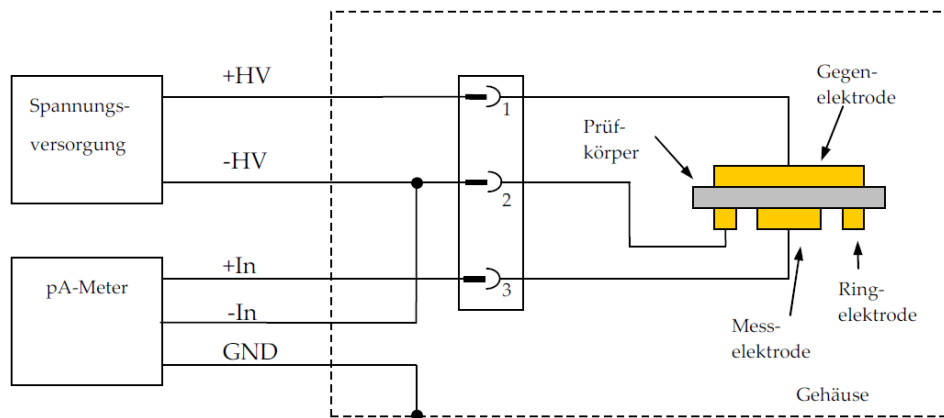


Figure 3.3.: A scheme representing the measurement set-up employed for determining the bulk resistivity. A full description is given in the text. From [67].

To better understand the surface of the plates, several samples are selected and inspected under a microscope. Figure 3.4 is a collection of observations during this process. The top panels show a fibre on the surface of the plate. This kind of pollution on the plates can be avoided by treating them in a clean room. It is important to ensure that the surface is free of such pollution elements due to the high fields employed in RPCs. If one of these fibres is located in the gas gap, it will create a distortion in the field and produce a spark inside the detector rendering it unusable until it is repaired. The middle left panel shows two dirty spots which require cleaning. The middle right panel shows a darker region in the plate. This is not a dirty point on the surface but a different colouring of the material. A slightly lower bulk resistivity is associated to these darker regions. However, the difference

is tolerable. The bottom panels show a broken section in the plate. This occurred during manufacturing process and was marked as defect immediately. These six pictures represent a few examples of how microscopic imaging can be used as a tool for quality control of electrodes. In Chapter 4, it will be shown how the microscope images can be used to explain different phenomena that occur inside the gas gap during operation.

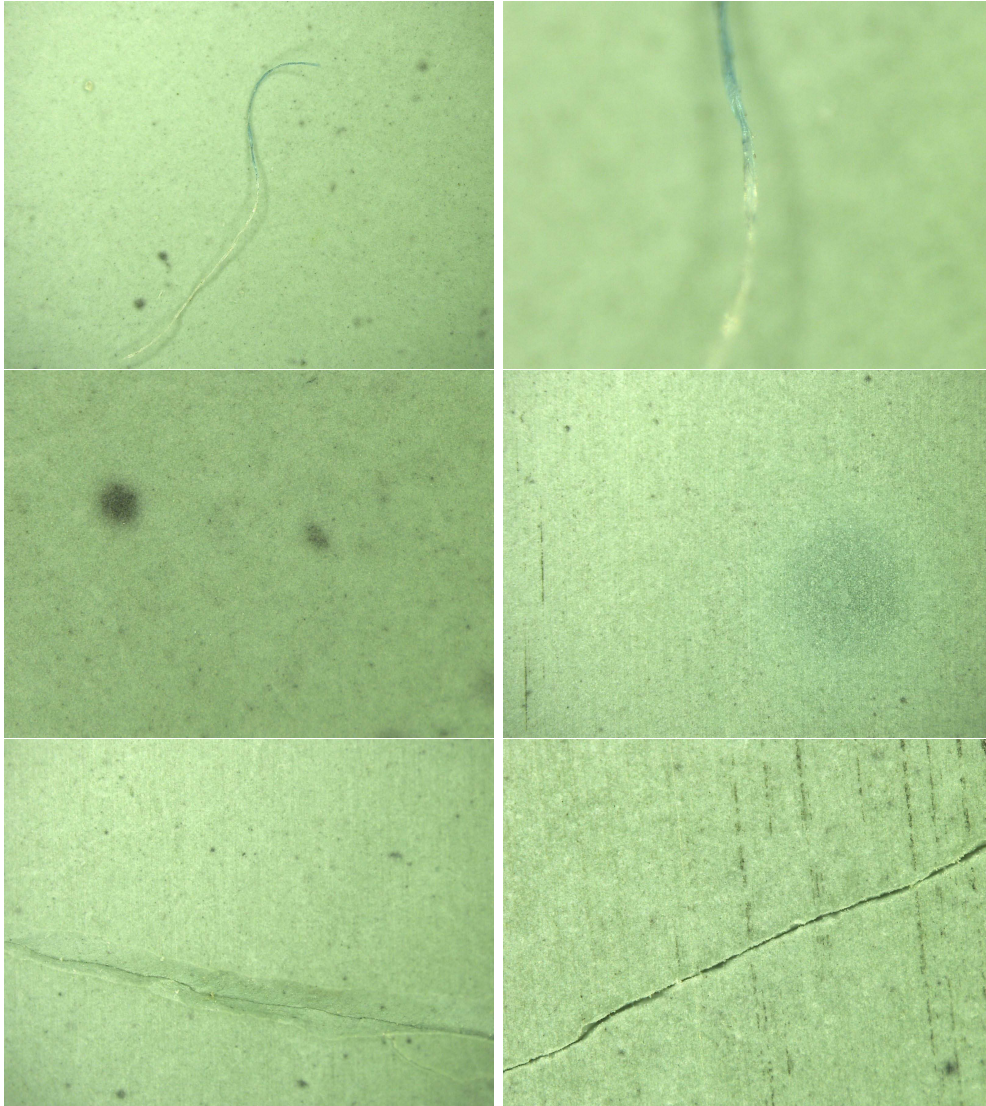


Figure 3.4.: Microscope images of ceramic plates. Each picture has dimensions  $3.15 \times 2.35$  mm. Upper left panel: A fibre lying on a ceramic plate. Upper right panel: A magnified picture of the fibre. Middle left panel: Two dirty spots on the plate which required posterior cleaning. Middle right panel: A darker region in the plate. It is identified as intrinsic to the plate and not dirt deposited on the surface. Lower left panel: A deep and wide broken region in a plate. Lower right panel: A broken area formed during manufacturing.

After all these tests, the plates are deemed suitable for RPC operation if their bulk resistivity lies in the range of  $10^9$ - $10^{10}$   $\Omega$  cm and have passed all the inspections.

### Dependence on composition

The dependence of the bulk resistivity on the composition can be understood by means of percolation theory. When an insulator matrix, in this case  $\text{Si}_3\text{N}_4$ , is mixed with a filler, SiC, electrical conducting paths can be formed throughout the material, modifying the response of the composite and its electrical properties. This has been studied in detail and the results can be found in [69]. The basic idea is that conductive paths can be formed in the material with the addition of sufficient semiconductor material to the insulator matrix. The higher the weight of this component in the mixture, the higher the probability that the charge carriers will find paths to traverse the material. This effectively lowers the bulk resistivity.  $\text{Si}_3\text{N}_4/\text{SiC}$  ceramics have electronic conductivity.

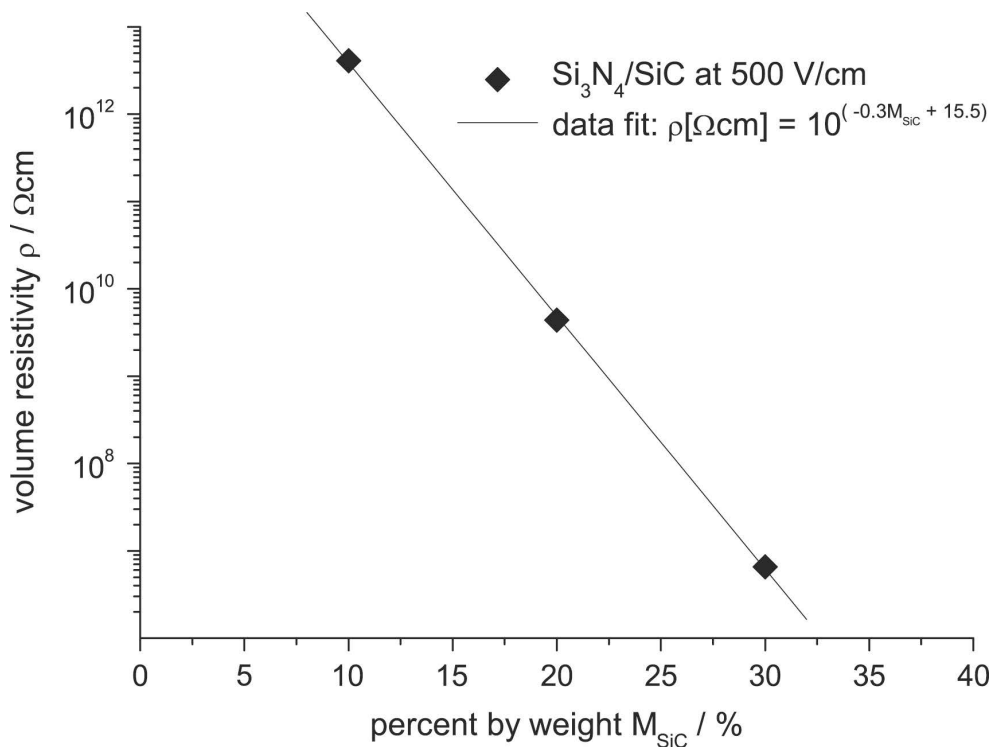


Figure 3.5.: Bulk resistivity dependence on the SiC weight [70].

The dependence of the bulk resistivity on the weight percentage of SiC is shown in Figure 3.5. This was measured after a full manufacturing cycle in which only the percentage by weight was changed. This plot shows that for a desired bulk resistivity of  $5 \times 10^9 \Omega\text{cm}$  approximately 20% of the mixture should be SiC.

### Dependence on sintering time and temperature

As mentioned above, during the sintering process, the ceramics are subjected to high temperatures to consolidate the ceramic powder. During this process, impurities present in the material are eliminated. These impurities are intrinsic to the method of powder developing and are typically products from the chemical reactions used to obtain the



initial crystals or for bonding the different components. In Figure 3.6 the dependence of the bulk resistivity on the sintering time and temperature is displayed. It shows that the bulk resistivity can change several orders of magnitude depending on these parameters. The sharp increase due to temperature can be explained. The impurities will acquire a kinetic energy due to the temperature. If this kinetic energy is high enough, over a certain threshold, the impurities will exit the material. This translates in a sharp change in the bulk resistivity. This change is so drastic that a careful control on the sintering process is needed to obtain the desired parameters.

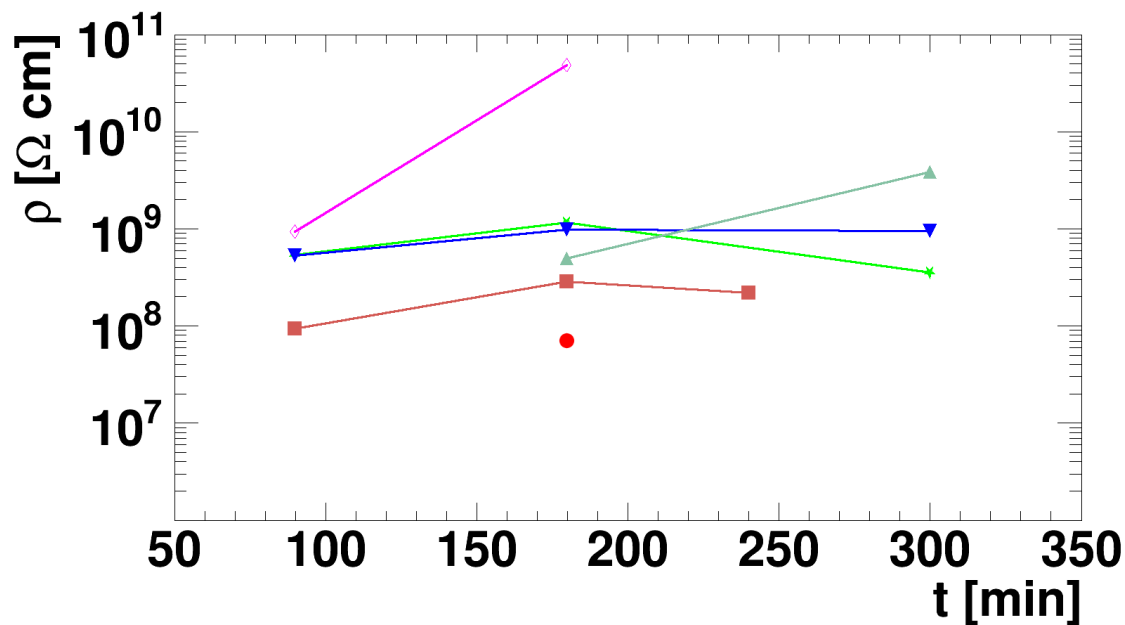


Figure 3.6.: Bulk resistivity  $\rho$  as a function of the sintering process duration  $t$ . The dependence was studied for different temperatures:  $\bullet$  correspond to  $T = 700^\circ\text{C}$ ,  $\blacksquare$  to  $T = 800^\circ\text{C}$ ,  $\star$  to  $T = 850^\circ\text{C}$ ,  $\blacktriangledown$  to  $T = 900^\circ\text{C}$ ,  $\blacktriangle$  to  $T = 950^\circ\text{C}$  and  $\blacklozenge$  to  $T = 980^\circ\text{C}$ .

### Dependence on voltage

$\text{Si}_3\text{N}_4/\text{SiC}$  ceramic composites present a varistor behaviour. A varistor-type material has a non-linear, or diode-like, voltage current characteristic. This means that the bulk resistivity depends on the voltage to which the material is subjected. Typically, the current-voltage characteristic curve (I-V curve) of a varistor, under normal operation conditions, will take the form<sup>2</sup>

<sup>2</sup>In general, the I-V curve presents three regions depending on the voltage interval: *i*) a pre-breakdown region at low voltages, *ii*) a normal operation region at intermediate voltages and *iii*) a up-turn region

$$I \sim I_0 V^\kappa, \quad (3.3)$$

where  $I_0$  is the current when the voltage applied is 1 V and  $\kappa$  is a coefficient intrinsic to the varistor under study depending on many factors.

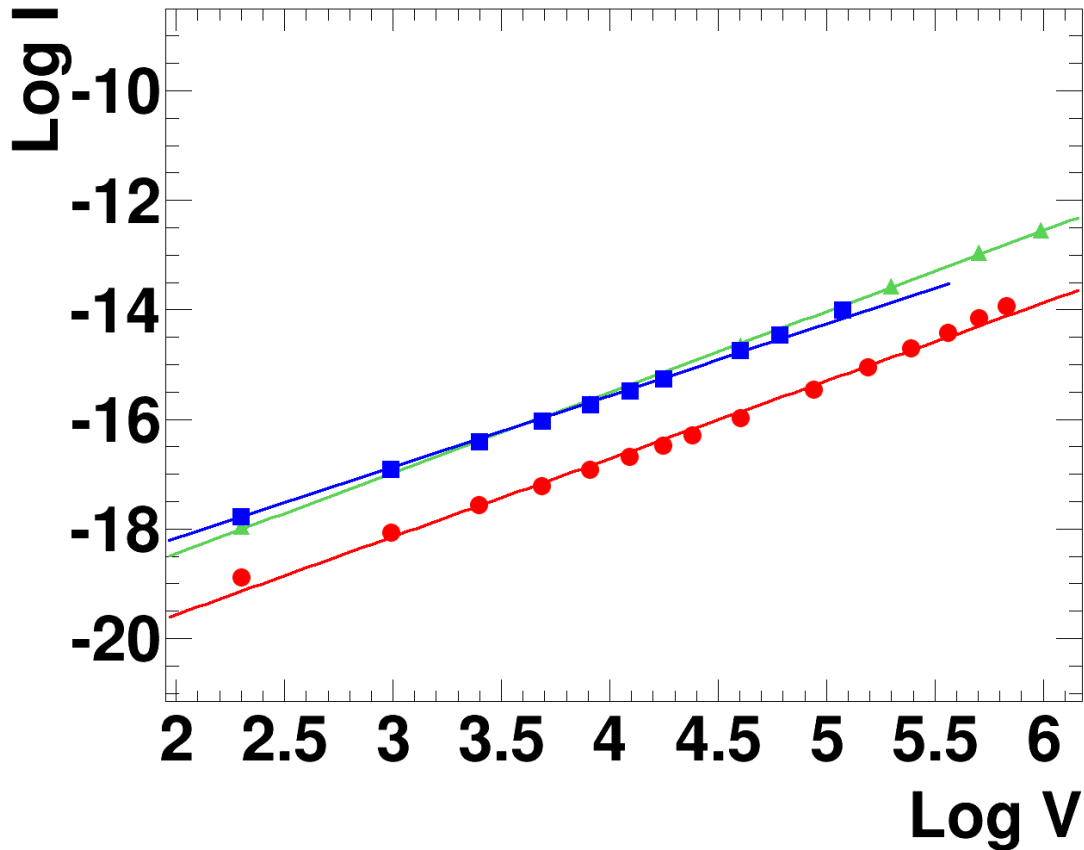


Figure 3.7.: Logarithm of the current  $I$  versus the logarithm of the voltage  $V$  for a test plate ▲ and two plates (●: plate #7, ■: plate #10) previously implemented into a RPC. The voltage is in volts and the current in microamperes.

In Figure 3.7, the current-voltage characteristic is shown. The logarithm of the current against the logarithm of the voltage for three plates is plotted. This plot shows clearly that the current and voltage do not have a linear correlation. The continuous lines represent a linear fit to

$$\ln I = p_0 + p_1 \ln V, \quad (3.4)$$

where  $p_0$  and  $p_1$  are two free parameters to be extracted from the fit. The parameters  $p_0$  and  $p_1$  relate to  $I_0$  and  $\kappa$  as

---

at high voltages. The voltage ranges are specific for each material.

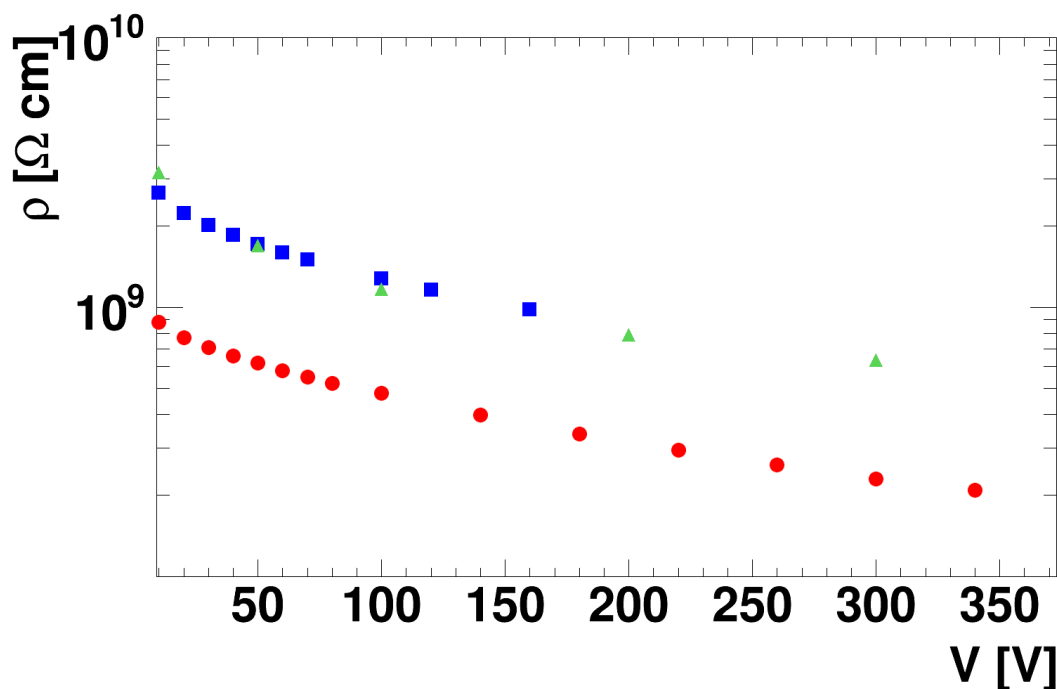


Figure 3.8.: Bulk resistivity dependence on the applied voltage for the same plates as in Figure 3.7.

$$p_0 = \ln I_0, \quad (3.5)$$

$$p_1 = \kappa. \quad (3.6)$$

This allows to extract a parametrization of the I-V curve for the ceramic plates used in RPCs. Putting together (3.2) and (3.3) a parametrization for the bulk resistivity as a function of the voltage is

$$\rho = \frac{V^{1-\kappa} S}{I_0 d}. \quad (3.7)$$

This parametrization will become important when calculating the electric field strength in the gas gap during irradiation. This will be discussed in Chapter 6.

In Table 3.1 the results of the fits are shown. All the values are larger than one. Specifically, one can obtain an averaged value for this material of  $\kappa = 1.381596 \pm 0.00011$ . The values of  $I_0$  are normalized to the surface unit. The parameter  $\kappa$  seems to be universal to the plates, indicating that the varistor behaviour is the same for all the analyzed plates. The parameter  $I_0$  changes with the intrinsic bulk resistivity of the plates.

This non-linear dependence is directly shown in Figure 3.8. In a perfect ohmic material, the bulk resistivity remains constant over the voltage range. In the  $\text{Si}_3\text{N}_4/\text{SiC}$  material, the bulk resistivity varies with the voltage nearly one order of magnitude. There are several

| Plate | $I_0$ [nA] | $\kappa$          |
|-------|------------|-------------------|
| test  | 0.58       | $1.475 \pm 0.017$ |
| 07    | 0.18       | $1.422 \pm 0.032$ |
| 10    | 1.02       | $1.300 \pm 0.015$ |

Table 3.1.: Values of  $I_0$  and  $\kappa$  obtained from the fits of eq. (3.4) to the data exhibited in Figure 3.7.

things to consider when addressing this effect. First and foremost, the bulk resistivity *decreases* with the increasing potential difference between the plate faces. For the purposes of high-rate RPCs this is not a problem. A lower resistivity means a higher rate capability. However the dark currents in the detector and the dark counting rate also increase.

#### Dependence on plate operation temperature

A possible way of decreasing the bulk resistivity of a material is to increase its temperature. The bulk resistivity changes with the temperature following the Arrhenius law

$$\log(\rho) = a + \frac{b}{T}, \quad (3.8)$$

where  $a$  and  $b$  are two parameters intrinsic to the material and  $T$  is the temperature. For narrow temperature intervals this can be expressed as

$$\rho \approx 10^{(T_0 - T)/\Delta T}, \quad (3.9)$$

with  $\rho_0$  the bulk resistivity at a reference temperature  $T_0$  and  $\Delta T$  the temperature variation required to decrease the bulk resistivity one order of magnitude. This effect has been measured for  $\text{Si}_3\text{N}_4/\text{SiC}$  ceramics [71]. The value of  $\Delta T$  is in the range of 29-41° C depending on the plate construction process. Several studies on float glass have revealed that the temperature interval for this material is  $\Delta T = 25^\circ \text{C}$  [72, 73].

The rate capabilities of RPCs with warmed electrodes have been investigated in the case of float glass electrodes [58, 74]. In these cases, the performance of the RPCs improved with higher temperatures. It was shown that increasing the electrode temperature by 25° C increased the rate capabilities by one order of magnitude.

Warming of the plates in large-scale detectors has several drawbacks: *i*) the most common way of warming-up is using hot water, which has a risk of having leaks and might be disastrous in contact with electronics, *ii*) the temperature has to be kept constant and homogeneous, something difficult on a large-scale detector, *iii*) some systems use flammable gases, *iv*) the heavy weight of a large-scale cooling system and *v*) higher temperatures induce faster ageing on materials. Therefore, the most effective way to increase rate capabilities is using low resistive materials as electrodes.

### Bulk resistivity in mass production

During mass production, two main factors are systematically studied: the variation of the bulk resistivity across the surface of each plate and the variation from one plate to another. A homogeneous bulk resistivity over the plate is important due to its relation to the potential drop in the plate. The RPC should operate at the same electric field strength for any rate.

The bulk resistivity over nine points equally spaced on a  $20 \times 20 \text{ cm}^2$  plate is shown in Figure 3.9. The maximum variation is approximately a factor 6. Typically the variation of the bulk resistivity over the surface of the plates was 2-6 depending on the quality of the plate. By optical inspection, several darker areas were observed in some plates (a microscope image was shown above in Figure 3.4, middle right panel). When measuring the bulk resistivity of these areas it was recognized that they show systematically a lower bulk resistivity than normal areas in the plates at room temperature.

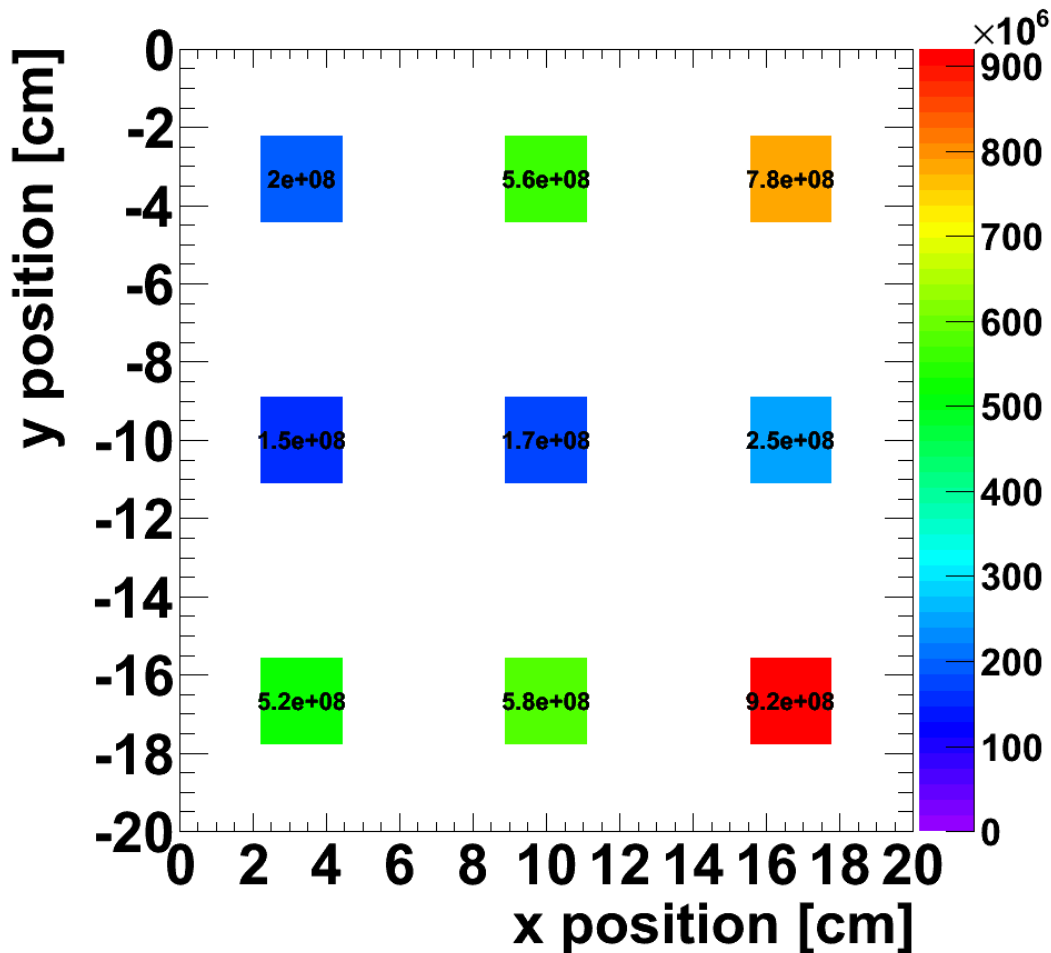


Figure 3.9.: Bulk resistivity measured over nine points on the surface of a plate.

#### Thin ceramic plate samples

Due to the excellent results obtained with ceramic RPCs [42, 71], thin samples were built and their bulk resistivity measured. Three small probes were manufactured. The probes had a surface of a few square centimetres and thickness smaller than  $200\ \mu\text{m}$ . The purpose of such thin plates would be to build a low-material budget RPC which could be used as start or trigger detector in high-energy experiments. In Figure 3.10 the results of the measurements are shown. The bulk resistivity is in the order of  $10^9\ \Omega\text{cm}$ . Based on the results of prototypes with electrodes with the bulk resistivity in the same range, a RPC built with plates with this thickness would potentially be able to withstand fluxes in the order of  $10^5\ \text{cm}^{-2}\ \text{s}^{-1}$ . These results will be discussed in Chapter 6.

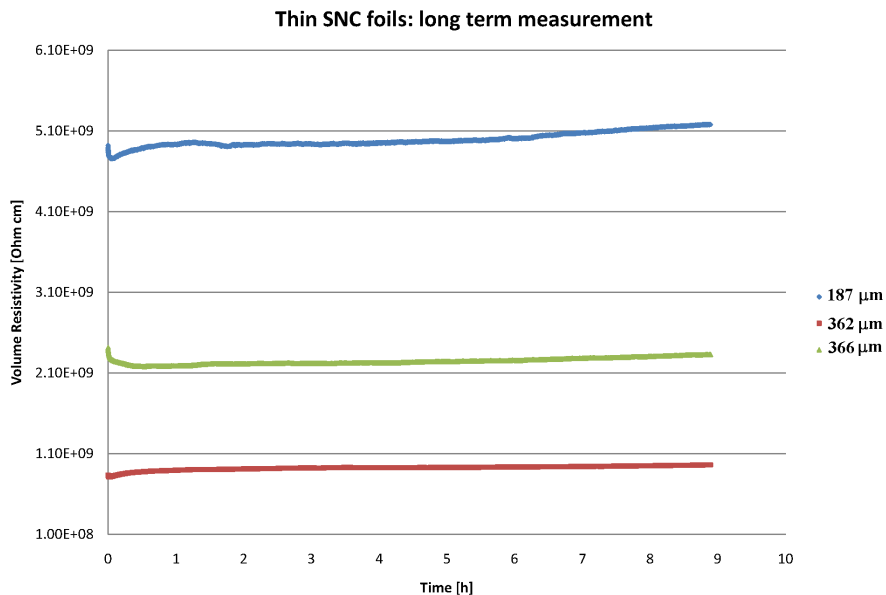


Figure 3.10.: Bulk resistivity as a function of time for three thin ceramic probes with different thicknesses. The thickness of each probe is indicated in the legend.

#### 3.3.3. Electrical parameters

As explained in Section 2.3.3 the signal in an RPC is formed by induction of the moving charges of the avalanche on the pick-up electrodes. Then the signal is propagated to the read-out points and the read-out electronics. Due to the nature of this phenomena and the RPC architecture, a few electrical issues must be addressed. Effects like cross-talk, charge-sharing and signal degradation can be important in this stage and a non-suitable read out scheme can make the detector unusable.

In a dielectric material, the dielectric permittivity can be expressed in terms of a real and imaginary part:

$$\epsilon = \epsilon_0(\epsilon'_r + i\epsilon''_r), \quad (3.10)$$

where  $\epsilon_0$  is the dielectric permittivity of vacuum,  $\epsilon'_r$  the real part and  $\epsilon''_r$  the imaginary part. Both the real part and imaginary part of the permittivity can be related to physical phenomena in the material when it is exposed to alternating fields. In particular,  $\epsilon'_r$  and  $\epsilon''_r$  are related to the material dipoles alignment with the electric field and the storage and loss of energy within the medium. The dependence of these parameters on the frequency of the applied field can be very complex.

For the RPC regime, where the signal rise-time amounts up to a few hundred picoseconds, the cut-off frequency can be as high as 3 GHz. The electronics employed by the ceramic RPCs was developed for the FOPI Collaboration (see Section 4.4.1) and have a bandwidth of approximately 1.5 GHz. Thus for our purposes, a study in the lower microwave range (0.1 - 5 GHz) suffices [75].

The experimental procedure can be found in [75]. A wide copper strip (where “wide” means that the signal line is much wider than its distance to the return line) was pasted over the ceramic plate and connected on both sides to a network analyser. The network analyser sends impulses from one line, the emission line, to another, the return line. With this, the transmission and reflection coefficients of the network can be determined. In this 1+1 line configuration, the signal transmission,  $S_{12}$ , can be expressed as

$$S_{12}(f) = \frac{(2 - T)T}{1 - (1 - T)^2 e^{-2\gamma D}} e^{-\gamma D}, \quad (3.11)$$

where in this case  $T$  is the transmission coefficient,  $D$  is the line width and  $\gamma$  the phase constant. An example of the measurement of  $|S_{21}|$  is shown in figure 3.11. There one can see the trend of decreasing transmission with increasing frequency as well as an oscillatory pattern due to impedance mismatch. The inter peak distance can be determined as

$$\Delta f = \frac{v}{2D} = \frac{c}{2D\sqrt{\epsilon'_r}}, \quad (3.12)$$

where  $v$  is the propagation velocity in the medium (as measured in [42]) and  $\epsilon'_r$  is the real part of the relative permittivity. With this and neglecting fringe fields, the cut-off frequency, corresponding to a 3 dB drop in the transmission, can be estimated as

$$f_c \approx \frac{v \log 2}{2\pi D \tan \delta}, \quad (3.13)$$

where  $\tan \delta$  is the tangent loss. Together, eqs. (3.12) and (3.13) provide the framework to calculate the relative permittivity and tangent loss from experimental data. The results for  $\text{Si}_3\text{N}_4/\text{SiC}$  are shown in Table 3.2 together with float glass material common in traditional low-rate RPCs.

The tangent loss of ceramic materials is higher than for commons glass, thus one must expect a higher loss of signal height when it is transported through the line to the front end electronics. The difference in relative permittivity will affect the weighting field. The

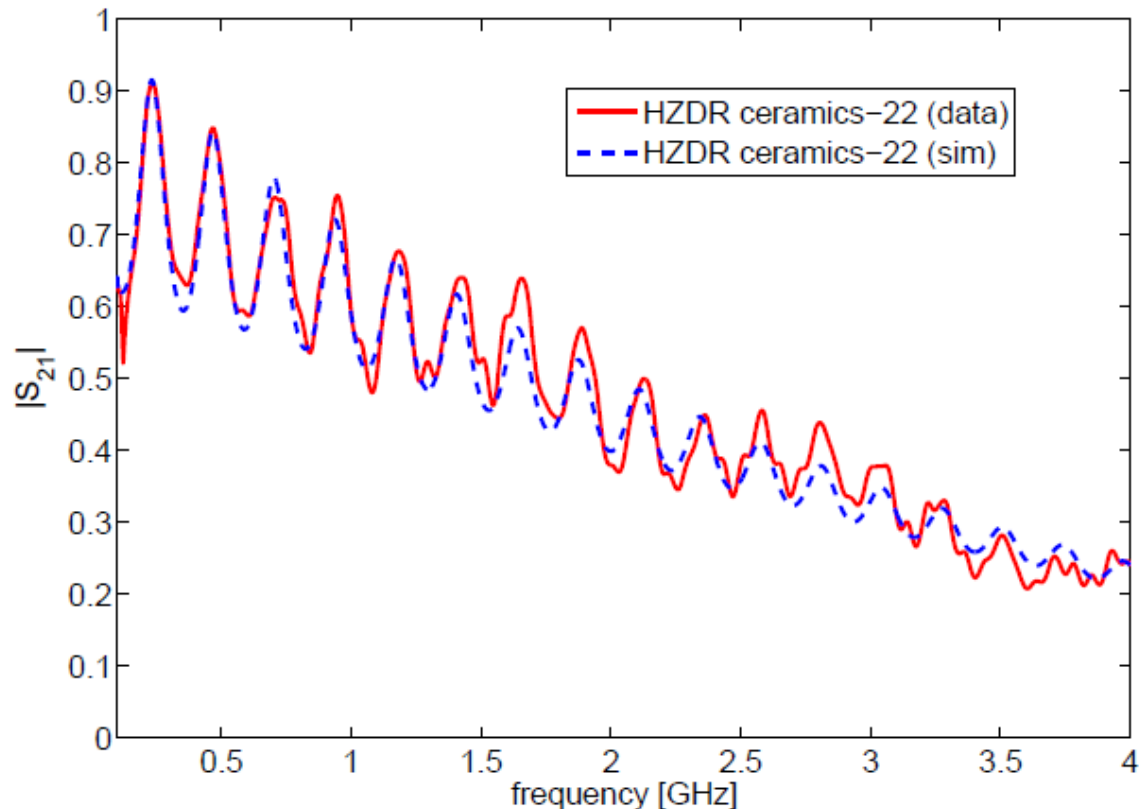


Figure 3.11.: Transmission coefficient  $|S_{21}|$  as a function of the signal frequency for a line on a ceramic plate. The continuous red line is the data measured with a network analyser and the blue dashed line correspond to a simulation. The plate under test was #22.<sup>3</sup>

combination of the two effects results in a lower induced charge in ceramic RPCs than glass RPCs. This will be discussed in Chapter 6.

### 3.3.4. Radiation hardness

Given the purpose of ceramic RPCs as detector in high irradiation and extremely demanding environments, it is necessary to prove the ability of the material to cope with the worse aspects of ionizing and non-ionizing irradiation. In heavy ion collisions like the ones planned at the FAIR facility by the CBM collaboration, the radiation level can be so high at selected positions as to damage the material itself by breaking up the bonds of the molecules and generating defects in its crystal structure. This is especially dangerous for the electronics employed to read out the signals (by a FPGA device, for example) exposed to this environments.

As a reference, the CBM radiation levels as calculated in [31] are shown in Table 3.3. Detailed simulations were performed with FLUKA to understand the radiation environ-



| material          | $\epsilon_r$   | $\tan \delta$     |
|-------------------|----------------|-------------------|
| ceramic plate #16 | $12.2 \pm 0.3$ | 0.03              |
| ceramic plate #22 | $12.2 \pm 0.3$ | 0.033             |
| float glass       | $5.8 \pm 0.5$  | $0.025 \pm 0.005$ |

Table 3.2.: Dielectric constant  $\epsilon_r$  and tangent loss  $\tan \delta$  for  $Si_3N_4/SiC$  composites and float glass.

| detector | Dose (Gy/year) | NIEL ( $n_{eq}/cm^2/year$ )        |
|----------|----------------|------------------------------------|
| ToF      | 1 - 100        | $10^{10} - 10^{11}$                |
| TRD      | 0.5 - 100      | $8 \times 10^8 - 5 \times 10^{11}$ |
| PSD      | $8 - 10^4$     | $5 \times 10^{12} - 10^{14}$       |

Table 3.3.: Radiation dose calculated for several CBM detectors: the Time-of-Flight wall (ToF), the Transition Radiation Detector (TRD) and the Projectile Spectator Detector (PSD) [31].

ment, specially the non-ionizing energy dose deposited on the detectors (see Section 1.3 footnotes for an explanation of this dose). The goal is to determine the radiation hardness of the materials required to operate throughout the complete CBM measurement program. Neutron irradiation, together with alpha particles, fission fragments and heavy ions are considered the most damaging radiation to organic and inorganic materials. This radiation can interact with the nuclei from the material themselves and break them up, fundamentally changing the composition of the material.

To test radiation hardness two plates of  $Si_3N_4/SiC$  ceramic material and two plates of  $Al_3O_4$  ceramics of size  $5 \times 5 \times 0.2 \text{ cm}^3$  were sent to Forschungsreaktor München (FRM-II). They were irradiated with a neutron flux of  $10^{13} n_{eq}/cm^2$  in the MEDAPP channel. The neutron energy was in the range 0.1 - 10 MeV. The bulk resistivity was measured before and after the irradiation following the protocol described in Section 3.3.2. After irradiation, the plates were optically inspected and no discernible changes were appreciated. The bulk resistivity was measured for 3600 seconds to ensure that saturation was reached. The bulk resistivity of the  $Si_3N_4/SiC$  ceramic plates decreased by a factor of 0.6 with respect to the measurement prior to the irradiation.

This study is not complete however. To further understand this property of this particular ceramic composites, systematic studies with different neutron fluxes are needed.

### 3.4. Characterization of $Al_2O_3$ ceramics

In collaboration with the Institute for Theoretical and Experimental Physics (ITEP), Moscow, several plates of  $Al_2O_3$  material with a chromium evaporated layer on top of it were developed and their properties measured. In [76] the properties of a previous prototype are discussed.  $Al_2O_3$  is characterized by a high bulk resistivity, typically  $10^{14} -$

$10^{15} \Omega \text{ cm}$ . This is clearly too high for its usage in RPCs. A clever solution was achieved by evaporating a small layer of chromium on its surface.

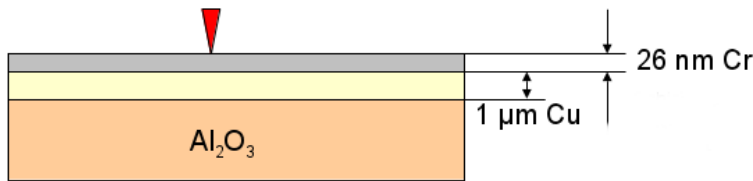


Figure 3.12.: A scheme of the different layers ( $\text{Al}_2\text{O}_3$  ceramic substrate, copper layer and chromium layer) in an  $\text{Al}_2\text{O}_3$  plate for RPC construction.

This solution is not trivial, however, and the formation process requires a detailed explanation. In Figure 3.12 a cross section of a plate is shown. The  $\text{Al}_2\text{O}_3$  ceramic forms the bulk of the material. Over it, a  $1 \mu\text{m}$  copper layer is deposited through evaporation. This is needed to be able to keep the chromium pasted to the ceramic and prevent the possible holes that appear in the chromium layer during the evaporation process from reaching the ceramic substrate. Over the copper a chromium layer is then deposited. This layer is so thin that it lowers the bulk resistivity but does not eliminate the resistive component that keeps the avalanche under control. The evaporation process is not perfect, and small imperfections can be seen when examining the plate with a microscope<sup>4</sup>. They are a few nanometres wide and several hundred nanometres deep. However, no negative effect on the performance has been correlated to them. Figures 3.13 and 3.14 show microscope images of the metallic layer. The dark spots in Figure 3.13 are holes in the chromium layer. In Figure 3.14, a roughness analysis is shown where the total difference in height is approximately 40 nm.

Another important characteristic is the shape of the plate, specially designed to reduce edge electric fields. This will be discussed in Chapter 4.

---

<sup>4</sup>Special thanks to Dr. B. Schmidt (Ionenstrahlzentrum at HZDR) for the detailed study of the surface of the  $\text{Al}_2\text{O}_3$  plates.

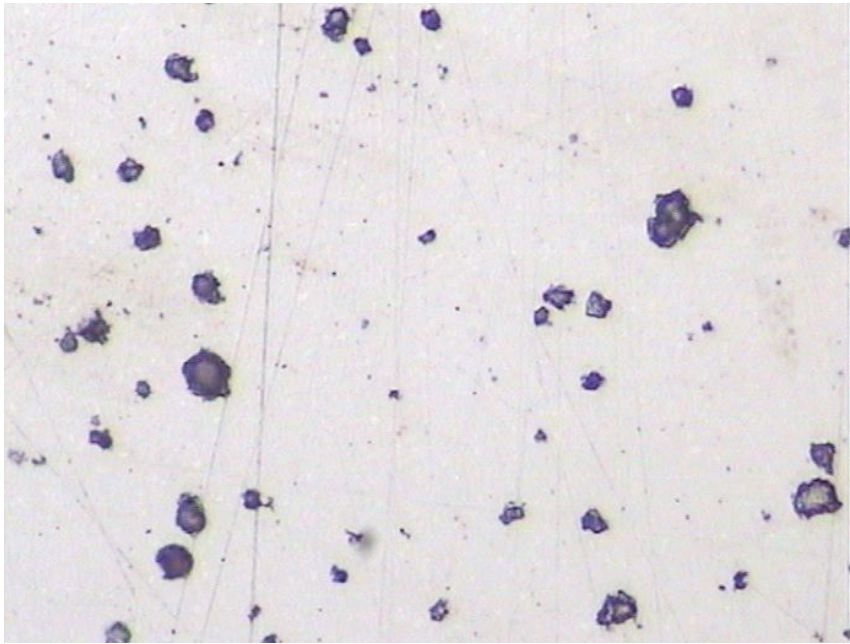


Figure 3.13.: Microscope picture, about  $2 \times 3 \text{ mm}^2$ , of the metallic surface deposited over the  $\text{Al}_2\text{O}_3$  ceramic.

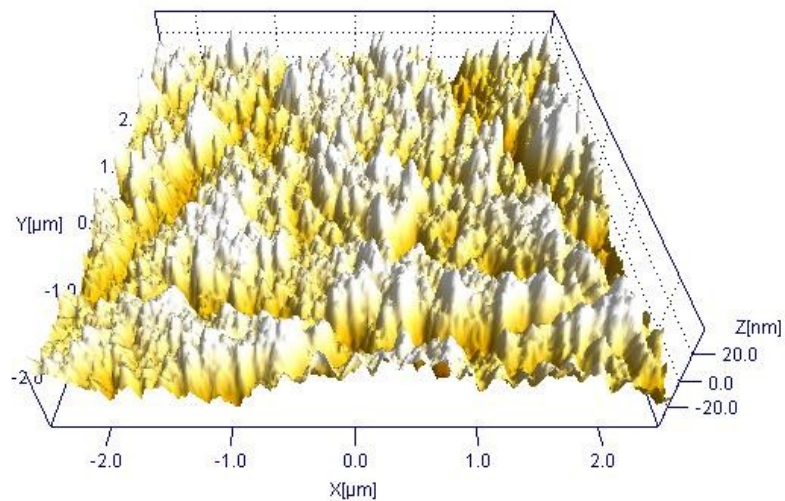


Figure 3.14.: Roughness of the chromium layer with a copper substrate on the  $\text{Al}_2\text{O}_3$  plate.



## 4. Ceramic Detector Prototypes

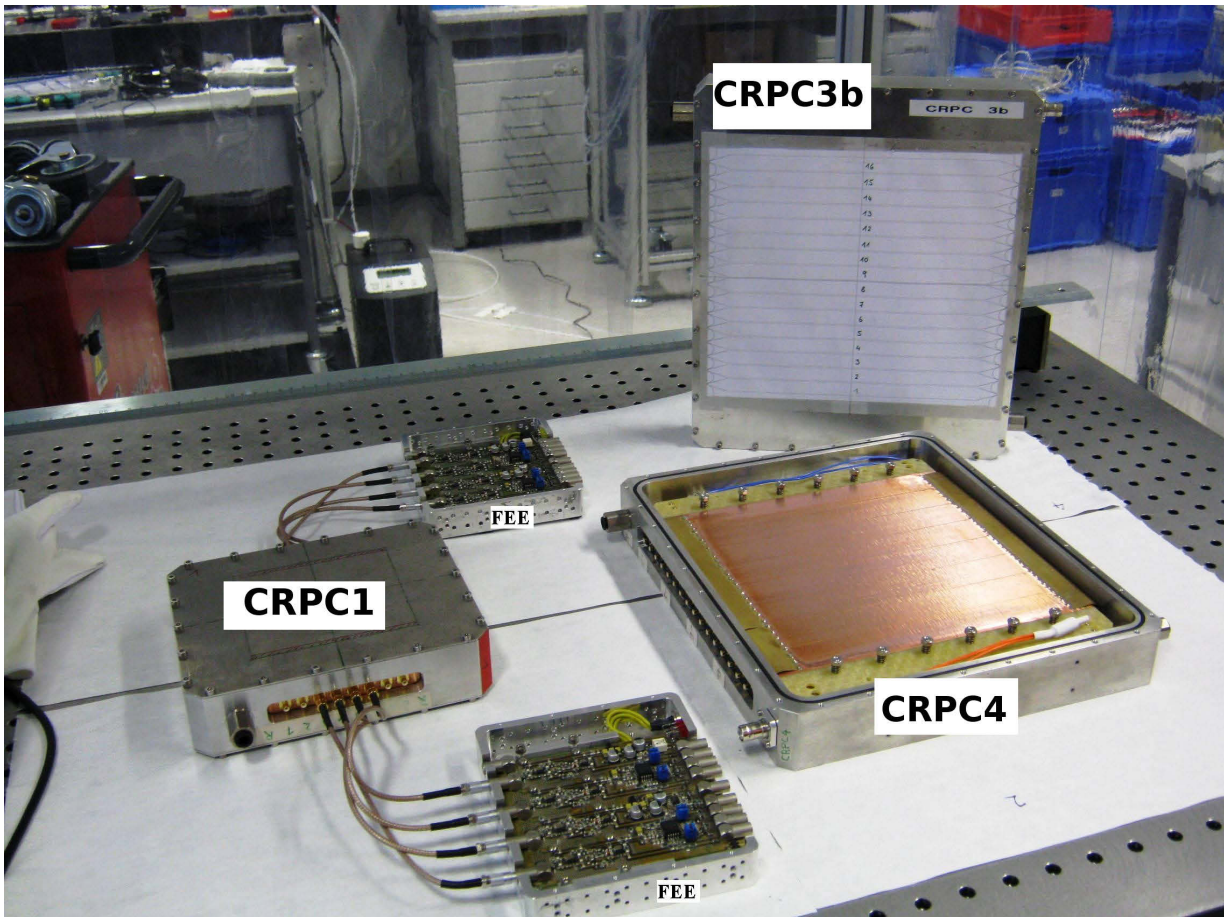


Figure 4.1.: The HZDR prototype CRPC1 with an active area of  $10 \times 10 \text{ cm}^2$  connected to FEE electronics. Standing on the right is the  $20 \times 20 \text{ cm}^2$  prototype CRPC3b. CRPC4 is opened for visual inspection with dimensions of  $20 \times 20 \text{ cm}^2$ .

The basic concept of RPCs is very simple. As described in Section 2.1, it consists of two plates arranged parallel with respect to each other with a separator in between, with gas flowing through the gap, subjected to a high voltage. With the passing of time, there have been notorious improvements on RPCs architecture while leaving this concept mainly unchanged. The development of timing-RPCs showed that, while the time resolution improved greatly in sub-millimetre structures, the efficiency and charge collection suffers. Therefore, the multi-gap RPC was developed. To cover wider areas in large-scale detectors the multi-strip architecture was created. Lately, to diminish the noise and increase charge

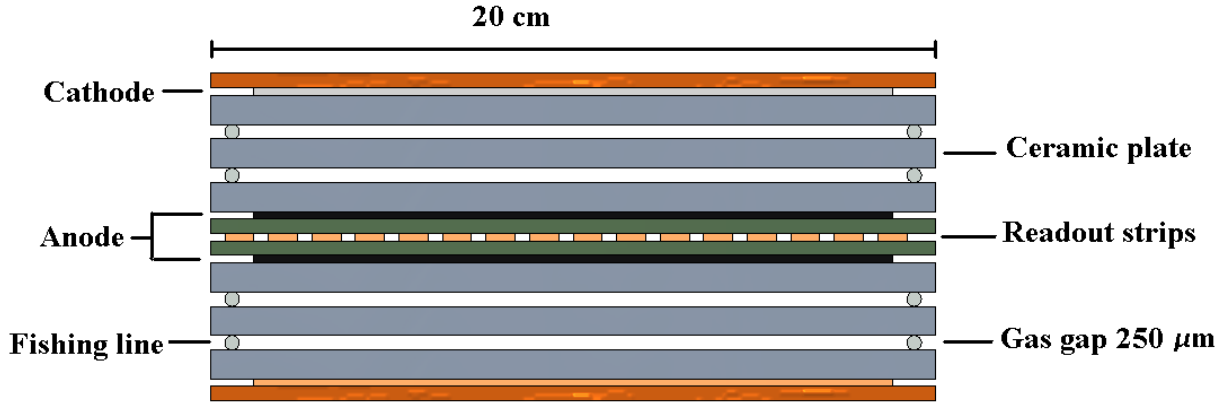


Figure 4.2.: Scheme of a 20×20 cm<sup>2</sup> RPC as realised in prototype CRPC3b.

collection, new differential front end electronics have been developed which allowed to modify the RPC structure to read out signals from anode and cathode.

In this high-rate ceramic RPC research several prototypes with different concepts were build, tested and their performance evaluated. In this chapter, these prototypes are described in detail. Also their intrinsic properties and special characteristics are summarized and compared with each other. The fringe electric fields at the edge of the plates are discussed. The techniques used to minimize them will also be shown.

## 4.1. Dual two gap RPC with Si<sub>3</sub>N<sub>4</sub>/SiC ceramic electrodes

The main detector concept for RPCs with Si<sub>3</sub>N<sub>4</sub>/SiC ceramic electrodes is that of a dual two-gap RPC. This concept makes use of the multi-gap architecture while mirroring the structure around the central pick-up strips to increase charge collection. A multi-gap structure means that there are several gas gaps between anode and cathode “in series”. The mirrored architecture around the central pick-up strips is known as “dual two gap” or “2x2 gap”. Two gaps are located on both sides of the read-out strips conforming a mirror image around them. A scheme of these structure is shown in Figure 4.2.

The voltage is supplied around the outer electrodes. The in-between electrodes are not connected directly to the cathode and anode due to the high-resistive separator (mylar:  $\rho \sim 10^{15} \Omega \text{ cm}$ , nylon:  $\rho \sim 10^{14} \Omega \text{ cm}$ ). Therefore the middle plates are left with an undefined potential a priori. The value of this potential is dynamically adjusted when the external high voltage is established. The final value depends on the gap size and on the external applied voltage. The negative high voltage is supplied to the cathode and the positive one to the anode. Neglecting the voltage drop generated inside the ceramic plates, the ones closer to the cathode will acquire a potential equal to the one established by the

| Detector name | active area [ $\text{cm}^2$ ] | number of gaps | gap size [ $\mu\text{m}$ ] | gap separator | strips |
|---------------|-------------------------------|----------------|----------------------------|---------------|--------|
| CRPC1         | $10 \times 10$                | $2 \times 2$   | 300                        | mylar         | 8      |
| CRPC2b        | $10 \times 10$                | $2 \times 2$   | 300                        | mylar         | 8      |
| CRPC3b        | $20 \times 20$                | $2 \times 2$   | 250                        | fishing line  | 16     |
| CRPC4         | $20 \times 20$                | $2 \times 2$   | 300                        | mylar         | 16     |
| CRPC6         | $20 \times 20$                | 6              | 250                        | mylar         | 32     |

Table 4.1.: Parameters of HZDR RPC prototypes with  $\text{Si}_3\text{N}_4/\text{SiC}$  electrodes investigated with electron beams at ELBE. CRPCs 1 to 4 are dual to gap structures mirrored around the central anode. CRPC6 is a single stack of six gaps between anode and cathode.

high voltage supply. The middle plates will automatically be set to half of the external one if the gas gap widths are the same. This way, the electric field in the gaps will point towards the cathode. The electrons in the avalanche drifting in the electric field will flow towards the anode and their signal will be picked up by the read-out strips. A numerical example would be applying 5 kV to the external electrodes with two gaps of 250  $\mu\text{m}$  width each. The middle one will then be set to a potential of 2.5 kV, thus both gas gaps will have an electric field of 100 kV/cm. Furthermore, since the two stacks are electrically in parallel with respect to the power supply, due to Kirchhoff's laws, the maximum voltage supplied to this structure is half of what is needed to apply to a single stack of four gaps.

A particle crossing the detector ionizes the gas in the gaps in both halves of the RPC. The avalanches on both sides will induce a signal on the read-out strips. The signal travels along the strip and is then read by the amplifying electronics connected to the detector. If the impedance of the strip does not match the input impedance of the electronics, part of the signal will be transmitted to the electronics and part will be reflected back. This reflected signal can reach the opposite side of the strip and then be transmitted to the corresponding electronic channel. These signals, corresponding to reflections, will be recorded by the data acquisition system (DAQ) and must be separated from the signal with the timing correlated to the arrival time of the incoming particle. In larger detectors the length of the strip is tens of centimetres. A typical signal traversing the strip has a velocity of 13 cm/ns in HZDR CRPCs [42]. The signal travelling a length of 20 cm will require a minimum time of 3 ns if the initial signal is generated in the edge of the detector. Then the reflected signal timing arrives 3 ns later than the real hit. For central hits, this time is even higher. A usual signal time distribution has a width of  $\sigma \approx 100$  ps, which corresponds to  $\text{FWHM} \approx 235.5$  ps. Thus the real arrival time signal and the reflected signal can be easily separated.

The input impedance of the amplifying electronics and the strips was matched at 50  $\Omega$ .

This structure has been used in several HZDR prototype detectors, with different active areas and gas gaps. Characteristics of these detectors are listed in Table 4.1.

### 4.1.1. Two-gap RPC with $\text{Al}_2\text{O}_3$ ceramic electrodes

The advantages and disadvantages of using  $\text{Si}_3\text{N}_4/\text{SiC}$  ceramic electrodes have already been discussed in Chapter 3. Another approach to the use of ceramic materials for high-rate RPCs has been proposed by Akindinov et al. [76], who propose a new type of hybrid RPC with characteristics of parallel plate counter and resistive plate chamber. In this detector, for each gap, one of the electrodes consists of a fine layer of conducting material (SiC or Al) deposited on a high resistive material (glass or  $\text{Al}_2\text{O}_3$ ), the other is the usual high-resistive material. Testing these prototypes in-beam, time resolutions better than 90 ps for kaons and pions and efficiency higher than 90% have been achieved.

Prototypes made of  $\text{Al}_2\text{O}_3$  ceramics and  $\text{Si}_3\text{N}_4/\text{SiC}$  composites were assembled and tested with 30 MeV electrons. The details of the detector assembling and special remarks regarding the architecture and gas considerations are discussed in the following.

### 4.1.2. The Rogowski profile

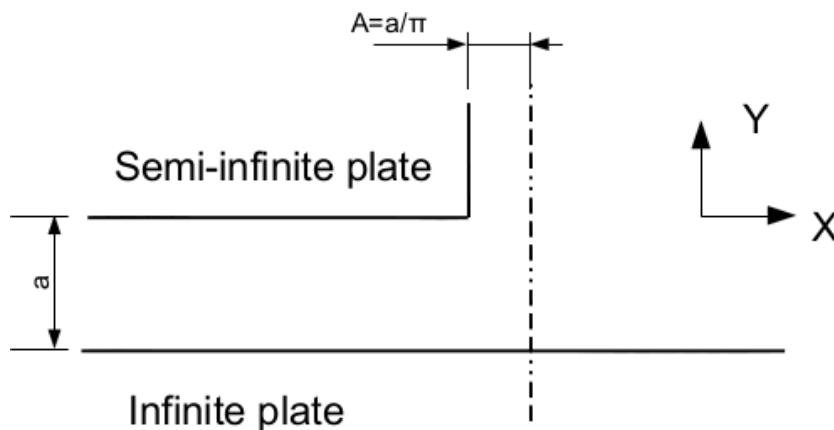


Figure 4.3.: Geometry used to calculate the fringe fields at the edge of a parallel plate capacitor.

The fringe fields created at the edges of a parallel plate configuration can be much higher than the electric field in the centre. This problem was studied by Rogowski in the 1920s [77]. Let us consider a parallel plate capacitor with a semi-infinite plate and a infinite plate separated a distance  $a$ , like the one displayed in Figure 4.3. An expression for the potential can be calculated by using image charges over the infinite plane. Considering that the semi-infinite plate has a potential  $V$  and that the infinite plate is set to a null potential, one finds a solution to to Maxwell's equations

$$x = A[\varphi + e^\varphi \cos\psi] \quad (4.1)$$

$$y = A[\psi + e^\varphi \sin\psi] \quad (4.2)$$

where  $A = a/\pi$ ,  $\psi = v/V\pi$  with  $v$  the potential at any point in space and  $\varphi$  a geometrical parameter. The electric field for this geometry is calculated in [77]. The case for which  $\psi = \pi/2$  can be simplified to



$$x = A\varphi \quad (4.3)$$

$$y = A \left( \frac{\pi}{2} + e^\varphi \right) \quad (4.4)$$

If the shape has  $\psi < 0.4 \times \pi$ , the electric field strength will be lower at the edges than at the centre region. Therefore, the breakdown of the gas mixture at the edge can be avoided. Thus a rounded shape of the edge of the electrode following this equations is optimal to reduce the electric fields at the edges of an RPC.

### Detector scheme for ITEP RPCs

Four different prototypes were assembled and tested. Two of them were two gap RPCs where  $\text{Al}_2\text{O}_3$  electrodes were placed at the outer part of the gas gaps and a  $\text{Si}_3\text{N}_4/\text{SiC}$  ceramic electrode was placed in the middle as a floating electrode. The other two detectors were three stacks of these two-gap “sandwiches” forming two six-gap RPCs.

The material was described in Section 3.4. The electrodes have dimensions  $5 \times 5 \times 0.2 \text{ cm}^3$ . However, the Chromium is deposited in a smaller area of  $4.85 \times 4.85 \text{ cm}^2$ . The metallic properties of Chromium make it useful as terminal for establishing the high voltage in the detector. They are also intended to collect the signal generated by the avalanches and direct it towards the amplifying electronics. Many detectors can then be used to cover a larger surface with a granularity of  $4.85 \times 4.85 \text{ cm}^2$ .

The electric field at the edge of the electrodes is reduced thanks to a special shape carved into the plates. This shaped is inspired by the above Rogowski solution to the parallel plane capacitor, although it does not follow exactly the profile described by him. The shape is attained by carving a groove on the surface of the  $\text{Al}_2\text{O}_3$  plate. Then the chromium is evaporated up to the middle point of the groove. Thus, the electric field is uniform in most of the part of the plates and decreases slowly in the grooved region. The plate is separated into two regions, as depicted in the left panel of Figure 4.4. The edges are part of the  $\text{Al}_2\text{O}_3$  ceramic, where no high voltage is applied. The rest of the plate is one single chromium electrode.

A  $4.85 \times 4.85 \text{ cm}^2$  area is located in the middle of the plate were the chromium was deposited through evaporation, and a high resistive area is on the edge where no high voltage was applied. The groove is approximately  $200 \mu\text{m}$  deep and the chromium evaporated layer reaches to about the middle of the groove (cf. Figure 4.4 right panel). The Chromium layer is used as voltage electrode and signal pick-up electrode. It is read out at a corner and the signal routed out of the detector.

The detectors with this special electrodes were developed at ITEP. There were built from stacks of two-gap RPCs where the readout was combined. These RPCs were fully ceramic, the electrodes were made of low resistive ceramics while the spacers were made by high resistive ceramics. The gas gaps were  $250 \mu\text{m}$  wide. A stack of three two-gap RPCs is depicted in the left panel of figure 4.5. The ceramic spacers used are shown in the right panel.

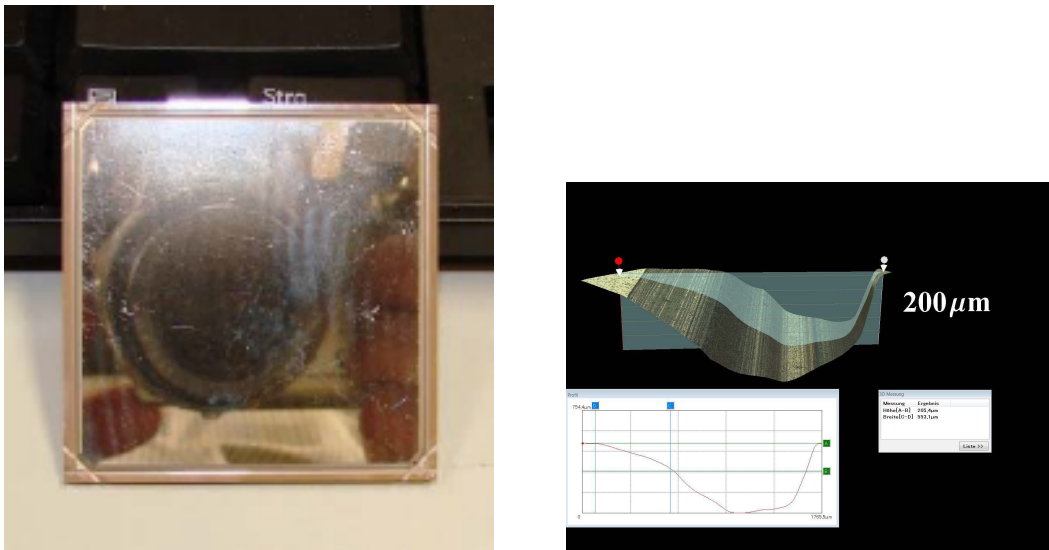


Figure 4.4.: Left panel: a picture of the deposited chromium over an  $\text{Al}_2\text{O}_3$  ceramic plate. Right panel: microscope measurement of the groove.

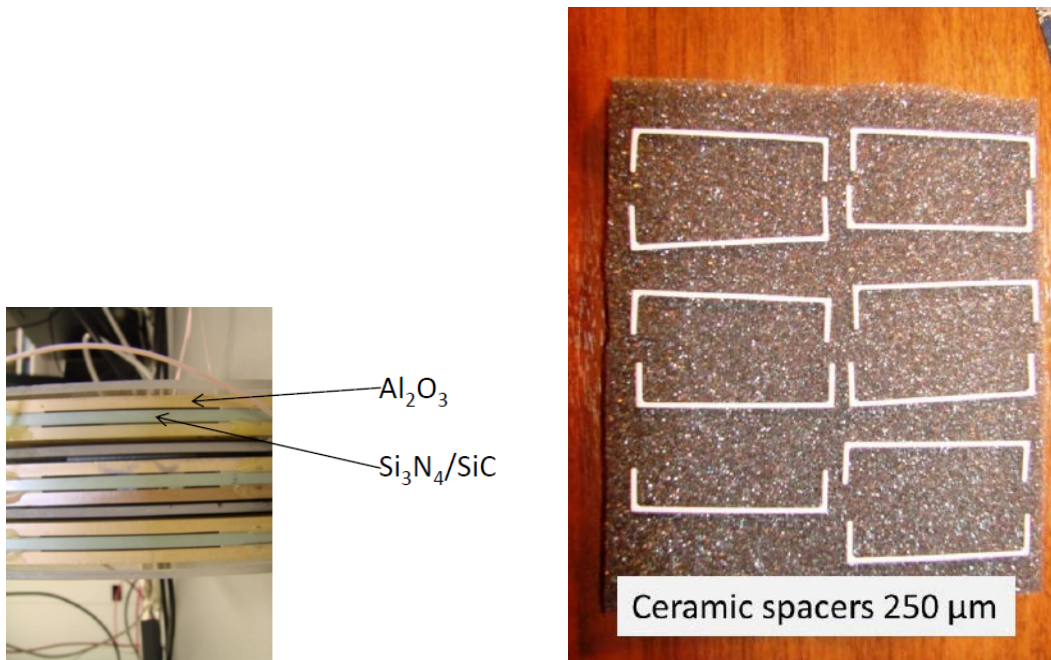


Figure 4.5.: Left panel: a stack of three sandwiches of RPCs. In total six gaps are read out simultaneously. Right panel: high resistive ceramic spacers used in ITEP prototypes.

### Detector scheme for HZDR RPCs

One of the uncertainties about operating timing RPCs at high rates is the gas flow in the gaps. Usually, the RPC stack is placed inside a container box with large empty areas

| Detector name | active area [ $\text{cm}^2$ ] | gas gap size [ $\mu\text{m}$ ] | gas gap separator | number of gaps |
|---------------|-------------------------------|--------------------------------|-------------------|----------------|
| HZDR          | $4.85 \times 4.85$            | 300                            | kapton foil       | 2              |
| Itep1         | $4.85 \times 4.85$            | 300                            | kapton foil       | 2              |
| Itep2         | $4.85 \times 4.85$            | 250                            | ceramic           | 6              |
| Itep3         | $4.85 \times 4.85$            | 250                            | ceramic           | 6              |

Table 4.2.: Parameters for four different  $\text{Al}_2\text{O}_3$  ceramic RPC prototypes.

surrounding it. The gas flows through the detector by diffusion. However, in a micro-gap structure the rate of renewal of the gas might not be enough at higher particle fluxes, thus deteriorating the RPC performance. To test these effects, one of the two-gap RPCs was placed inside a specially designed box where there were no empty spaces around the active area. The gaps were implemented in such a way that the gas flows from the gas input line directly through the gaps and into the gas output line. A scheme of this special construction is shown in Figure 4.6. There, the gas input and output is marked in orange, the  $\text{Al}_2\text{O}_3$  electrodes in granite, the  $\text{Si}_3\text{N}_4/\text{SiC}$  ceramic electrode in blue and the readout connector in red. The plates were separated by a  $300 \mu\text{m}$  thick Kapton foil.

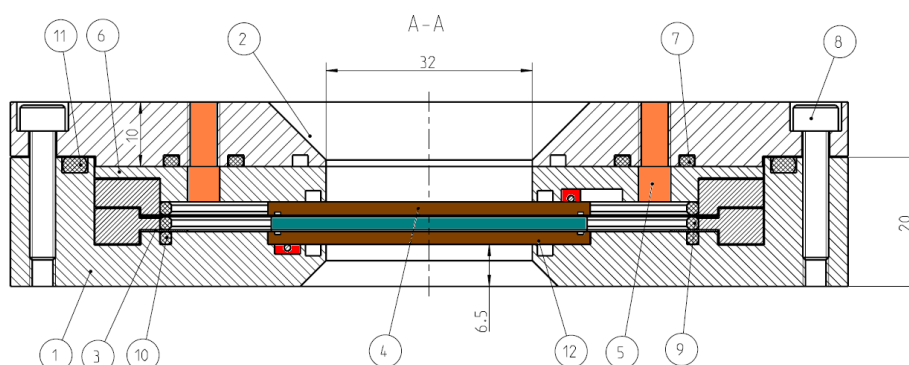


Figure 4.6.: Engineer design of a two-gap RPC with Rogowski-shaped electrodes. The orange parts are the gas input and output. The small red boxes are the voltage connectors. Brown-coloured electrodes correspond to Rogowski-shaped electrodes while the blue correspond to a  $\text{Si}_3\text{N}_4/\text{SiC}$  electrode.

As a summary, in Table 4.2 the parameters of these RPCs are shown.

### Gas effects on low resistive electrodes

The first tests with this new prototypes indicated that the goal of lowering dark current was achieved. However, the working point voltage could not be reached. At the higher electric fields in the gaps, the current suddenly increased to several tens of microamp and remained there while a certain noise could be heard inside the detector. Upon opening

the RPCs, the surfaces of the electrodes were inspected under a microscope. It was found that there were organic depositions formed in the metallic surface of the cathode. This depositions grew in the shape of filaments or whiskers towards the anode. Thus in those points the electric field increased drastically favouring the apparition of sparks inside the gas gap. This provides and explanation for the increased dark current observed during the tests. In Figure 4.7 a 3D reconstruction made by the microscope is shown. The height of the whisker amounts to  $100\ \mu\text{m}$ . The growth of such filaments is associated to the i-butane component of the gas mixture. Similar effects have previously been observed by the JADE group in drift chambers [78].

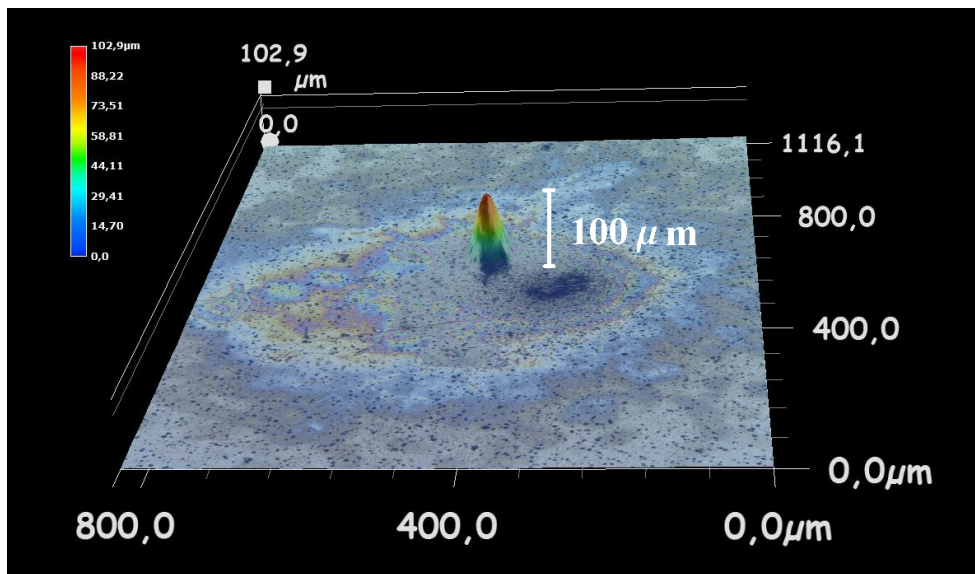


Figure 4.7.: 3-D reconstruction of a whisker over a chromium layer.

This whisker could be cleaned with the use of acetone, indicating its organic nature. Due to the increased field created by the filament, the surrounding region was filled by sparks which cause visible damage around the chromium metallic plate. This damage can be seen in Figure 4.8. The  $\text{Si}_3\text{N}_4/\text{SiC}$  ceramic plate was undamaged, however. After observing this effect, the gas mixture for operating this detectors was changed to 90%  $\text{C}_2\text{H}_2\text{F}_4/10\%$   $\text{SF}_6$ .

Another test was performed in which the RPC operated with pure freon for two days. The absence of quencher implied that the RPC operated in streamer mode for that time. The discharges were so large that large areas of the Chromium layer were destroyed. In contrast, the corresponding region on the  $\text{SiC}/\text{Si}_3\text{N}_4$  electrode was simply blackened but not damaged. This indicates that the discharges grew so much that temperatures of hundreds of degrees were reached in some points. Also some whiskers grew inside the gaps making a contact between anode and cathode. The current at 100 V jumped from 0.0 nA with Freon to  $140\ \mu\text{A}$ . A I-V measurement showed that indeed there was a short-cut inside the detector. When calculating the resistance associated to such currents one obtains a value in the order of  $\text{M}\Omega$  which is in the same order of magnitude as the one obtained with a dedicated set-up.

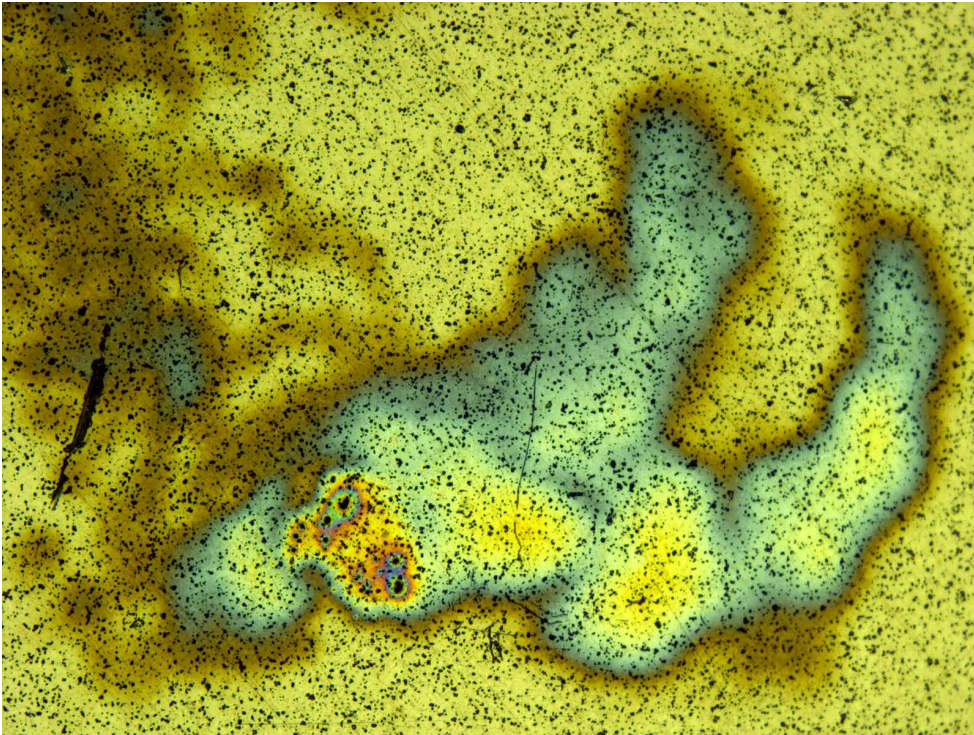


Figure 4.8.: Photo of a burned region and acid trace around the burning point on a Chromium layer. The dimensions are around  $3.15 \times 2.35$  mm.

Two microscope images of the plates after this study are shown. Figure 4.9 shows the chromium destruction after the discharges (left panel). The black region corresponds to a large hole of approximately  $200 \mu\text{m}$  at its maximum diameter. The right panel shows “paths” where the discharges were more intense. These paths connected several holes.

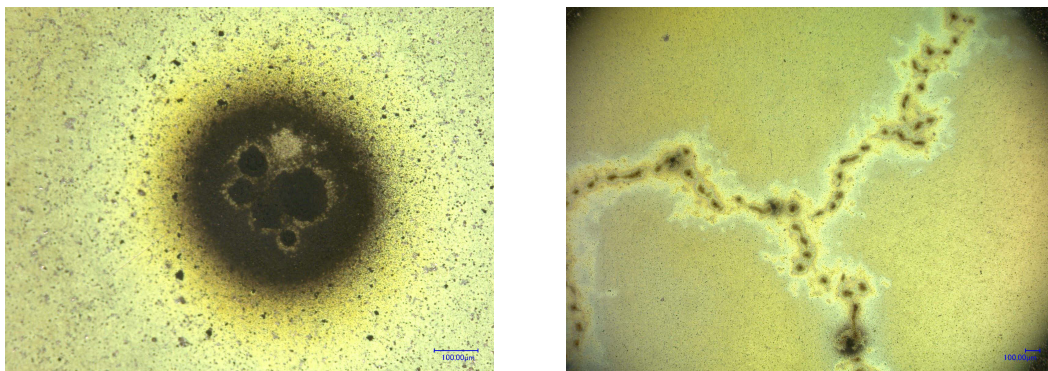


Figure 4.9.: The size of the pictures is  $0.8 \times 1.1$  mm approximately. Left panel: a burned region after being exposed to constant streamers during two days. Right panel: a “path” joining such burned spots.

### 4.1.3. Differential readout prototypes

In a differential readout the charge is collected at both the anode and the cathode. The signals are then fed into a differential amplifier. The benefit of this method is a partial noise cancellation due to the properties of differential amplifiers and an increase of charge collected thanks to the read out of both anode and cathode. Based on the experience acquired by previous prototypes, the differential RPC was designed as a six-gap RPC with  $250\ \mu\text{m}$  gap width. The width of the strips was decreased as well as the inter-strip distance. The active surface of this detector is  $20\times 20\ \text{cm}^2$ . The average bulk resistivity is in the order of  $10^{10}\ \Omega\ \text{cm}$ .

The edges of the electrodes were rounded by a milling machine. The radius of the edge is 1 mm. The goal is to reduce the edge discharges and minimize the dark current. These edges were also studied in a microscope. The left panel of Figure 4.10 is a microscope image of the edge of the plate. The profile of the edge was measured with the microscope. The results is shown in the right panel of Figure 4.10.

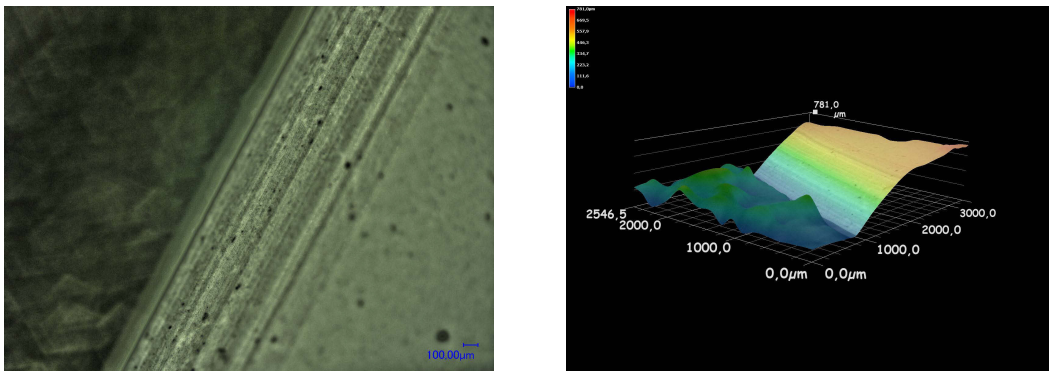


Figure 4.10.: Left panel: Microscope image of a rounded edge on a ceramic plate. Right panel: 3-D reconstruction by the microscope of the upper half of the round edge.

## 4.2. Gas mixtures for ceramic RPCs

Two different mixtures were used in the investigation:  $85\% \text{C}_2\text{H}_2\text{F}_4/10\% \text{SF}_6/5\% \text{i-C}_4\text{H}_{10}$  (called “standard“ from now on) and  $90\% \text{C}_2\text{H}_2\text{F}_4/10\% \text{SF}_6$ . In these mixtures,  $\text{C}_2\text{H}_2\text{F}_4$ , also known as freon, acts as counting gas and quencher;  $\text{i-C}_4\text{H}_{10}$  captures high energy photons generated by de-excitation of molecules in the mixture and  $\text{SF}_6$  captures low energy electrons, preventing the formation of secondary avalanches parallel to the main one and cathode-directed streamers. There have been many studies of the gas mixture impact on RPC performance. For example, studies of flammable-gas-free mixtures were done in [45], or with and without  $\text{SF}_6$  in [46].

### 4.3. Dark current comparison

In a parallel plate configuration the electric field is homogeneous in the central parts of the detector. However, at the edges of the plates, fringe fields appear. These fields are orders of magnitude higher than the ones in the centre of the plate. Due to the high voltage applied, these fields can get high enough as to enter into the dielectric breakdown region of the gas. This implies the development of discharges around the edges of the detector which contribute to the dark current and dark rate.

Three edge types of ceramic plates have been studied. The first one is a simple  $90^\circ$  angle between the horizontal and vertical faces of the plate. A second one uses an intermediate face between the vertical and horizontal ones decreasing the angle to  $45^\circ$ . The third one is a round edge with a 1 mm radius. Figure 4.11 is a representation of these different configurations. The high voltage is applied to the outer electrodes made of copper. The resistive electrodes are  $\text{Si}_3\text{N}_4/\text{SiC}$  ceramics with parameters described in Chapter 3. The gas is normal air at standard temperature and pressure. Since the problem to be addressed is just a electrostatic problem, the choice of gas is irrelevant. The electric field is evaluated at the edge of the plates following the dashed line showed in Figure 4.11.

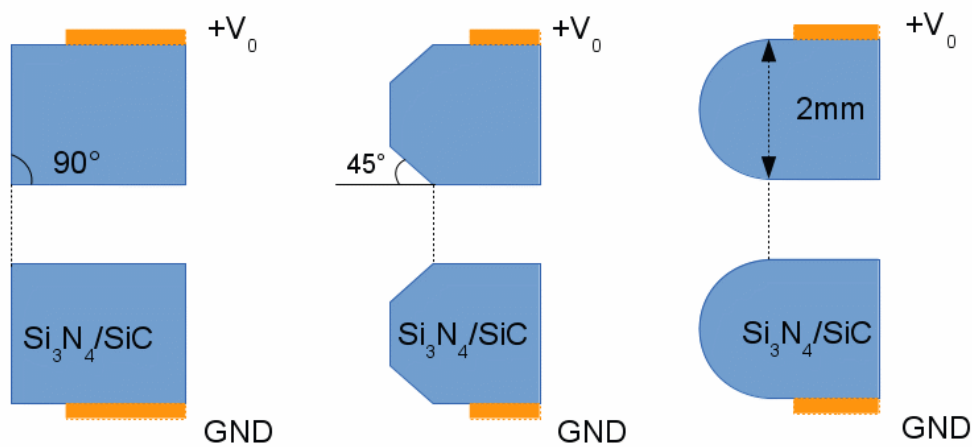


Figure 4.11.: A depiction of the structures used for the simulation of the edge fields of semiconducting ceramics electrodes.

The results of the simulation can be seen in Figure 4.12. The  $90^\circ$  edge is the worst configuration possible. The field at the edge is two orders of magnitude higher than the one for the other two configurations. There is small difference between the  $45^\circ$  angle and

the rounded edge. Both have negligible edge effects. However, for even smaller gaps, the rounded edge would be the recommended structure, since the fringe fields will increase with the proximity of the plates to each other.

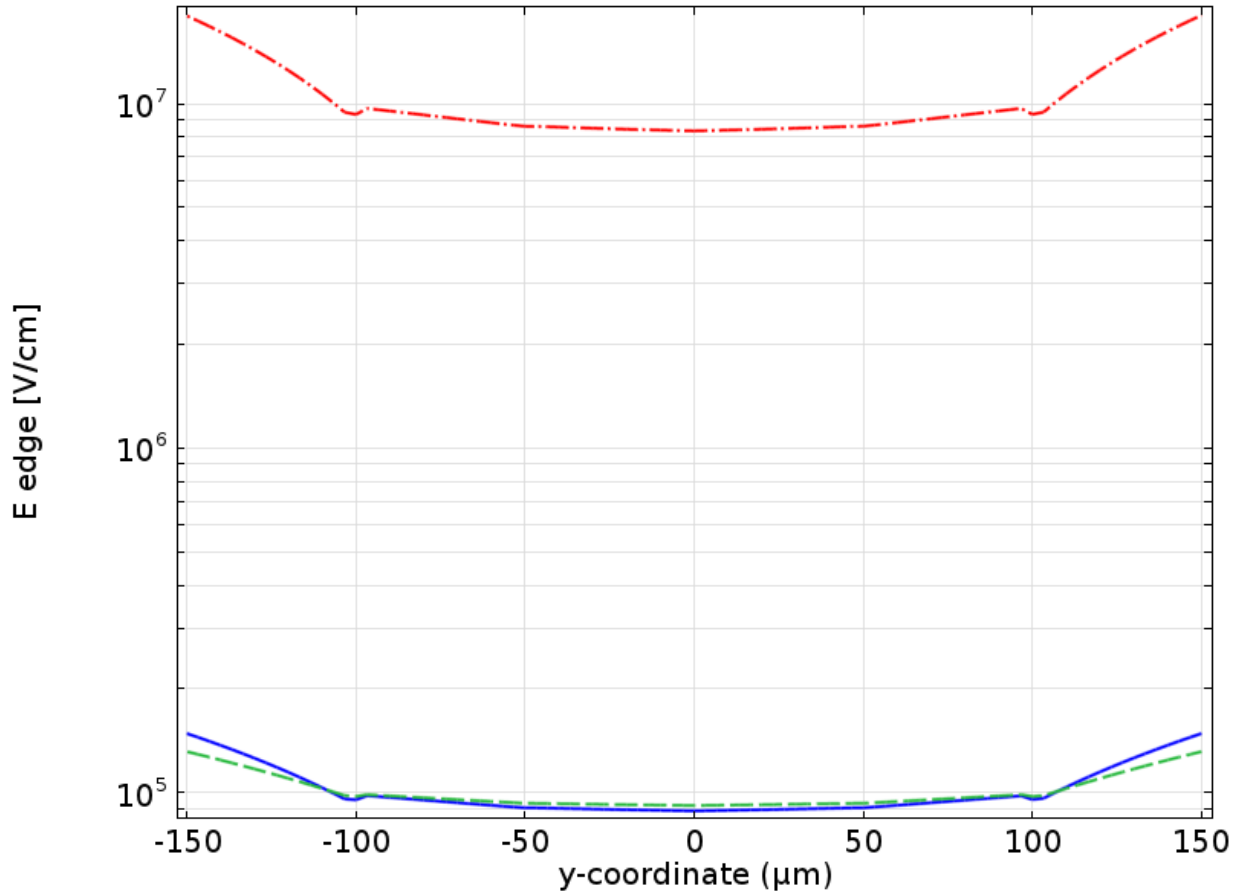


Figure 4.12.: Results of a simulation of fringe fields for three edge types. The red curve is for a  $90^\circ$  edge (4.11, left panel), blue a  $45^\circ$  edge (4.11, centre panel) and green a rounded edge with 1 mm radius (4.11, right panel).

The dark current was measured for some of these configurations. The  $90^\circ$  edge was not implemented in the plates for obvious reasons. However, for the small RPCs the edge is not completely at  $45^\circ$  degrees. So a higher field value than the one for  $45^\circ$  is expected. The result is shown in Figure 4.13. The closed circles (●) and squares (■) points are measurements of dark current of  $10 \times 10 \text{ cm}^2$  detectors with 4 gaps and  $300 \mu\text{m}$  per gap. The upper triangles (▲) were taken from a  $20 \times 20 \text{ cm}^2$  detectors with 4 gaps and  $250 \mu\text{m}$  per gap. Finally the lower triangles (▼) correspond to dark current measurements of a 6 gap RPC with  $250 \mu\text{m}$  per gap and  $20 \times 20 \text{ cm}^2$  active area. the lines joining the points are linear interpolations and are used to guide the eye. The electric field shown is the one calculated from the power supply and not the fringe field. However, one can observe how the triangle curves, corresponding to  $45^\circ$ -type edge and rounded edge, present a similar dark current, with the rounded edge creating a slightly smaller current. The results for



the small RPC give a much higher current, attributed not only to the edge, but also to a lower bulk resistivity in the plates and different spacer types.

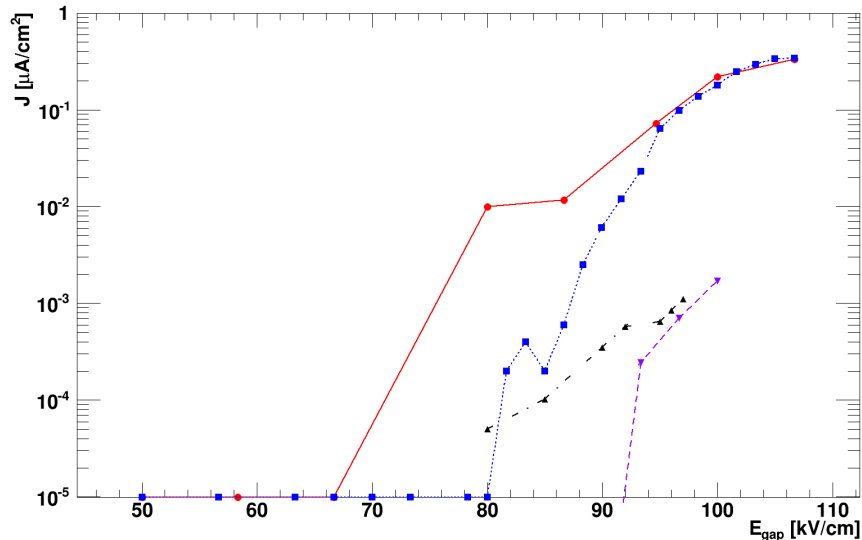


Figure 4.13.: Measurement of the dark current density as a function of the electric field comparison for three different edge types. The closed circles (●) and the closed squares (■) correspond to a 90° edge type. The upper triangles (▲) correspond to a 45° type edge and the lower triangles (▼) to a round edge with a 1 mm radius.

## 4.4. Front End Electronics

The low charge contained in the induced signal requires the use of amplification electronics to be able to work with said signal. The input signals delivered by an RPC are typically fast signals, with a rise time lower than one nanosecond, an amplitude of few millivolt and a charge of few tens to hundreds femtocoulombs. Two different amplifiers were used for the single ended prototypes and one amplifier was used in the differential readout configuration.

### 4.4.1. FOPI amplifying electronics

One of the types of amplifiers used were the Front End Electronics (FEE) developed for the FOPI Time-of-Flight wall [79]. These amplifiers present a 3-stage amplifier followed by a leading-edge comparator. For each input channel, a digitized timing signal and an analogue signal are provided. Each FEE card has four inputs. Each card also has a test-input for testing purposes and a logical OR output. The FEE have a large bandwidth of 1 GHz. The amplification can be tuned up to 200. The thresholds can be adjusted

to discriminate signals of few millivolt. These amplifiers are optimized for an input and output impedance of  $50\ \Omega$ .

The amplification and time jitter of these electronics were studied. The amplification is set globally for the whole card by a single potentiometer. However it was measured that the amplification varies from channel to channel and from card to card drastically (see Appendix B).

#### 4.4.2. PADI - Preamplifier and discriminator

The PreAmplifier and Discriminator (PADI) was designed as a general purpose electronics [80]. It was developed in the frame of the CBM ToF wall research on RPCs. As opposed to the FEE detailed in previous sections, PADI delivers a differential input and output. Therefore, signals from both anode and cathode can be read and amplified, thus gaining a factor two in the signal charge contents.

The PADI have a  $50\ \Omega$  impedance, an amplification gain of approximately 100 and a bandwidth larger than 300 MHz. Several families of the PADI architecture have been developed. The differential CRPC prototype was equipped with PADI-VI amplifiers placed in a motherboard. Each motherboard has 8 chips of 4 channels each, allowing for the coverage of 32 electronic channels. The motherboard has an output for each of the input channels, and OR signal for each of the chips and a DAC interface to modify the thresholds of the discriminators.

## 5. In-beam Tests of CRPCs

Cosmic radiation is one of the main sources of radiation for detector testing. It has many advantages: it is always available, provides a very distinct signal in the detector and doesn't require complex set-ups to work with. The main disadvantage is its low rate. The average flux at sea level is  $1 \text{ cm}^{-2} \text{ min}^{-1}$  [81]. Thus, tests require long periods of time to accumulate enough statistics to provide meaningful results. Despite this, they are widely used for measuring basic RPC parameters and for calibration purposes. This is the case for trigger RPCs like the ones at ATLAS [9], ALICE [11] or CMS [10] (all of them at CERN). Also, experiments with a time-of-flight wall built with RPCs, like HADES [82] at GSI or ALICE [61], have used cosmic rays for their performance studies.

The cosmic radiation has been used only for calibration procedures during ceramic RPC research. The prototypes have been systematically tested in radiation beams. The experiments were performed in electron beams at the electron linac ELBE at HZDR [83], in proton beams at the Cooler Synchrotron (COSY) at FZ Jülich [84], and under heavy ion reaction products at SIS-18 at GSI [85]. A triggered system was used in all these tests.

A description of the set-ups used in these experiments is given in this chapter. A discussion of the beam and trigger conditions and a comparison of the different environments is also presented. The calculation of the fluxes for non-uniform beam profiles is discussed.

### 5.1. Basic concepts of trigger systems

The structure of a trigger system is as follows. One or more detectors, whose performance is known, are used as trigger detectors. The device under test is placed between them. Any particle that crosses the trigger also crosses the prototype if its trajectory is a straight line.

When a particle crosses the set-up, the trigger detectors provide one signal respectively. The overlap of these signals acts as a trigger. This trigger provides a time window in which to look for the signals of the device under test. Any signal of this device which coincides with the trigger is recorded. Thus, in the case of a hit, a triple coincidence is produced between the trigger detectors and the device under test.

The absolute efficiency of the detector under test can be estimated. After  $N$  incoming particles, the counts recorded by the detector will be  $N_{detector} = \varepsilon_1 \varepsilon_2 \varepsilon_{detector} N$ , where  $\varepsilon_{1,2}$  and  $\varepsilon_{detector}$  are the efficiencies of the trigger detectors and the device under test, respectively. The counts recorded by the trigger coincidence will be  $N_{trigger} = \varepsilon_1 \varepsilon_2 N$ . Then the efficiency is determined by

$$\varepsilon_{detector} = \frac{N_{detector}}{N_{trigger}}. \quad (5.1)$$

To calculate the efficiency uncertainty, it is necessary to know the uncertainty in the counts recorded by the detector. Assuming that the efficiency follows a binomial distribution, it is possible to calculate this by:

$$\sigma_{\varepsilon_{detector}} = \sqrt{\frac{\varepsilon_{detector}(1 - \varepsilon_{detector})}{N_{trigger}}}. \quad (5.2)$$

Random coincidences in the detector chain can be important in high-rate environments. This effect can be analysed as follows. Assume that the trigger detectors provide each a signal with the same widths  $\tau_1$  and  $\tau_2$ . The trigger is a pulse defined by the overlap of these signals with a width  $\tau_1 + \tau_2$ . The trigger detectors record each certain rates,  $R_{1,2}$ , in units of inverse of time. The random coincidences are then

$$N_{random} = R_1 R_2 (\tau_1 + \tau_2). \quad (5.3)$$

Thus, the timing coincidence window should be as small as possible to minimize the random coincidences. There are some limitations as to how small this window can be. The detector type and the signals it provides is one of the main factors. The coincidence window cannot be smaller than the sum of the width of the detector signals or real coincidences are lost. This, together with signal pile-up in the trigger detectors, provides an upper limit for the incoming particle fluxes which can be triggered on under stable conditions.

## 5.2. Test in electron beams

The performance studies were carried out by exposing the RPC prototypes to 30 MeV electrons at the Electron Linac with high Brilliance and low Emittance (ELBE) at HZDR.

ELBE is the first accelerator in the world to use a superconducting RF gun operating in full continuous wave (CW) mode. The beam energy can reach up to 40 MeV. The accelerator produces several kinds of secondary radiation from the primary electron beam: coherent electromagnetic radiation in two free-electron-lasers, bremsstrahlung photons, direct electrons, neutrons and positrons. These secondary radiation beams are used in different experimental areas inside the ELBE hall. Figure 5.1 shows a layout of the facility. The RPC tests were carried out in the Radiation Physics Cave indicated by a red circle.

### 5.2.1. Accelerator details

A thorough determination of the beam characteristic was done during the RPC development. The purpose is to understand the unique properties of the electron beam provided by ELBE and its effects on RPC prototype testing. While ELBE can accelerate electrons up to 40 MeV, in the tests typical values of 30 MeV were attained. At this energy, electrons behave as minimum ionizing particles. However, there exists a low angle scattering due to the interaction of electrons with the material in the set-up.

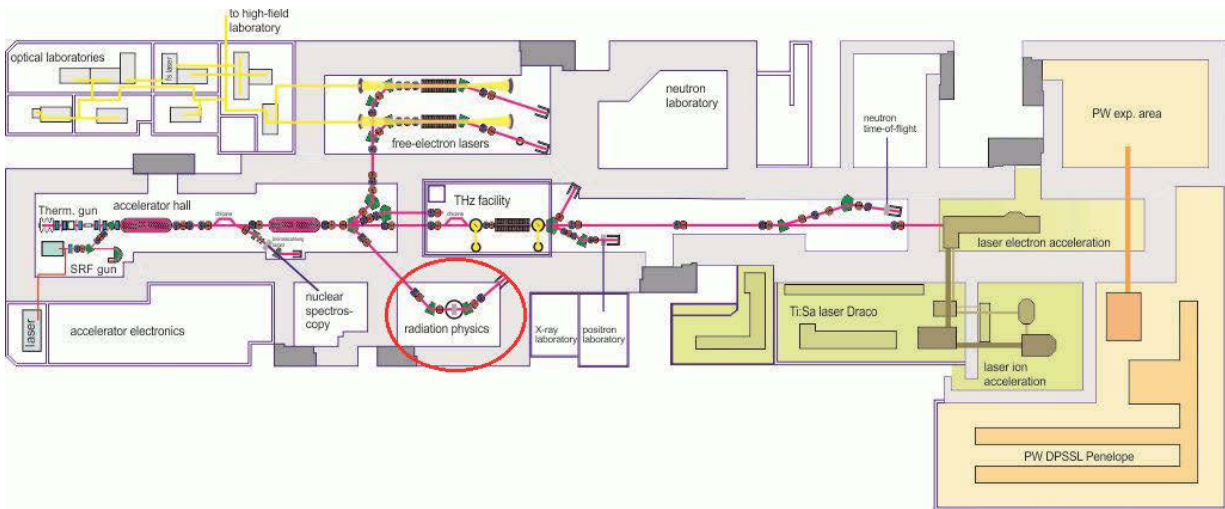


Figure 5.1.: Layout of the ELBE facility at HZDR. Status at January 2014.

### Single-electron mode

One of the important features of the electron beam at ELBE is the so-called “single-electron-mode”. This mode, developed at HZDR, is unique to the ELBE facility [86]. It allows for the delivery of a single electron in a micro-bunch. That is, with a very high probability it is possible to guarantee that there will be one or none electrons in every bunch, but no more. This special characteristic makes the ELBE beam especially well suited for testing particle detectors. This effect is achieved by placing scattering screens in the beam trajectory. Scattered electrons will be discarded and will not reach the experimental set-up. Only those electrons that do not scatter will exit the beam-pipe and reach the RPC measurement set-up. This effectively “dilutes” the beam. The number of bunches which are filled with a electron depends on the electron gun injector voltage. The incoming particle rate is tuned by modifying the electron gun voltage thanks to this effect. The total rate is in a range from  $100 \text{ s}^{-1}$  up to  $10^6 \text{ s}^{-1}$ . A scan of the rates used during a beam time is shown in Figure 5.2.

### Repetition Frequency Precision

The repetition frequency signal is an extremely well defined signal provided by the accelerator radio frequency (RF) system. The RF signal marks the time in which a bunch is created. The beam bunch has a duration of less than 5 ps according to the ELBE specifications. The bunch repetition rate, and thus the RF-signal, can be modified as fractions of  $26/2^n \text{ MHz}$  ( $n=0, 1, 2, \dots, 8$ ). In case of RPC testing, it was specified as  $26/4 \text{ MHz}$ .

However, not every RF pulse corresponds to an electron arriving to the RPC in the single electron mode. As an example, consider a RF with a frequency of 6.5 MHz. This corresponds to a period of 154 ns. If the rate arriving to the RPC is  $10^5 \text{ s}^{-1}$ , this means that approximately 15% of the RF impulses correspond to an electron crossing the system.

This signal is used as start time in time-of-flight systems research at ELBE. The main advantage is its high precision. Figure 5.3 shows a histogram of the RF signal with a

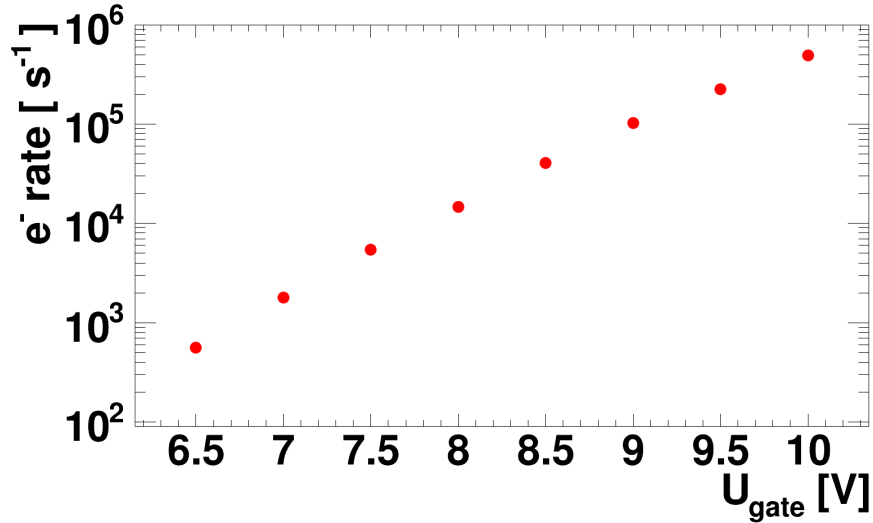


Figure 5.2.: Extracted incoming electron rate as a function of the electron gun voltage.

Gaussian fit. This measurements is done by feeding the same signal to two different channels of the same TDC. The figure shows the difference between the two channels. The time resolution of the signal is defined as the standard deviation of the Gaussian distribution. The resolution amounts to  $\sigma_{RF+TDC} = 38.45 \pm 0.22$  ps. This high precision shows that the signal is suited for start time in fast time-of-flight research, where the detectors under test can have a time resolution of 50 ps [62]. The resolution shown in the figure combines the RF resolution and the TDC resolution. The RF signal is transported by fibre optic cable from the accelerator high frequency system to the measurement room. There it is refreshed and fed into a CAEN v1290N TDC.

### 5.2.2. Test set-up for CRPCs

The set-up used in CRPC studies was as follows. Two scintillating plastic detectors of volume  $2 \times 2 \times 0.5$  cm<sup>3</sup>, each read-out at both sides, are placed before and after the RPC defining the trigger region. The RPC is placed in a movable platform between the two plastics. The platform can be moved in the vertical and horizontal direction with a precision better than 1 mm. Two more plastic scintillating detectors are placed in front of the set-up to determine the incoming particle rate. The size of these detectors was  $4 \times 4 \times 0.1$  cm<sup>3</sup>. Depending on the size of the RPC to be tested, smaller scintillating plastics are used to better define the particle trajectories. Two scintillating plastics of dimensions  $0.5 \times 0.5 \times 0.1$  cm<sup>3</sup> and two of  $0.5 \times 1 \times 0.1$  cm<sup>3</sup> were used for this purpose. They were not used in the trigger logic, but cuts on their timing signals helped define the valid hits (see Chapter 6). A scintillating plastic of  $4 \times 4$  cm<sup>2</sup> was used when necessary. This set-up is presented in Figure 5.4. A list of all the scintillating detectors is compiled in Table 5.1.

The trigger was defined as the coincidence between the signals of the four photomultiplier tubes S1, S2, S3, S4 and the repetition frequency (RF) of the accelerator. The trigger region is larger than the scintillator area due to small angle scattering of the electrons in

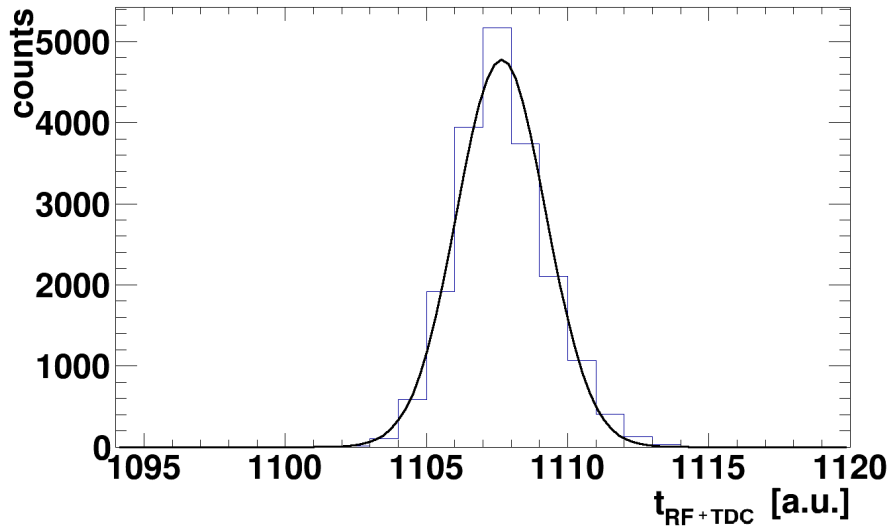


Figure 5.3.: The time distribution of the repetition frequency,  $t_{RF+TDC}$ , of the accelerator. The continuous line is a Gaussian fit to the experimental data. The standard deviation corresponds to a start time resolution of  $\sigma_{RF+TDC} = 38.45$  ps.

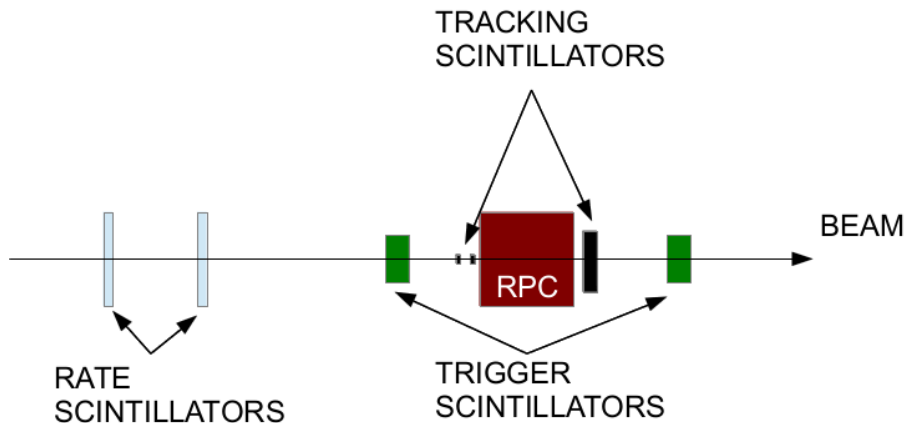


Figure 5.4.: Experimental set-up for RPC testing with electron beams.

the material. The RPC signals are read out by front-end amplifiers, part of the FOPI experiment time-of-flight detector development. The front-end provide a digital timing signal and an analogue signal for each electronic channel. Each strip in the RPC is read out at both sides, each side accounting for a electronic channel. The timing signal is transported to the measuring room through 20 meter long cables. There, it is fed into a leading edge discriminator to refresh it and finally recorded by a CAEN TDC v1290N, time-to-digital converter, based on the HPTDC chip developed at CERN, with a precision of 24.4140625 ps/bin [87]. The analogue signal is amplified by a factor of ten in the measuring container by a CAEN N979 fast amplifier and digitized by a CAEN QDC v965

| Scintillator | Dimensions [cm <sup>3</sup> ] | Purpose      |
|--------------|-------------------------------|--------------|
| S1&S2        | 2 × 2 × 0.5                   | trigger      |
| S3&S4        | 2 × 2 × 0.5                   | trigger      |
| S5           | 0.5(diameter) × 1             | beam profile |
| S6           | 4 × 4 × 1                     | tracking     |
| S11          | 0.5 × 0.5 × 0.1               | tracking     |
| S12          | 0.5 × 0.5 × 0.1               | tracking     |
| S13          | 0.5 × 0.5 × 0.1               | tracking     |
| S14          | 0.5 × 0.5 × 0.1               | tracking     |
| S23          | 20 × 20 × 2                   | rate         |
| S24          | 4 × 4 × 1                     | rate         |
| S25          | 4 × 4 × 1                     | rate         |

Table 5.1.: List of the scintillating sizes and purposes for detectors used in the RPC test system.

charge-to-digital converter with a precision of 25 fC/bin. The front end amplifier provides additionally an OR signal which was used for online efficiency estimation purposes.

The data acquisition system was based in the Multi Branch System (MBS), developed at GSI [88]. The online monitoring was based on the GSI Online-Offline Analysis Tool (Go4), also developed at GSI.

### 5.2.3. Electron Beam profile

The electron beam profile was determined in each experiment. There are different ways to do this, depending on the equipment available. A measurement of the beam profile is needed to estimate the particle fluxes to which the RPCs are exposed. Four different methods are used to do this:

#### Emulsion Plate

Emulsion reactive plates were exposed to the electron beam at different places in the set-up. This enables the study of the variation of the beam shape due to the scattering of the electrons in the material. The exposed plates were revealed in a dark room with specific equipment and the image was digitized and stored in a computer. Figure 5.5 is a sample of the photoplate images collected during the experiments. The upper left panel corresponds to a emulsion plate placed at the outside of the beam pipe during July 2011. The apparent image of the beam being “cut” is due to scattering screens not completely removed from the beam trajectory. The upper right panel is the image of another plate exposed at the same position during November 2011. The beam fully covers the beam-pipe. The lower centre panel shows the image recorded by a emulsion plate pasted to the outside of the aluminium RPC box. The plate was exposed during July 2011. The shadows of the scintillators can be seen and have been marked to better distinguish them. The beam has lost the focalized structure present in the upper left panel due to scattering on the scintillators.



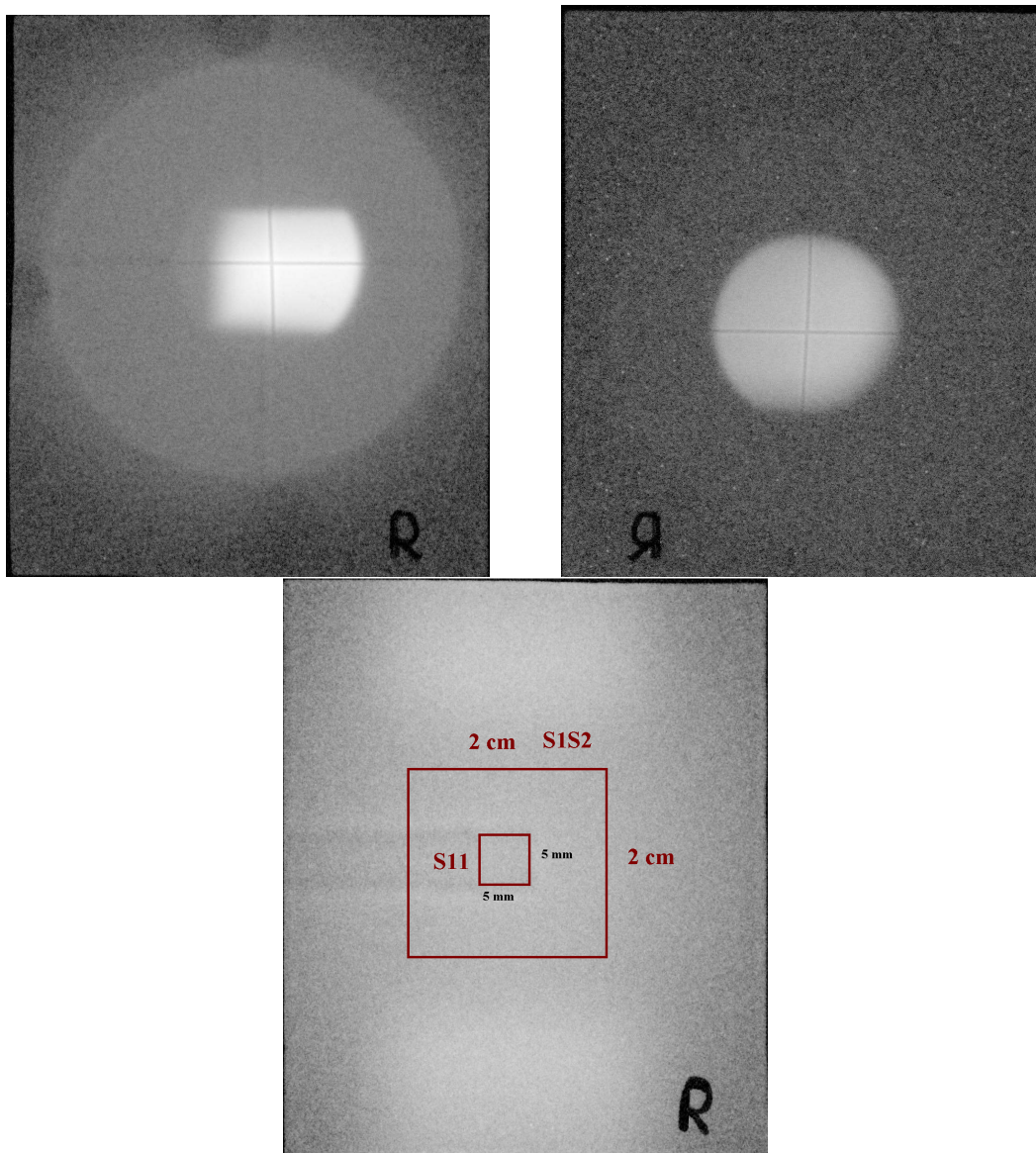


Figure 5.5.: Emulsion plates exposed to the electron beam during two experiments. Upper left panel corresponds to a plate placed at the exit of the beam pipe during June 2011. Upper right panel shows the image of a plate at the same position during November 2011. Lower centre correspond to a plate pasted to the frontal face of the RPC aluminium box during June 2011.

### Scintillator measurement

A coincidence between the signals of two PMTs, S1 and S2, and the small cylindrical scintillator S5 provide a trigger for the determination of the beam profile. While S1 and S2 remain fixed in their position, a scan was made by moving S5 in the horizontal and vertical positions. These profiles are shown in Figure 5.6. The projection of the beam over the RPC plane is an ellipse. The axes of this ellipse can be extracted from Gaussian fits.

| rate [s <sup>-1</sup> ] | $\sigma_x$ [cm] | $\sigma_y$ [cm] |
|-------------------------|-----------------|-----------------|
| 10 <sup>4</sup>         | 1.097 ± 0.005   | 1.246 ± 0.006   |
| 10 <sup>6</sup>         | 1.196 ± 0.005   | 1.192 ± 0.005   |

Table 5.2.: Beam dimensions measured with a fiber hodoscope for two different beam rates. Taken during May 2013.

One obtains  $\sigma_{x,scint} = 1.168 \pm 0.011$  cm and  $\sigma_{y,scint} = 1.557 \pm 0.072$  cm.

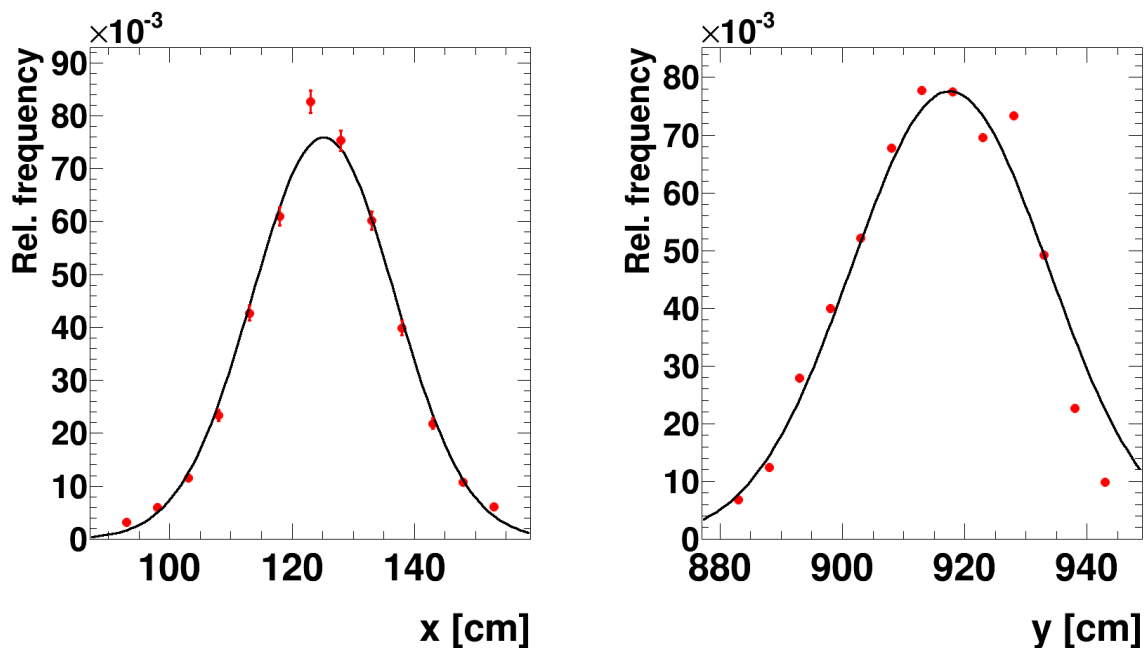


Figure 5.6.: Profiles obtained by scintillator measurement. Left panel: horizontal direction. Right panel: vertical direction. Taken during April 2011

### Hodoscope measurement

A very precise measurement of the beam profile was done with a segmented fiber hodoscope. Three layers of scintillating fibers were oriented in horizontal and vertical directions. The signal generated in the fibers were read by a segmented photomultiplier in both directions. The position precision of this detector is 1 mm. The dependence of the beam spot on the particle flux was determined by measuring the beam spot for two different fluxes. The results are shown in Figure 5.7. The upper panel corresponds to a beam rate of 10<sup>3</sup> s<sup>-1</sup> and the lower panel to a beam rate of 10<sup>6</sup> s<sup>-1</sup>. Table 5.2 summarizes the results obtained with this method. The values for the dimensions are the standard deviation of a 2-D Gaussian fit to the data. No change in the beam size happens when modifying the beam rate, thus providing a constant beam spot during a whole experiment.

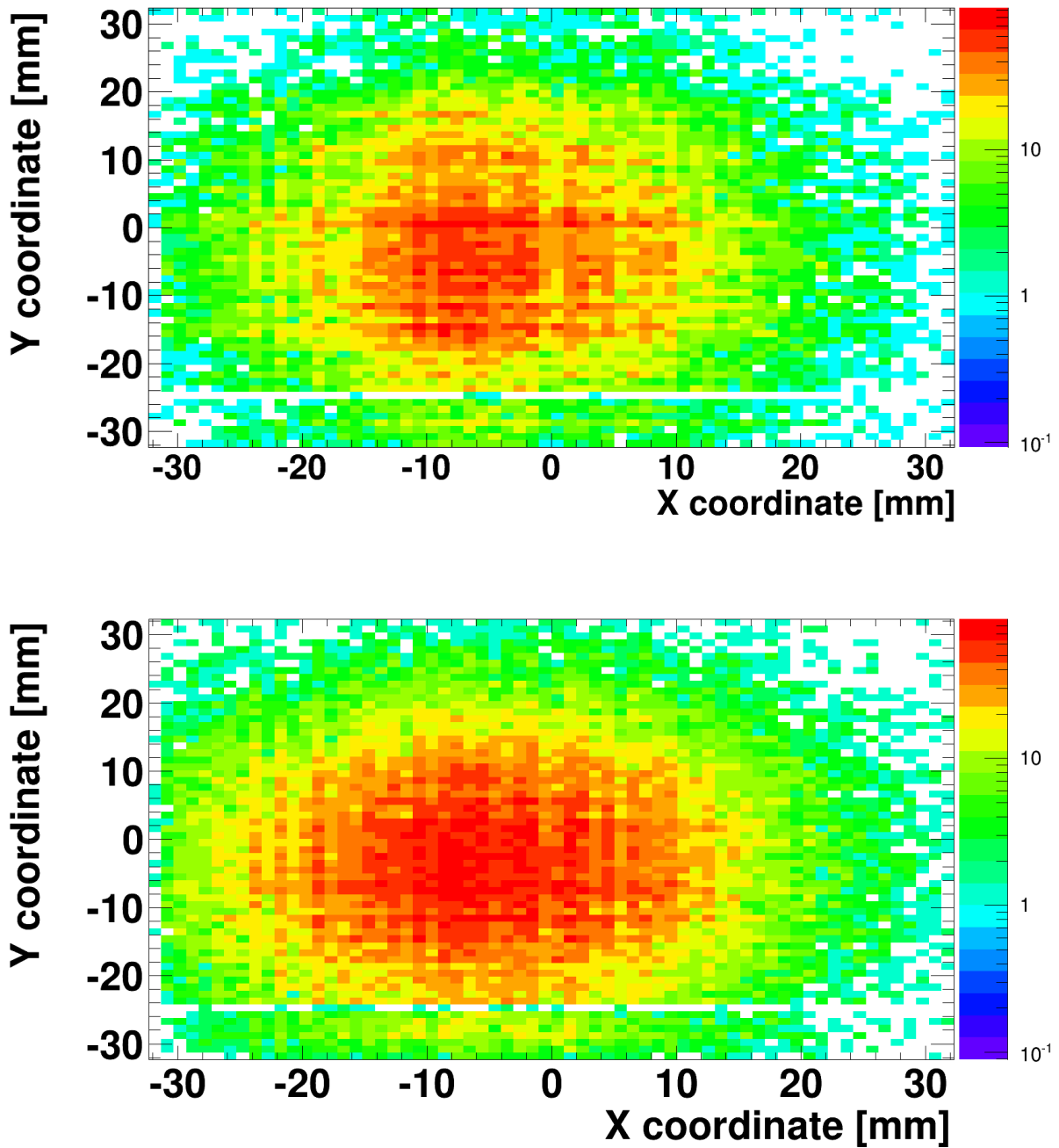


Figure 5.7.: Beam spot measured with a fiber hodoscope. The upper panel shows the beam distribution for an incoming particle rate of  $10^3 \text{ s}^{-1}$  and the lower one for an incoming particle rate of  $10^6 \text{ s}^{-1}$ .

### RPC-extracted beam profile

It is also possible to extract a profile information from the data obtained from the RPC (cf. Figure 5.8). Thanks to the readout of the strips at both ends it is possible to relate

the time difference of the left and right sides of the strips with the spatial location of the signal along the strip. The position information is given by

$$\Delta x = x_L - x_R = \frac{v_{strip}}{2}(t_R - t_L), \sigma_x = \frac{v_{strip}}{2}\sigma_t, \quad (5.4)$$

where  $v_{strip}$  is the speed with which the signal propagates along the strip and  $t$  is the time recorded in the TDC. In this case,  $v_{strip} \sim 13$  cm/ns [42].

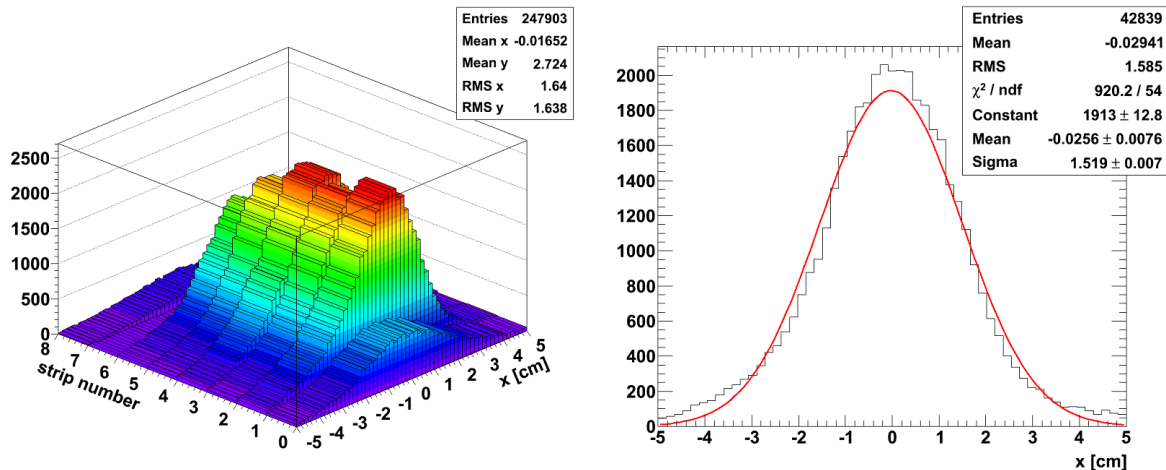


Figure 5.8.: Beam cross section obtained from RPC spectra. Left: spatial distribution for all strips. Right: horizontal projection of the centre most strip. Taken during April 2011.

The RPC spatial information is directly obtained from the time difference. In the vertical direction, the spatial resolution is the strip width, which is 1 cm. This information is always accessible and can be used in every test even if no other methods of measuring the beam spot are available. The information in the vertical direction has a drawback. Usually, more than one strip fires simultaneously when a particle crosses the detector. Thus the vertical dimensions obtained are typically larger than the physical dimensions of the beam.

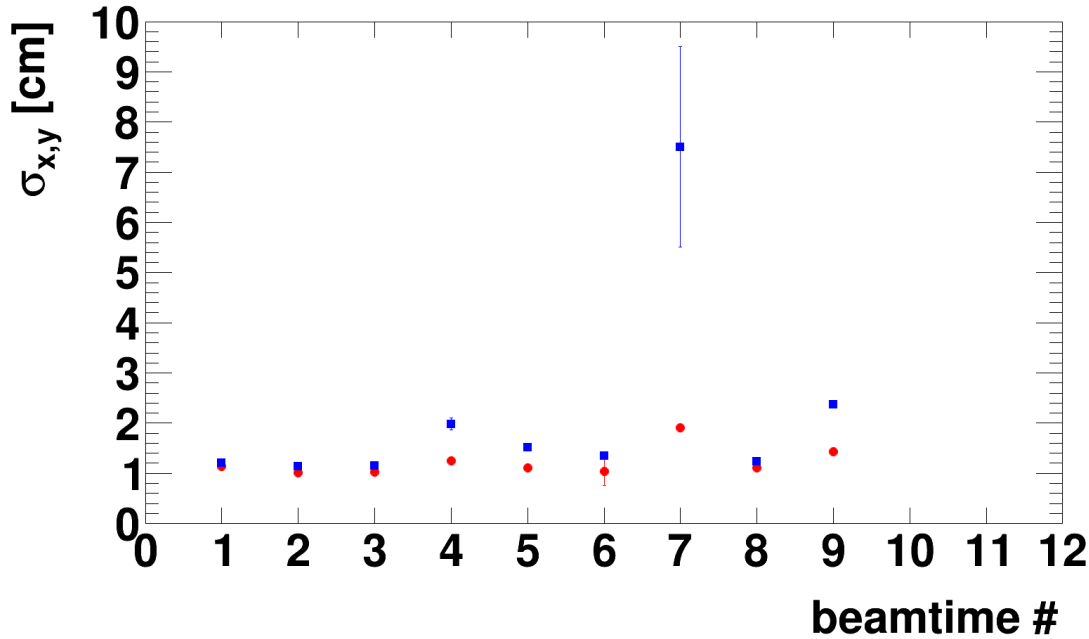
Figure 5.8 shows the reconstruction of the beam spot with the RPC information. On the left, a 2-D reconstruction is shown. On the right, the most irradiated strip information is shown and fitted to a Gaussian distribution. This beam spot data was taken during the same beamtime as the one shown in Figure 5.6, thus a direct comparison is possible. Table 5.3 shows a comparison of the results. The RPC extracted profile has larger dimensions than the one extracted from the scintillator data. This is due to the RPC intrinsic spatial resolution (in the order of 1 cm, see Chapter 6), simultaneous strip firing and scattering on the detector material before reaching the gas gap.

#### 5.2.4. Systematics on the beam profile

The RPCs were systematically tested at ELBE for three years. Valuable information was gathered about the ELBE beam conditions and beam quality. The main parameters monitored are the dimensions of the beam.

| Method       | $\sigma_x$ [cm] | $\sigma_y$ [cm] |
|--------------|-----------------|-----------------|
| Scintillator | 1.168           | 1.557           |
| RPC          | 1.640           | 1.638           |

Table 5.3.: Comparison of the beam dimensions measured with scintillators and RPC.

Figure 5.9.: Beam dimension measured with scintillators for different tests runs from September 2010 until November 2013. The bullets ( $\bullet$ ) correspond to the horizontal dimension,  $\sigma_x$  and the squares ( $\blacksquare$ ) to the vertical,  $\sigma_y$ .

The spatial dimensions of the beam measured with scintillators are shown in Figure 5.9. Except for one beam time where the vertical dimension increased dramatically, the beam size remains constant within a few millimetres. The most probable reason for this anomaly is a scattering screen misplaced in the beampipe. This measurements correspond to 3 years of testing and were gathered in 12 different beam times. This gives a quantitative description of the quality and stability of the single electron mode at ELBE.

### 5.2.5. Average flux estimation

An important remark when studying detectors under local irradiation is the flux of particles which traverses the detector. In the electron beam tests at ELBE, the beam spot was never larger than the RPC and it was never uniform. A clear example of this is shown in Figure 5.8. On the left side the beam profile extracted from RPC position information is presented. This profile was extracted from a  $20 \times 20 \text{ cm}^2$  prototype. In the figure the beam profile decreases to negligible values at 5 cm from the central position in every direction.

This means that the total area irradiated is about  $\sim 25 \text{ cm}^2$  whereas the active area of the detector is  $400 \text{ cm}^2$ .

Therefore, the flux has to be defined for the area under study. In the case of RPCs the beam spot is selected as the region in the range of full-width-half-maximum (FWHM). However the intersection of a plane with the Gaussian describes ellipses, thus the area is taken as an ellipse with its major and minor axis equal to half of the FWHM in the vertical and horizontal directions. The defined area is then

$$S_{beam} = \pi \frac{FWHM_x}{2} \frac{FWHM_y}{2}. \quad (5.5)$$

The flux is defined as the rate in the first PMTs, S24 and S25, divided by the area of the beam spot multiplied by a factor which accounts for the number of events that fall inside a certain range in a Gaussian distribution. In the case of a 2-dimensional Gaussian and for the FWHM region, this factor amounts to 0.56. Thus the flux is calculated, in this region, as

$$\langle \phi \rangle = \frac{N_{S24S25}}{S_{beam}} 0.56. \quad (5.6)$$

A more detailed explanation is given in Appendix A.

## 5.3. Tests in proton beams

The RPC response to hadrons was tested at the Cooler Synchrotron at FZ-Jülich in a proton beam. The protons had a momentum of  $1.7 \text{ GeV}/c$ , with a equivalent behaviour to minimum ionizing particles. The beam was characterized by a small beam spot and very high rate. Fluxes on the order of  $10^6 \text{ cm}^{-2} \text{ s}^{-1}$  were attained thanks to the high focusing power of the accelerator.

### 5.3.1. Experimental set-up

The test were performed in the Jessica Cave. The set-up was shared with the other CBM ToF groups. The trigger, reference counter and electronics set-up was shared between the different groups. The gas system was such that the prototypes were placed in series with the ceramic RPCs at the end of the chain.

A geometrical description of the detectors placement is seen in Figure 5.10. Two ceramic RPC prototypes were tested at the same time in each run. The first detector was a  $20 \times 20 \text{ cm}^2$  prototype with the strips along the horizontal direction. The second prototype was one of two  $10 \times 10 \text{ cm}^2$  RPCs with the strip oriented along the vertical direction. These were exchanged once during the experiment. Two small scintillating plastics of dimensions  $10 \times 5 \times 2 \text{ mm}^3$  were placed in front of the RPCs. Each one over one of the strips in the centre of the detector, where the beam was expected. At the front of the whole set-up two plastic scintillating counters, each read out at both sides were mounted with a  $90^\circ$  angle between them. They were used for reference timing and triggering purposes. At the end of the set-up another plastic scintillating detector was mounted for triggering purposes. A fiber hodoscope, also used at ELBE, was used for the estimation of the beam dimensions.

The electronics were the same as with the electron beam tests, with the timing signals digitized by CAEN V1290N TDCs and the charge signals digitized by CAEN V956 QDC modules. The DAQ was common for all the experimental groups based on the GSI Multibranch System. The online monitoring was based on the Go4 framework.

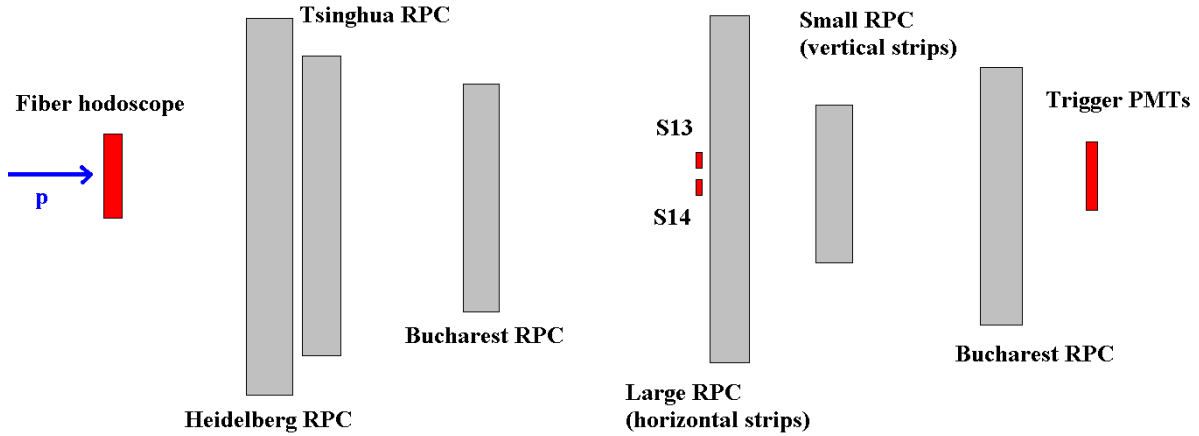


Figure 5.10.: Schema of the experimental set-up during the COSY run.

### 5.3.2. Beam properties

The beam delivered by COSY is a so-called “pencil beam” with a high rate region at the centre with a quickly decreasing rate with the distance from centre and a very small beam divergence. Therefore, to determine the beam dimensions the RMS of the distribution will be the best estimator. The measurement of the beam profile is shown in Figure 5.11. An estimate of the beam spot from the RMS of the measurements gives a value of  $RMS_x = 2.5$  mm and  $RMS_y = 5.8$  mm for the horizontal and vertical dimensions, respectively. The area is calculated by

$$S_{beam} = \pi RMS_x RMS_y = 47mm^2, \quad (5.7)$$

which is a much smaller beam spot in comparison to the one obtained at the electron beam tests. Such a small beam spot is useful for hadron and nuclear physics experiments. However, for detector testing, it carries several inconveniences. The beam will hit the detector at one strip or in the space between two strips. The effects of such a small, concentrated beam on a ceramic RPC will be discussed in chapter 6.

Supposing that the low angle scattering is negligible for this beam energy, the flux at the frontal plane of the RPC can be determined. The particle rates were measured by the frontal scintillators. The rates were recorded by scaler modules and stored into a file. The rates are obtained as the counts on the scaler,  $R$ , divided by the beam spot size,  $\phi = R/S_{beam}$ .

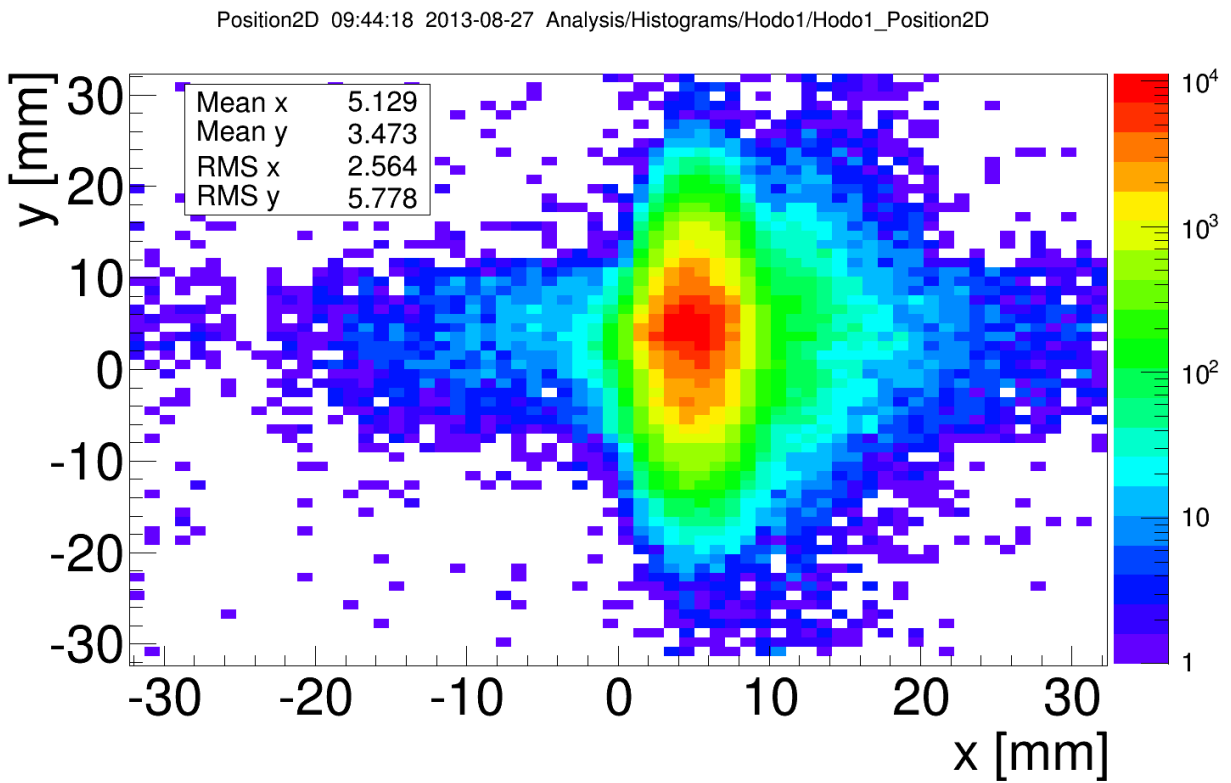


Figure 5.11.: On-line reconstruction of the beam spot for the proton beam at COSY measured with a fibre hodoscope.



## 6. Performance of CRPCs

All the data collected during the tests of CRPC prototypes was analysed. The goal was to obtain the parameters which help define the performance of ceramic RPCs in high-rate environments. Due to the different set-ups employed and the different radiation beams used, special care was taken to ensure that the results from the various beam tests are comparable. Therefore, this chapter starts with the definition of a valid event and explains its relation with the RPC parameters extracted from the analysis. A study of the performance as a function of the electric field in the gas gaps and the incoming particle flux follows. Finally a comparison between the results obtained for the different prototypes under different irradiation conditions is discussed.

### 6.1. Calculating the electric field as a function of the flux

The resistive nature of the electrodes in a RPC implies that the charge released by the avalanche will take a certain time to dissipate over the surface of the electrode. In Chapter 2 it was discussed how this time was directly related to the bulk resistivity and the relative electrical permittivity. The DC model first presented by Carboni et al. in [89] relies on the ohmic voltage drop on the electrode plates due to the current flowing to them. Later on, this model was extended and applied to the RPCs developed for the HADES ToF wall [22, 90].

The voltage drop in the gas gap due to a flux of ionizing particles crossing the detector can be expressed in a general way for a single gap RPC as

$$V_0 - \langle V_{gap} \rangle = \phi q_{total}(\langle V_{gap} \rangle) \rho(\langle V_{gap} \rangle) d, \quad (6.1)$$

with  $V_0$  the voltage applied on the external source,  $\langle V_{gap} \rangle$  the average voltage in the gas gap,  $\phi$  the particle rate,  $q(\langle V_{gap} \rangle)$  the charge released by the avalanche,  $\rho(\langle V_{gap} \rangle)$  the bulk resistivity of the electrode and  $d$  the electrode thickness. Since the prototypes here discussed are multi-gap RPCs, the equation has to be slightly modified. The voltage drop in the whole stack can be represented as two times the voltage drop in one gap, considering the symmetry around the floating electrode. The details are found in [91]. The final expression is

$$\frac{V_0}{2} - \langle V_{gap} \rangle = \frac{3}{2} \phi q_{total}(\langle V_{gap} \rangle) \rho(\langle V_{gap} \rangle) d. \quad (6.2)$$

This equation can be solved analytically for ohmic materials, like glass and bakelite where  $\rho(\langle V_{gap} \rangle)$  is nearly constant. One must also assume that in the saturated region the charge of the avalanche depends linearly on the potential difference in the gas gap.

In the case of semiconducting ceramic electrodes, the bulk resistivity does not obey an ohmic behaviour (see Chapter 3), nor does the charge of the avalanche depend linearly on the voltage in the gas gap. However, the dependence of the bulk resistivity on the voltage was measured in the laboratory. The situation is equivalent to having a potential difference between the two sides of the plates during the operation of the RPC. Therefore it is possible to use eq. (3.3) simply by substituting  $V$  by  $\langle V_{gap} \rangle$ . Therefore eq. (6.1) can be rewritten as

$$\frac{V_0}{2} - \langle V_{gap} \rangle = \frac{3}{2} \phi q_{total}(\langle V_{gap} \rangle) \cdot \frac{\langle V_{gap} \rangle^{1-\kappa}}{I_0} d \quad (6.3)$$

The charge of the avalanche  $q_{total}$  can be extracted from the current information for each flux, or in this case the *rate*  $R$ , after subtracting the dark current  $I_{dark}$

$$\begin{aligned} I &= I_{total} - I_{dark}, \\ \langle q_{total} \rangle &= \frac{I}{2R}. \end{aligned} \quad (6.4)$$

Equation eq. (6.3) is a transcendental equation which can be solved for  $\langle V_{gap} \rangle$  for each experimental point ( $V_0, I, \phi$ ) by means of numerical methods. After solving it, the voltage in the gas gap as a function of the flux is obtained. Therefore, the main variable,  $\langle V_{gap} \rangle$ , which defines most of the parameters of the gas amplification and RPC is parametrized. One example is shown in Figure 6.1. The red points correspond to the voltage drop in the gas gap as a function of rate for electron beams. The blue squares correspond to proton beams. The behaviour of  $\langle V_{gap} \rangle$  is different in both cases. A good parametrization for the proton case is a linear polynomial. However for the electron beam, the fit that best describes the data is of the type  $V_{gap} = V_a \phi^b$ , in the flux range under investigation. It is not possible to extrapolate the behaviour, but this is of no concern here. The goal is to reproduce the data by using the model above for that particular range.

The difference in  $\langle V_{gap} \rangle$  might be an indication of beam spot effects. Due to the smaller beam spot in the proton beam, the ration of the illuminated area against the non-illuminated area is much smaller than with the electron beam. Thus, the electrodes take longer to charge up. This will have an effect on parameters like the efficiency and time resolution. These will be discussed below.

The functional behaviour of the efficiency as a function of  $V_{gap}$  is well described by a Fermi function,

$$\varepsilon = \frac{\varepsilon_0}{1 + e^{\theta(V_{gap} - V_{ref})}}, \quad (6.5)$$

with  $\varepsilon_0$  the efficiency extrapolated to the situation for low fluxes,  $\theta$  a parameter which describes the steepness of the function and  $V_{ref}$  the voltage at which the efficiency is half of  $\varepsilon_0$ .

Knowing the dependence of the parameters on  $V_{gap}$  and the dependence of  $V_{gap}$  on  $V_0, I$  and  $\phi$ , it is possible to do a global fit to the data for different working conditions.

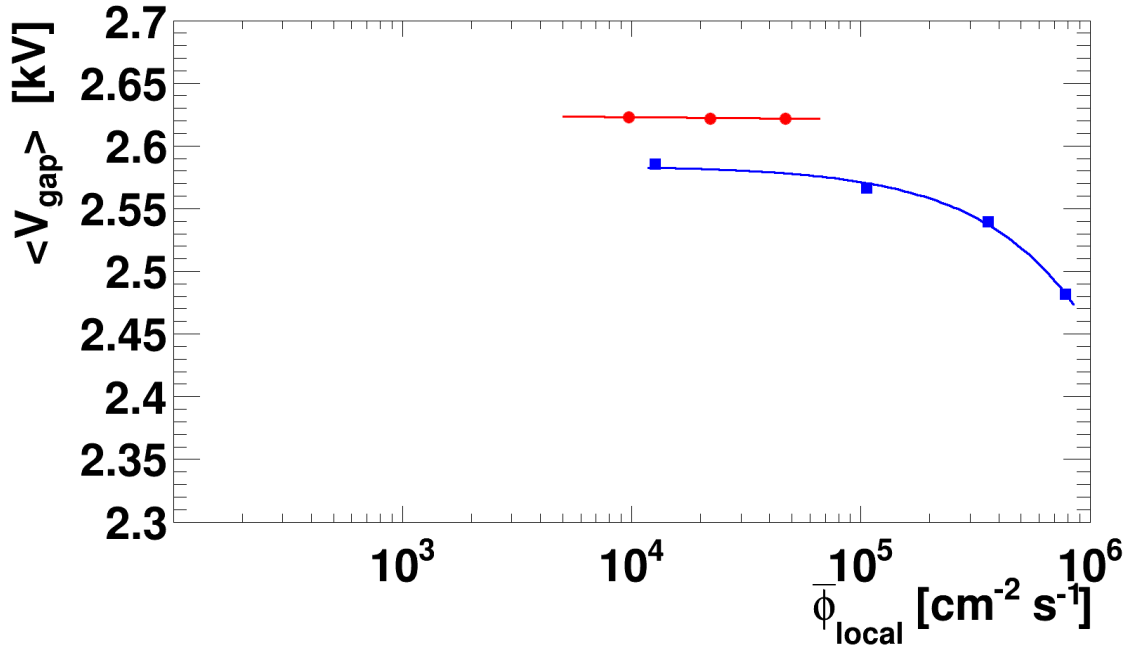


Figure 6.1.: Voltage drop in a single gas gap  $\langle V_{gap} \rangle$  as a function of the local particle flux  $\bar{\phi}_{local}$  for electron irradiation at ELBE ● and proton irradiation at COSY ■. The solid lines are fits to the data.

## 6.2. Definition of parameters and conditions

### 6.2.1. Event definition

It was mentioned in Chapter 5 how a trigger system helps to reduce the background. It was also discussed the probability of random coincidences. There can be some cases in which the trigger signal is delivered to the DAQ but no signal is recorded by the electronic modules in which the scintillating plastic signals are fed into. An event definition based on the timing spectra of the trigger detectors is done. Thus, during off-line analysis, a valid triggered event is defined by the following conditions:

1. A RF hit recorded by the TDC falls into an interval of 2 ns around the main timing peak. This cut is particularly effective in low-rate measurements. At these rates, field emission of electrons from the beam-pipe is produced. These electrons arrive at the set-up but are not correlated with the RF, since they do not come from the RF gun. If they cross the set-up inside the TDC search window, their timing will be recorded, but will not fall strictly on the main peak. Also, secondary frequencies from the accelerator synchronization system may be present, sometimes biasing the main peak width towards higher values.
2. A scintillating plastic timing hit falls into an interval of 2 ns around the main timing peak. Essentially, it provides the same effects as the cut on the RF. However, at high rates, this cut allows for minimization of random coincidences effects, which

can provide false triggers in which the RPC does not record a signal. Also, if the coupling of the secondary frequencies in the RF is too strong, this cut separates the main frequency set by the operator providing a better start time resolution. This was the only method employed in the analysis of the proton beam test data. No RF signal was used during that experiment.

In the case of the RPC, a proper timing hit in an electronic channel is defined by an interval of 2 ns around the main peak. This cut eliminates hits from reflections in the timing spectra. However, it is wide enough as to record the tails of the distribution which sometimes can have a physical significance.

All these conditions ensure that the triggered event has a valid timing in all the trigger detectors. For the RPC, this cuts implies that the efficiency will be defined as the efficiency of the RPC to give valid timing signals. It also helps to discard in a very easy way the reflections due to impedance mismatching or crosstalk in the electronics. During this chapter, the term “valid trigger” will be used for the events that passed the cuts on the trigger detectors explained above. A “valid timing hit” on the RPC will describe events that pass the cuts on the RPC (after passing the cuts on the scintillators).

### 6.2.2. Parameter definition

The general efficiency and time resolution determination was explained in Chapter 5. Here a more refined definition is provided.

The efficiency will be defined as the number of valid timing hits on the RPC divided by the number of valid triggers. Mathematically, this can be expressed as

$$\varepsilon = \frac{N_{RPC,OR}}{N_{trigger}}, \quad (6.6)$$

where  $N_{RPC,OR}$  is the logical OR operation over both sides of all strips and  $N_{trigger}$  is the number of valid triggers. The logical “OR” is chosen to account for the most efficient FEE used in the detector. The FEE amplifiers used, provide different amplification between them and between channels of the same amplifier. If a logical “AND” is used (we ask for a valid timing hit on both sides of the same strip), the efficiency of the detector will be biased due to the poor amplification of some of the electronic channels. A more detailed explanation is given in appendix A.

The time resolution definition depends on the beam spot size. For the electron beam, which typically covers three strips, the time resolution is defined as the average of the time resolution of the three most irradiated consecutive strips. In the case of the proton beam, which hit the detector between strips, it is defined as the average of the two strips irradiated by the beam. This average accounts the for systematic effects introduced by differences in the electronic channels. The time resolution of one strips is defined as

$$\sigma_{strip} = \sigma \left( \frac{t_{left} + t_{right}}{2} \right), \quad (6.7)$$

that is, the standard deviation of a Gaussian fit to the mean timing spectrum. Finally, the time resolution over a certain number of strips  $n$ , depending on the beam spot, is defined

as

$$\sigma_{RPC+FEE} = \sqrt{\sum_{i=1}^n \sigma_i^2 / n^2 - \sigma_{ref}^2}, \quad (6.8)$$

with  $\sigma_{ref}$  the resolution of the reference timing signal.

### 6.2.3. Time-walk correction

It is a well known fact that the arrival time of the avalanche is influenced by noise and a walk introduced by the electronics. To correct for this problem the charge has been measured. Thus a correlation between the arrival time of the signal and the charge is established. The correction of this effect is called *time-walk correction* or *slew correction*. The result of this correction can be seen in Figure 6.2. This kind of correction significantly improves the time resolution of the detectors. The correction depends on the signal rise time and amplifier saturation. Typically an improvement of the time resolution in the order of tens of picoseconds is achieved.

## 6.3. Currents and charges induced by avalanches

The low bulk resistivity of the ceramic material increases the dark current of the detector. As it was shown in Section 4.3, CRPCs deliver a dark current density in the range of  $10^{-3} - 10^{-1} \mu\text{A}/\text{cm}^2$  depending on the edge type. In the case of a Rogowski-shaped electrode, the dark current falls below the precision of the instruments. Figure 6.3 shows the electric current density,  $J$ , versus the average electric field strength in the gas gap,  $\langle E_{gap} \rangle$  for different fluxes. The electric field strength was calculated from the voltage obtained from solving equation eq. (6.3).

The plot shows that the current increases with the electric field strength in the gas gap and with the flux of the incoming particles. Figure 6.4 shows the total charge released by the avalanches. In this case, the charge released decreases with the increase of the incoming particle flux. The straight lines represent a linear fit to the data. However, the solution of eq. (6.3) was done point by point with the experimental values measured. The plot shows that the charge at  $\langle E_{gap} \rangle \approx 98 \text{ kV}/\text{cm}$  varies from 0.6 to 1.4 pC on average depending on the flux. This values can be compared with semi-conductive glass prototypes exposed to the same electron beam during another beam time with the same set-up [62]. The semi-conductive glass showed a total charge of 2.5 pC for low fluxes. However, that detector was operated at a higher electric field strength of  $E_{gap} = 103 \text{ kV}/\text{cm}$ .

The charge difference for different fluxes is not yet understood. The electric field in the gas gap has been calculated already taking into account the flux effects. In an ideal case, the curves should merge in a single curve, however this is not the case.

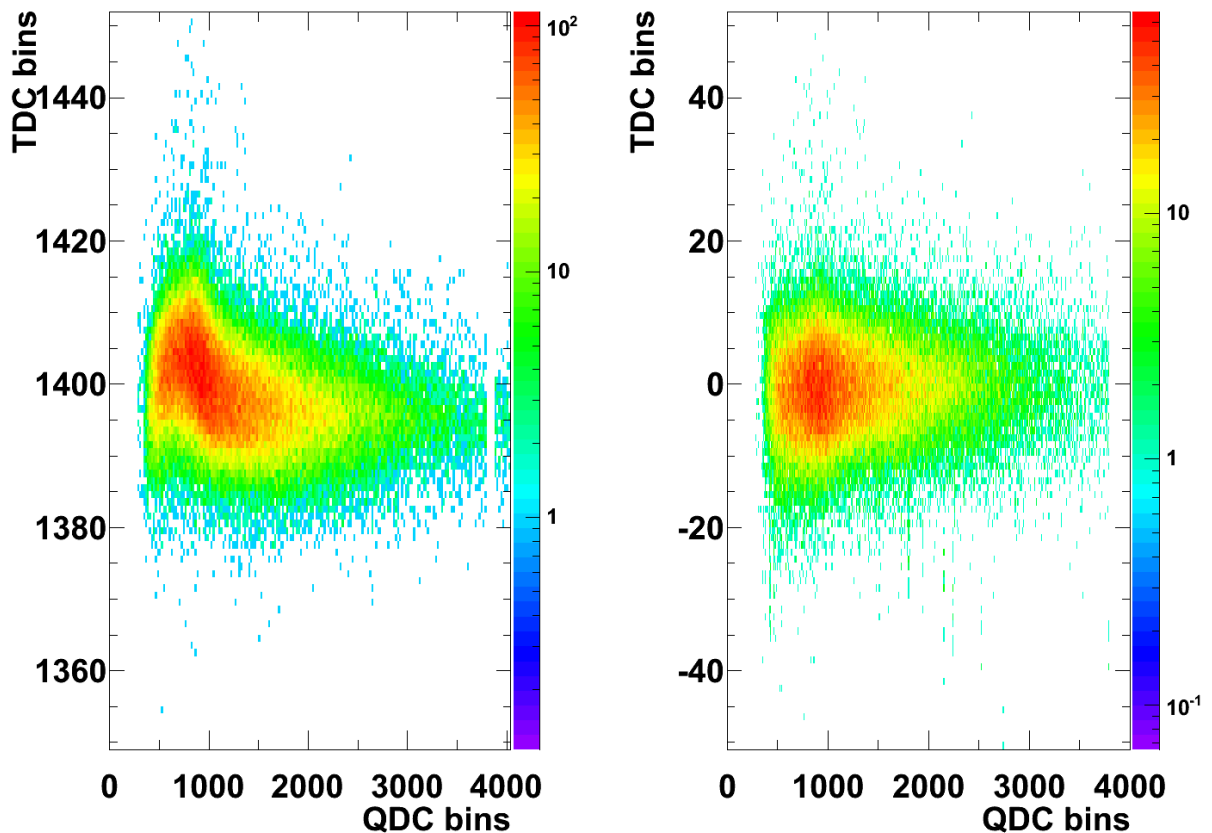


Figure 6.2.: Left: Time-charge spectra before walk correction. Right: Time-charge spectra after walk correction.

## 6.4. Working curve

### 6.4.1. CRPC3b

The working curve of a detector represent the parameters, efficiency and time resolution, as a function of the electric field. The working curves of the RPC prototypes were measured for different fluxes. The result for CRPC3b is shown in Figure 6.5. The results shown in the figure correspond to working curves taken under electron beam exposure for different incoming particle rates. The curve shows an increase of the efficiency with increasing electric field in the gas gap. This is a consequence of a higher Townsend coefficient for the avalanches. Thus, the charge contents of the avalanche have a higher probability to surpass the threshold which translates into a higher efficiency. It is observed that for the highest electric field of 100 kV/cm the efficiency dependence on the high voltage has not reached yet a plateau. It is expected that for the mixture used 85%  $C_2H_2F_4$ / 10%  $SF_6$  /5%  $iC_4H_{10}$ , the detector should exhibit a streamer free region in which the efficiency will remain constant. This region should be in the order of a few hundred volts per centimetre. Even though the nominal voltage is about 5.3 kV at the highest values, which corresponds

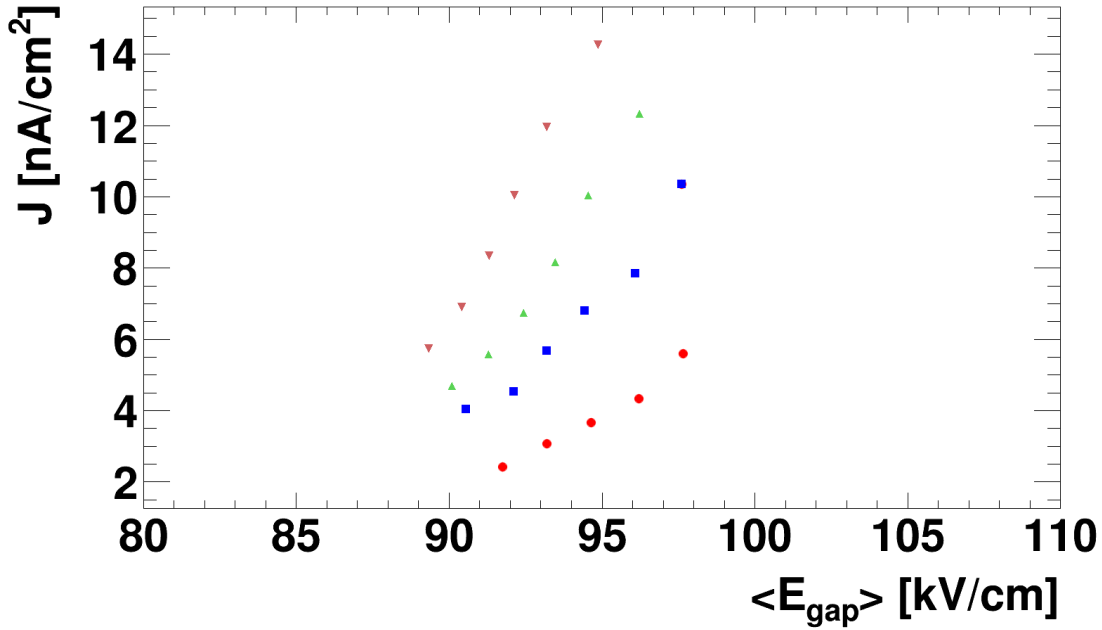


Figure 6.3.: Current density,  $J$ , as a function of electric field strength,  $\langle E_{gap} \rangle$ , for a  $20 \times 20 \text{ cm}^2$  RPC (CRPC3b) irradiated with 30 MeV electrons. Red bullets (●) for fluxes of  $3.8 \times 10^3 \text{ cm}^{-2} \text{ s}^{-1}$ , blue squares (■) for  $9.5 \times 10^3 \text{ cm}^{-2} \text{ s}^{-1}$ , upper triangles (▲) for  $24 \times 10^3 \text{ cm}^{-2} \text{ s}^{-1}$  and lower triangles (▼) for  $54 \times 10^3 \text{ cm}^{-2} \text{ s}^{-1}$ .

to an electric field strength of 106 kV/cm, the electric field in the gas gap calculated with the DC model is much lower not reaching even 100 kV/cm for the highest fluxes. This is a consequence of the large currents drawn by the detector. The electric field decreases strongly due to the continuous currents flowing through the plates. Furthermore, this is a consequence of using low resistivity semiconducting ceramics in the detector. It was shown in Chapter 4 that the current does not come from the edges as it was at previously supposed. This current is inherent to the system and has to be taken into account when operating the detector. A possible solution for this drawback is to increase the nominal voltage, thus increasing the electric field strength in the gas gap.

Figure 6.5 also shows that the curves do not completely superimpose to each other. As mentioned above, the efficiency depends on the electric field strength in the gas gap (or correspondingly to the voltage drop  $\langle V_{gap} \rangle$ ). Therefore, plotting the efficiency as a function of  $\langle E_{gap} \rangle$  should provide a unique curve even for different fluxes. This effect has already been observed in other high rate experiments with RPCs [92]. The explanation is the large background current. The multi-gap structure relies on the high resistivity of the electrodes to self-equilibrate the voltage drop between the different gaps. For low rates, the current is dominated by the dark current. In the analysis, the dark current was carefully measured and is subtracted from the experimental values. Thus, the curve for low rate shown in Figure 6.5 (red bullets, ●) is shifted towards a higher electric field strength values than the others. It is also shown that for fluxes higher than  $10^4 \text{ cm}^{-2} \text{ s}^{-1}$  the curves overlap to

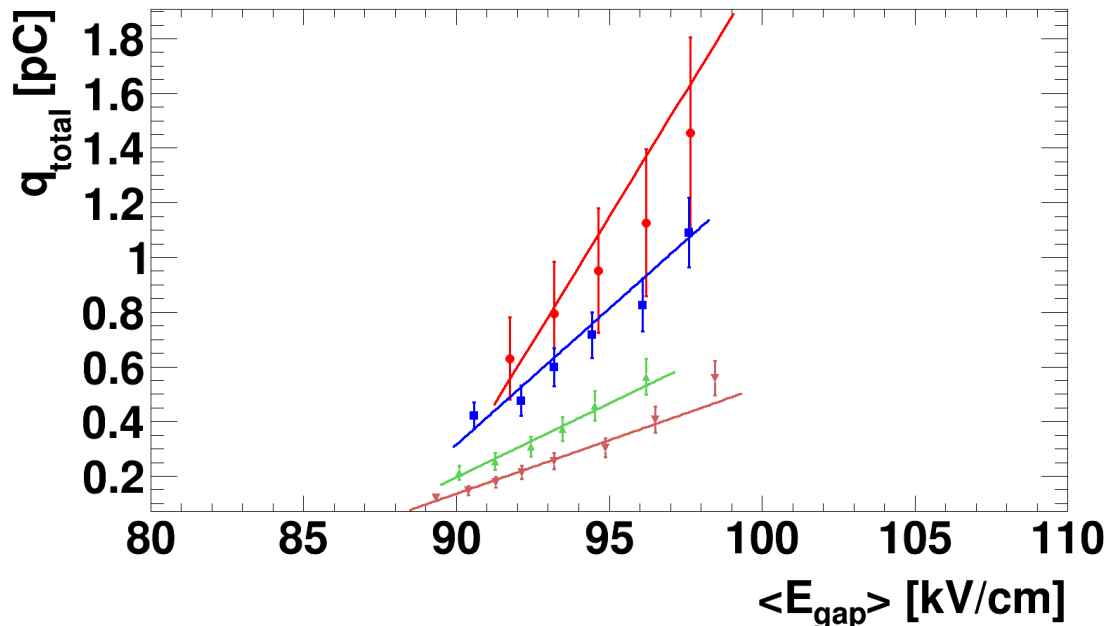


Figure 6.4.: Charge released by the avalanches,  $q_{total}$ , as a function of the electric field strength,  $\langle E_{gap} \rangle$ , for CRPC3b. The colour and symbol code is the same as Figure 6.3.

each other. This is a minimum value where one can assume that the ionization current dominates in the detector.

The time resolution as a function of the electric field strength was also studied. The results are shown in Figure 6.6. The time resolution appears not to depend on the electric field strength in the gas gap. The field was calculated like in the previous sections, thus the overlapping of points. The red bullets ( $\bullet$ ) correspond to a incoming particle flux of  $3.8 \times 10^3 \text{ cm}^{-2} \text{ s}^{-1}$ , the blue squares ( $\blacksquare$ ) to a flux of  $9.5 \times 10^3 \text{ cm}^{-2} \text{ s}^{-1}$ , the upper triangles ( $\blacktriangle$ ) to  $24 \times 10^3 \text{ cm}^{-2} \text{ s}^{-1}$  and lower triangles ( $\blacktriangledown$ ) to  $54 \times 10^3 \text{ cm}^{-2} \text{ s}^{-1}$ . The time resolution does not seem to deteriorate with these fluxes. The most probable cause is the low charges collected by the RPC. This fact triggered the design of a differential prototype with  $20 \times 20 \text{ cm}^2$  active area and six gas gaps with gap widths of  $250 \mu\text{m}/\text{gap}$ . However, that detector was not yet successfully tested in beam by the time this work was written. The dark current improvement due to rounded edges was shown already in Chapter 4.

### 6.4.2. ITEP1 and ITEP2

In the case of  $\text{Al}_2\text{O}_3$  Rogowski-shaped electrodes the results are shown in Figure 6.7. Two different prototypes with the same characteristics were tested at the same electron beam. Both detectors consisted of  $2 \times 3$  gaps with gap widths of  $250 \mu\text{m}$ . In the figure the efficiency for different cuts in the data is shown. The green squares ( $\blacksquare$ ) correspond to the efficiency estimated by selecting events in the trigger and an additional scintillator (S6) placed behind the RPC. The same cuts were applied for the other detector and the



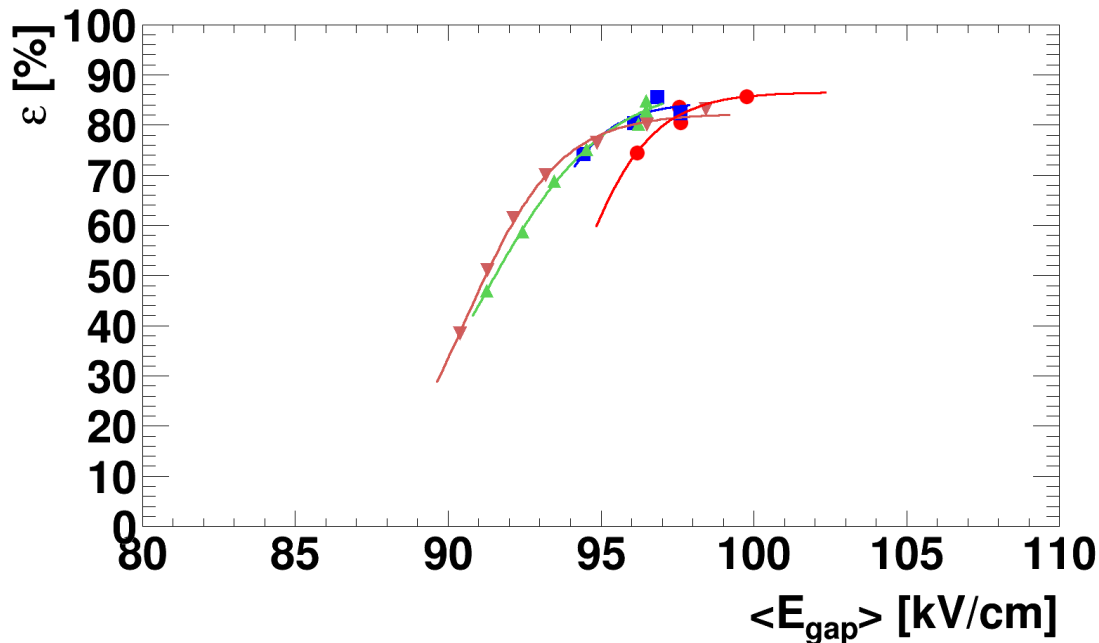


Figure 6.5.: Efficiency as a function of the electric field in the gas gap for different fluxes. The prototype was CRPC3b irradiated by 30 MeV electrons. The colour code is the same as Figure 6.3.

result is shown with upper triangles ( $\blacktriangle$ ). Both detectors show comparable efficiency for these cuts. However the low efficiency of around 60% is the result of geometrical factors. There is a high number of electrons which generate a trigger signal but do not cross the detector due to low angle scattering. To prove this, two small additional scintillators (S13 and S14) were placed covering a region of 50 mm<sup>2</sup> on the RPC. With additional cuts on these scintillators, shown as lower triangles ( $\blacktriangledown$ ), the efficiency rises to 88% for an electric field strength in the gas gap of 93 kV/cm.

## 6.5. Rate scan

The evolution of the operating parameters as a function of the incoming particle flux was determined through a series of systematic rate scans. The flux determination at the surface of the RPC for non-uniform irradiation has been described in subsection 5.2.5.

### 6.5.1. CRPC2b

The efficiency for a 10×10 cm<sup>2</sup> RPC (CRPC2b) is shown in Figure 6.8. This efficiency remains higher than 90% for fluxes up to 4×10<sup>5</sup> cm<sup>-2</sup> s<sup>-1</sup>. No decrease is observed. The limitations on the rate scan were given by the trigger scintillating counters used. The rates for the scintillators can be in the order of 10<sup>9</sup> s<sup>-1</sup>. Taking into account that the average dead time for a scintillating counter is about 10 ns, at the highest rates signal pile-up

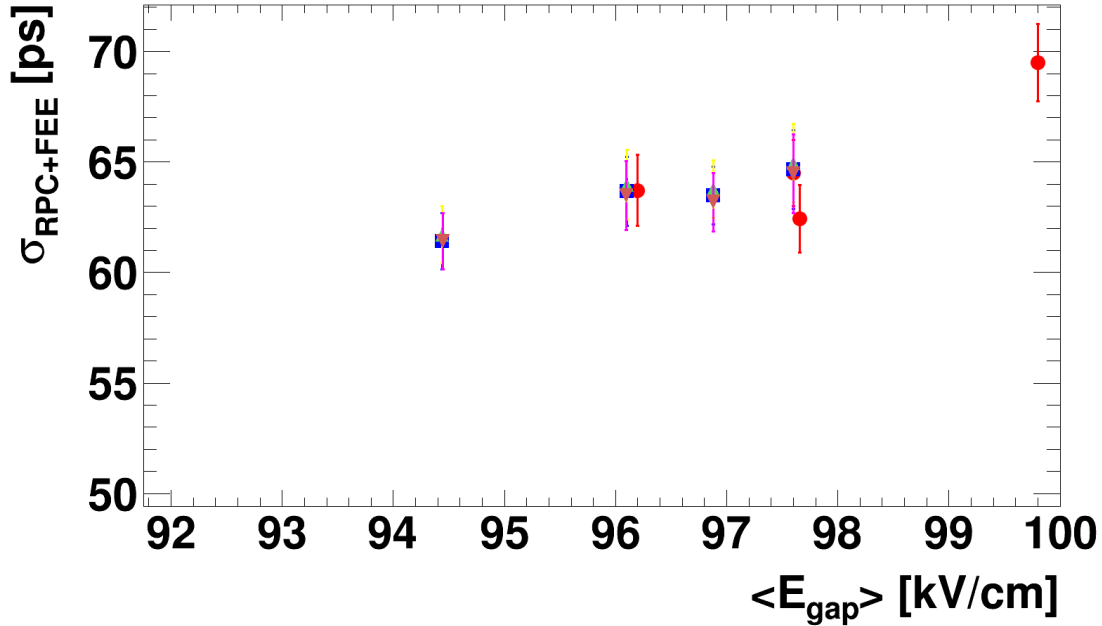


Figure 6.6.: Combined time resolution of the RPC and FEE  $\sigma_{RPC+FEE}$  as a function of the electric field in the gas gap  $\langle E_{gap} \rangle$ . The data is for CRPC3b. The colour legend is the same as Figure 6.5.

becomes significantly higher. Furthermore, at such high beam intensities the coincidence starts to become heavily affected by random coincidences. The cuts performed in the timing spectra of the scintillating counters reduced the uncertainties introduced by these effects. By asking a valid timing signal (that is,  $\pm 2$  ns around the main peak) spurious events are easily discarded.

As opposed to the efficiency, the time resolution worsens with increasing particle flux. These detectors operate with a strong dark current ( $\sim 30 \mu\text{A}$  at 100 kV/cm), therefore the DC model could not be applied. The electric field strengths quoted are the ones obtained directly from the voltage power supply and are just presented as guidance. Several conclusions can be drawn from the data, however. The efficiency remains high even for the higher fluxes at  $3 \times 10^5 \text{ cm}^{-2} \text{ s}^{-1}$  and above. The time resolution worsens with the increasing flux. This is a different situation as the one discussed in the previous section for the large prototype. When analysing the prompt charge, it was observed that there was a small decrease for the highest fluxes. However, the charge remained well above the pedestal of the QDC. Therefore, in this case the voltage drop in the electrodes implies a shift of the time-charge spectra towards the low charges, where the influence of the electronics is stronger and the timing peak widens. The efficiency remains unaffected because the charges are still well above the detection threshold, thus a much higher voltage drop is needed to observe a deterioration of the efficiency. When comparing with the proton beam data, the efficiency remains constant although at a much lower value than for the electron

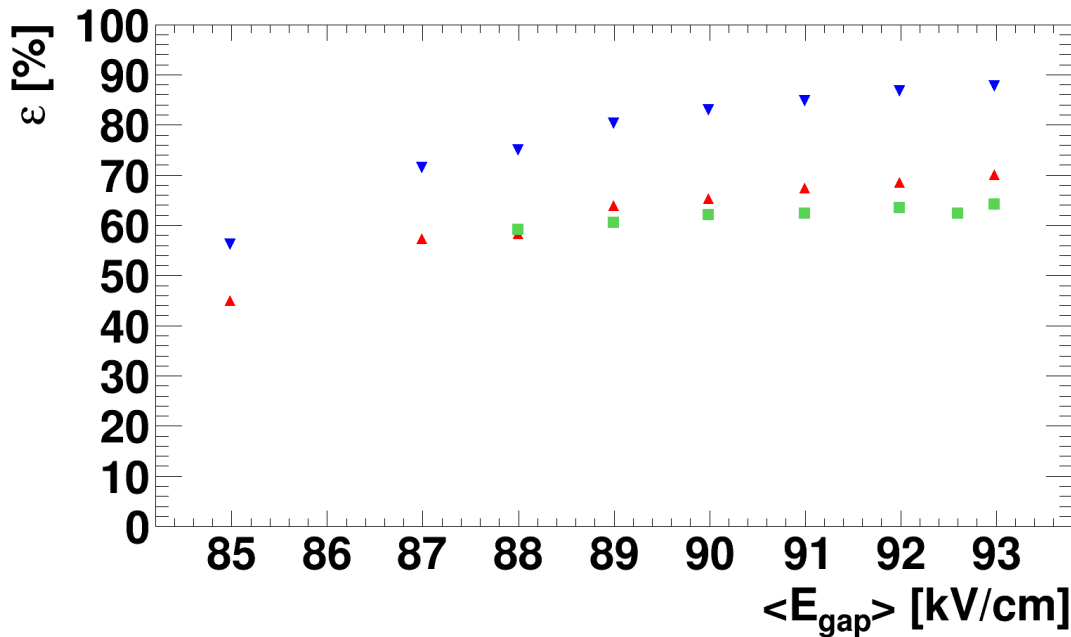


Figure 6.7.: Efficiency,  $\varepsilon$ , as a function of the electric field strength in the gap,  $\langle E_{gap} \rangle$  for two prototypes and trigger conditions. Green squares (■) corresponds to ITEP1 and cuts on the trigger + S6, upper triangles (▲) correspond to ITEP2 and same cuts and lower triangles (▼) correspond to ITEP2 and cuts on every scintillator.

beam. This effect is not yet understood. It was observed that the charges collected by the QDCs are not correlated to any considered parameter of the RPC, nor are they correlated to the incoming particle flux, indicating a set-up problem for the charges. The timing signals were checked and indeed a time resolution deterioration is observed. The results are shown in Figure 6.9. The red bullets (●) correspond to electron beam irradiation at a nominal effective field of 106 kV/cm, the blue squares (■) correspond to a nominal electric field of 100 kV/cm and the green triangles (▲) to proton beam irradiation at a nominal voltage of 100 kV/cm. It is apparent that the high rate capabilities for this prototype are confirmed in both tests.

### 6.5.2. CRPC3b

The same study was done for a larger prototype of size  $20 \times 20 \text{ cm}^2$ , CRPC3b. The rate scan was done under electron beam irradiation and proton beam irradiation. The efficiency as a function of the local incoming particle flux is shown in Figure 6.10. The efficiency corresponding to electron beams is depicted for four different voltages set on the power supply. The efficiency corresponding to proton beams is also plotted. The data was fit to the model once the dependence of  $\langle V_{gap} \rangle$  and  $\bar{\phi}$  was obtained. There is a good agreement between the data and the model. Also, the model agrees with the results for both types of incoming particles. It is shown that for the electron beam the drop in the efficiency

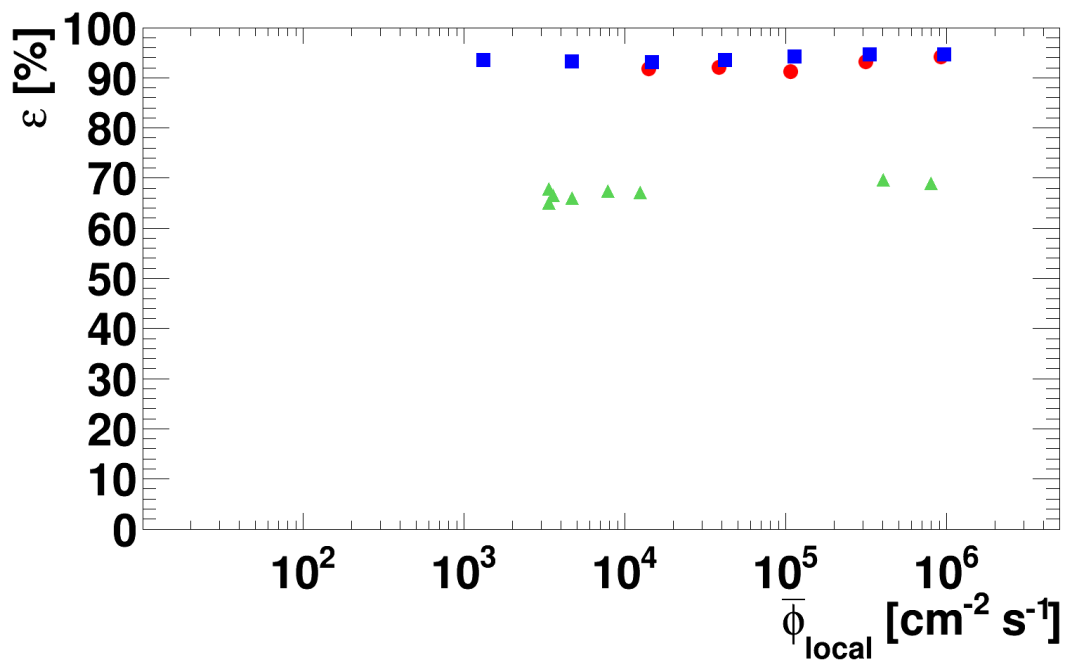


Figure 6.8.: Efficiency as a function of incoming particle local flux,  $\bar{\phi}_{local}$  for electron irradiation at  $E_{nominal} = 100 \text{ kV/cm}$  (●) and  $106 \text{ kV/cm}$  (■) and proton irradiation at  $E_{nominal} = 100 \text{ kV/cm}$  (▲). The detector tested was CRPC2b.

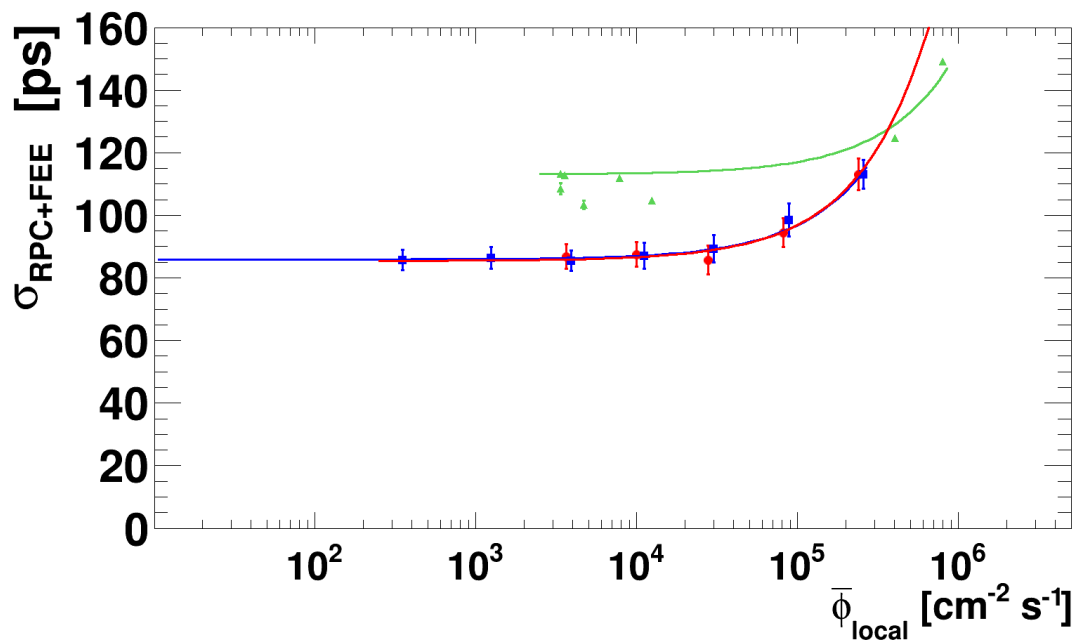


Figure 6.9.: Time resolution,  $\sigma_{RPC+FEE}$  as a function of local incoming particle flux,  $\bar{\phi}_{local}$ . The colour code is the same as Figure 6.8.

happens earlier than in the proton beam. This is also visible in the behaviour of  $\langle V_{gap} \rangle$ . In the case of the proton beam, the voltage in the gas gap decreases much slower than in the case of the electron beam. This has been observed before and reported in [93]. Testing RPCs with focused and defocused beams, and comparing to previous results [94], the authors concluded that the decrease in efficiency was a consequence of the charging of the plates. In the measurements presented here, we can also conclude that, indeed, the charging of the plates is a significant factor in the efficiency. Also, we can conclude that the charging of the plate depends on the size of the beam. An interesting question is, what happens under a higher rate in the case of electron irradiation? The red and blue points in Figure 6.10 corresponding to the lower voltages clearly drop much earlier than the proton beam data, and the model confirms it. However, extrapolating along the line of the fit for the higher electric fields under electron irradiation might overlap the points of the proton beam, thus requiring a different explanation as to why that happens. This must remain an open question at the moment due to insufficient data. The rate capabilities can then be obtained by calculating the flux at which the efficiency drops a 10%. The rate capabilities thus obtained with the proton beam are higher by a factor ten than the ones obtained with the electron beam. A 10% decrease under proton irradiation occurs at  $4 \times 10^5 \text{ cm}^{-2} \text{ s}^{-1}$ , whereas the same drop happens under electron irradiation at  $4 \times 10^4 \text{ cm}^{-2} \text{ s}^{-1}$ . The beam-spot in the proton beam had a size  $A_p = 0.49 \text{ cm}^2$ , while the electron beam had a size  $A_{e^-} = 10 \text{ cm}^2$ . This results in an irradiation of 0.1225% of the detector in the case of protons and 2.5% in the case of electrons. This shows that to obtain an unbiased efficiency, uniform irradiation tests are needed where the whole surface is illuminated.

The time resolution is also estimated and represented in Figure 6.11. For the electron beam it remains constant at a value of  $\sigma_{RPC+FEE} \sim 60 \text{ ps}$  up to fluxes of  $10^5 \text{ cm}^{-2} \text{ s}^{-1}$ . In the case of the proton beam, this value is also 60 ps for the same fluxes and then deteriorating up to 150 ps for the highest flux of about  $1.5 \times 10^6 \text{ cm}^{-2} \text{ s}^{-1}$ . The difference to the lowest fluxes, in which the time resolution amounts to 80 ps for the proton beam, is due to the set-up. The synchronization between the TDCs at ELBE is performed via the accelerator's RF which has a resolution of 30 ps, while the synchronization at COSY was changed during the experiment. The effects of both synchronizations were measured in both cases by feeding the same signal to different TDC channels and making time differences between them. In the case of the electron beam, it consistently achieved a resolution per channel of 30 ps while at the proton beam was 50 ps.

## 6.6. Position resolution

At the beginning, RPCs were intended to be used as trigger. For these purposes, a low granularity was sufficient. With the development of timing RPCs and more granular systems, the position resolution of the detectors started to improve. As shown in Chapter 2, the position resolution depends on the speed of the signal along the strip and on the resolution of the electronics. As far as 2003, there were several studies on the potential of RPCs for tracking purposes [95, 96]. This early prototypes achieved spatial resolutions of  $300 \mu\text{m}$  in the case of [95] or 3 mm in the case of [96]. This developments opened the door

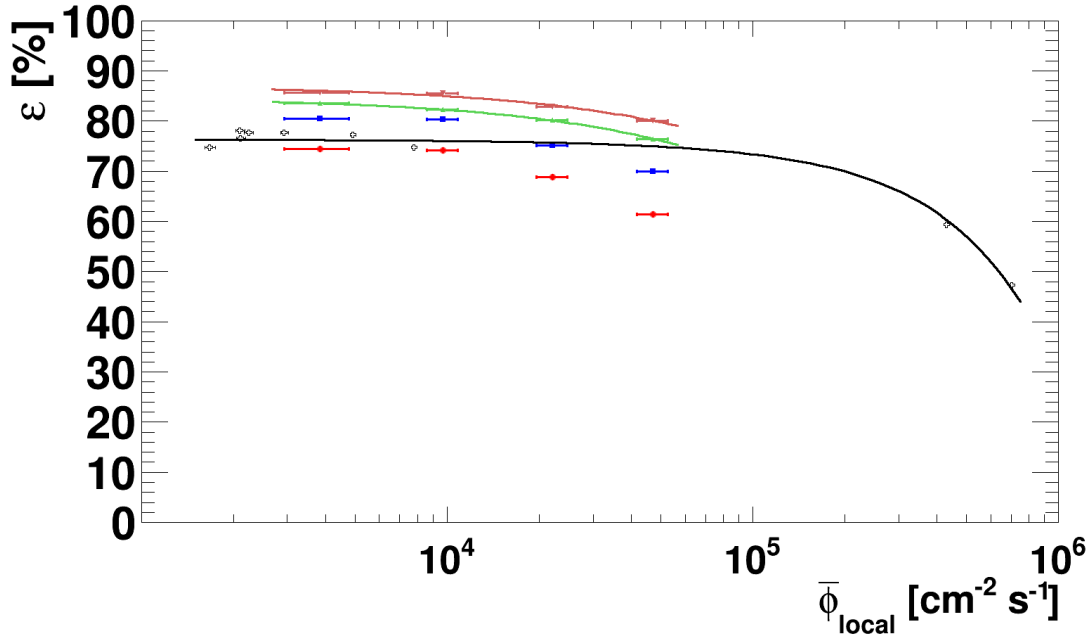


Figure 6.10.: Efficiency  $\varepsilon$  as a function of the incoming particle flux  $\bar{\phi}_{local}$ . CRPC3b under electron beam and operating at 92 kV/cm is shown with bullets  $\bullet$ , at 94 kV/cm with squares  $\blacksquare$ , at 96 kV/cm with upper triangles  $\blacktriangle$  and at 98 kV/cm with lower triangles  $\blacktriangledown$ . CRPC3b under proton beam and operating at 95 kV/cm is shown with crosses  $+$ . Lines correspond to fits to the model.

of tracking with RPCs, not only in high energy physics experiments but also in the field of medicine. Experiments like OPERA [97] use RPCs for tracking. Recent results show that RPCs can indeed have resolutions in the order of 200  $\mu\text{m}$  with bakelite electrodes [98]. There are also proposals to use RPCs for Positron Emission Tomography (PET) systems like [99].

The position resolution of CRPCs was tested with the proton beams. In that test, the physical dimensions of the beam were  $\text{RMS}_x = 2.5 \text{ mm}$  and  $\text{RMS}_y = 5.8 \text{ mm}$ . The time difference between both sides of the irradiated strip in the detectors is shown in Figure 6.12. The upper panel corresponds to the  $10 \times 10 \text{ cm}^2$ , prototype CRPC2b, and the lower panel to the  $20 \times 20 \text{ cm}^2$ , prototype CRPC3b. The spatial resolution of the detector is obtained as the  $\sigma$  of the Gaussian fit. The small prototype has a resolution  $\sigma_x = 1.0660 \pm 0.0070 \text{ cm}$  and the large one  $\sigma_y = 0.9855 \pm 0.0060 \text{ cm}$ . The spatial resolution is mainly affected by the electronics employed. Both RPCs were equipped with FOPI electronics. Also their strip widths were very similar, with a difference of 1 mm. The length of the strips was 10 cm and 20 cm, respectively. Therefore we can conclude that the spatial resolution of these prototypes with the FOPI electronics is 1 mm. These values were obtained without weighting by the charge collected by the strips. There are different methods, like charge-weighting, by which it is possible to select the strip with the highest charge. This methods

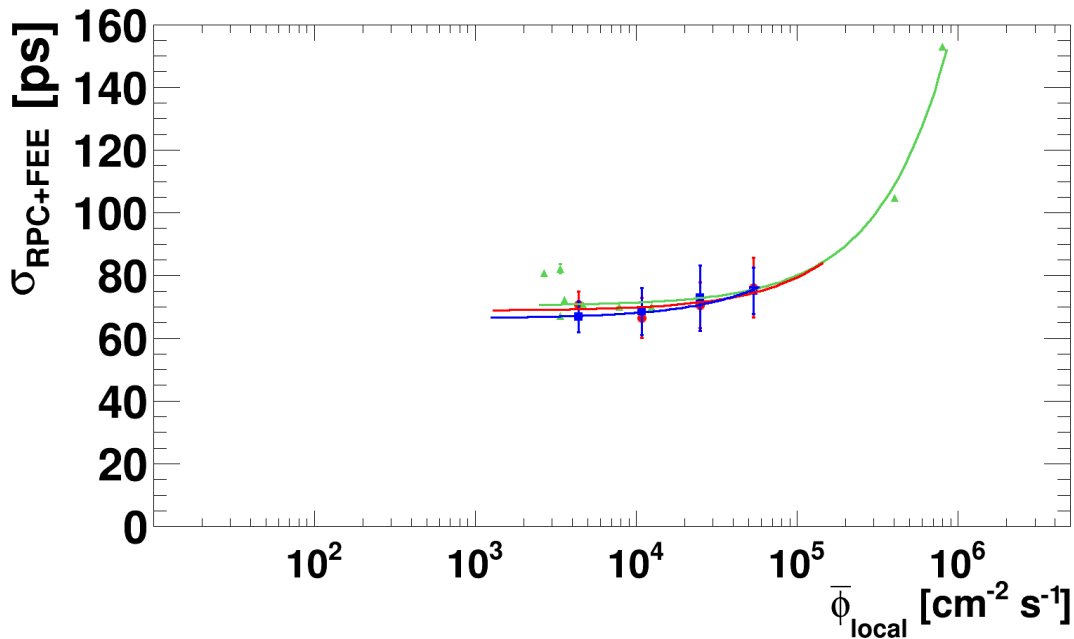


Figure 6.11.: Time resolution,  $\sigma_{\text{RPC+FEE}}$  as a function of the incoming particle flux for different working conditions. The points correspond to experimental data: Red bullets ( $\bullet$ ) to an electron beam exposure at an nominal RPC electric field of 96 kV/cm, blue squares ( $\blacksquare$ ) to a nominal electric field of 98 kV/cm, green upper triangles ( $\blacktriangle$ ) correspond to a proton irradiation at a nominal electric field of 95 kV/cm. The lines represent a linear fit to the data.

are used because when a signal crosses the detector, one or more strips can fire at the same time. The study of the number of strips fired by event is presented in the next section.

## 6.7. Cluster size

Cluster size is one of the critical aspects of multi-strip RPCs. In any event, there is a probability that a certain number of strips fires. The average number of strips fired per event is called the cluster size,  $\bar{n}_s$ . This effect complicates the physics analysis due to the intrinsic problem of assigning a track to every hit. To minimize this problem the causes must be analysed.

Cross-talk effects seem to be the most probable candidates in the case of CRPCs [71]. Crosstalk has been thoroughly studied and even some solutions for its minimization have been proposed [100]. It has been simulated for a general two-strip structure and it was found out that the fraction of signal induced in the neighbours through cross-talk depends on two physical factors: (*i*) an inducto-capacitive coupling between the strips and (*ii*) a modal dispersion of the signal progressing through the strip. While the second factor can be minimized by adjusting the capacitances in the detector (process called “compensation”) the first one is due to the fact of having two strips next to each other. In the case of CRPCs

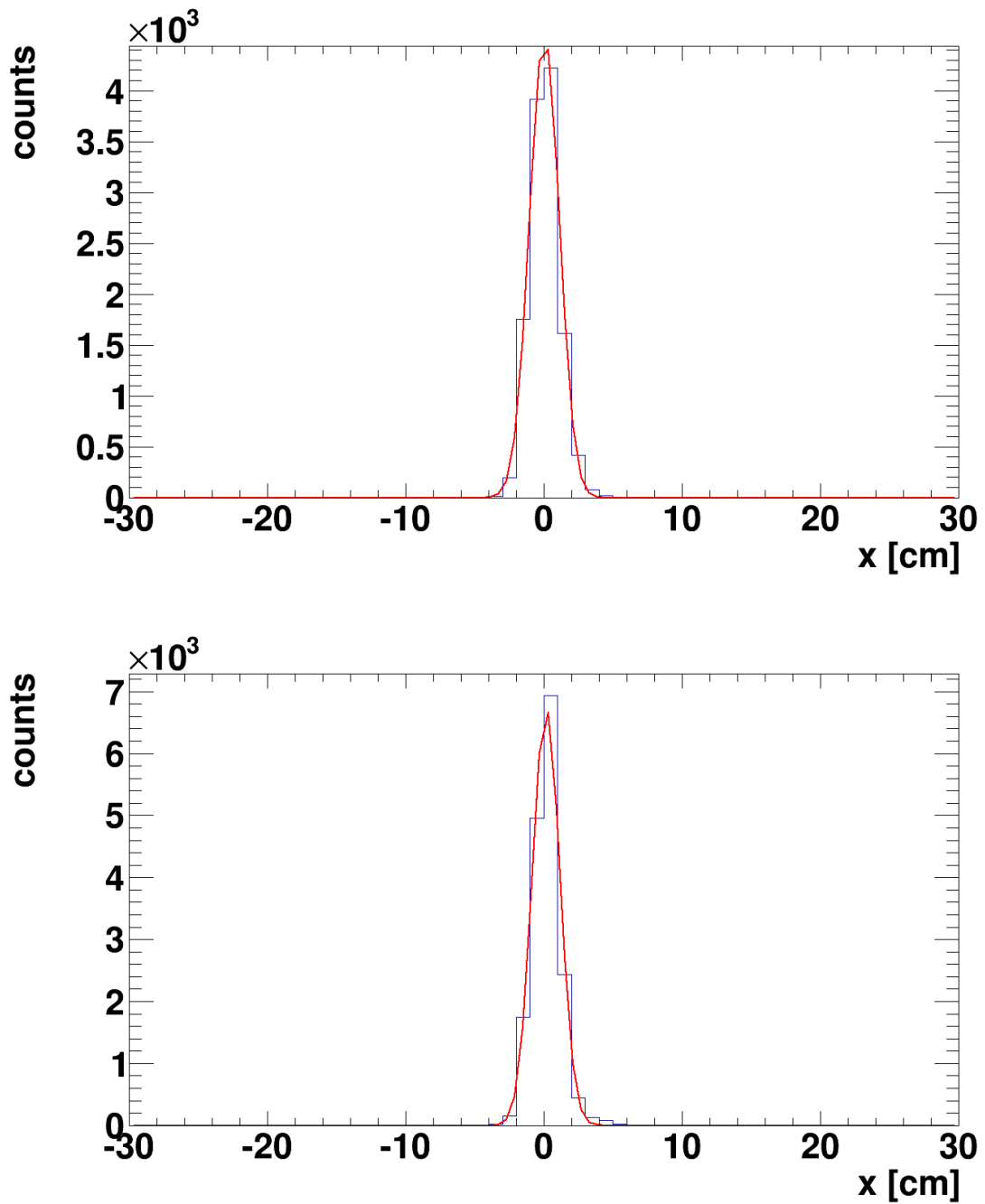


Figure 6.12.: Spatial resolution for CRPC prototypes under proton irradiation. Upper panel: CRPC2b. Lower panel: CRPC3b.

the read-out structure has not yet been optimized thus it is expected that cross-talk plays a large role for the cluster size.

The data collected with the CRPC3b prototype was analysed. The cluster size was studied as a function of the electric field. Figure 6.13 shows the average of the cluster size



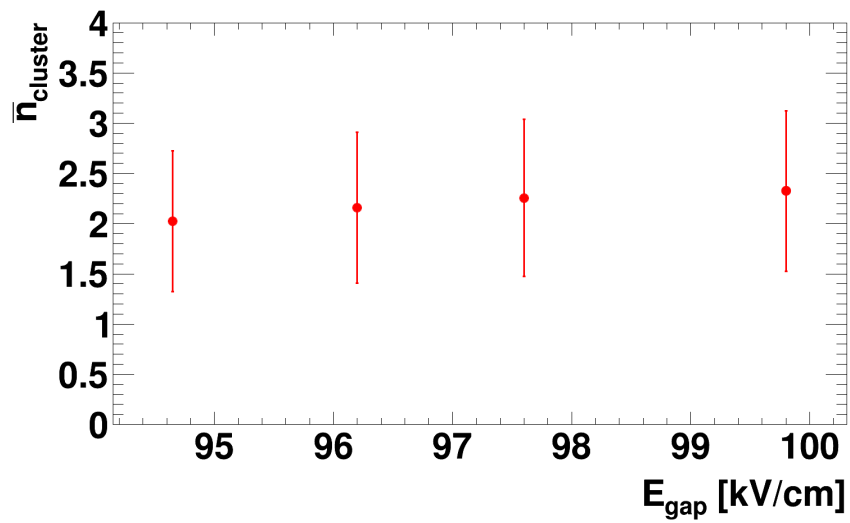


Figure 6.13.: Average cluster size as a function of the electric field for CRPC3b. The flux was  $3.8 \times 10^3 \text{ cm}^{-2} \text{ s}^{-1}$ .

distribution. The RMS was taken as uncertainty. The distribution peaks at 2. However, the uncertainties are so large because a high number of events have  $\bar{n}_{\text{cluster}} > 2$ . Therefore, an average of 2-3 strips fired per event are to be expected when operating this detectors.



## 7. Conclusions and Outlook

This thesis presents the developments of ceramic RPCs for high rate environments. The main goals have been the characterization of innovative electrode materials like  $\text{Si}_3\text{N}_4/\text{SiC}$  composites or  $\text{Al}_2\text{O}_3$  with chromium deposited layers.

The results of detailed characterization of the materials are shown in Chapter 3.  $\text{Si}_3\text{N}_4/\text{SiC}$  have intrinsic properties that makes them interesting for RPCs implementation. The possibility of tuning the material resistivity during the manufacturing process allows for the construction of RPCs targeted to specific flux ranges. The chemical resistance of the material is an advantage when compared to “standard” electrodes materials like glass or bakelite. Ceramics present an inherent resistance to corrosion and the surface is not damaged by acid mixtures formed in the gas gap during operation. They are also resistant to the ageing induced by the transported charge over the bulk of the material. Their varistor nature allows the resistivity to decrease when higher charges are transported. The ceramics can also recover from spark damage. Tests in the laboratory under streamer modes and heavy discharges showed that the surface of the plates was simply darkened by the discharges. This could be easily cleaned. Afterwards the plates were ready to be implemented again in the detector.

The assembly of the detectors and comparison between different architectures has been explained in Chapter 4. CRPCs have been systematically assembled and tested. The first step has been the proving of scalability. The active surface of the RPCs have increased a factor four, going from  $10 \times 10 \text{ cm}^2$  in CRPC1 and CRPC2b, to  $20 \times 20 \text{ cm}^2$  in CRPC3b, CRPC4 and CRPC6. Special and innovative hybrid ceramic RPCs have also been assembled in collaboration with the Institute for Theoretical and Experimental Physics in Moscow. This “dielectric” RPCs present a combination of HZDR ceramics with  $\text{Al}_2\text{O}_3$  electrodes with metallic layers. The concept has been proven to work stably with a butaneless gas mixture. Important results on discharge quenching have also been obtained. The minimum bulk resistivity needed to operate in reasonable streamer-free conditions is  $\rho \geq 10^8 \Omega \text{ cm}$ . The fields at the edges of the electrodes and their influence in the dark current were also studied. The knowledge acquired resulted in an improved prototype with rounded edges with dark currents less than  $20 \text{ nA cm}^{-2}$ .

Chapter 5 describes the experimental set-ups used during in-beam tests. Special emphasis is placed in the beam characterization. Different methods of beam quality monitoring are presented: emulsion plate, scintillator measurement, fiber hodoscope measurement and RPC profile extraction. The calculation of average local flux is discussed with a mathematical explanation in appendix A. Photographs showing the experimental set-ups for time-of-flight systems are found in appendix B.

The analysis of the data is described in Chapter 6. First an introduction of the calculation of the electric field in the gas gap is given. The conditions of the analysis are discussed. Finally the results are presented. The performance of CRPCs with HZDR ceramics are

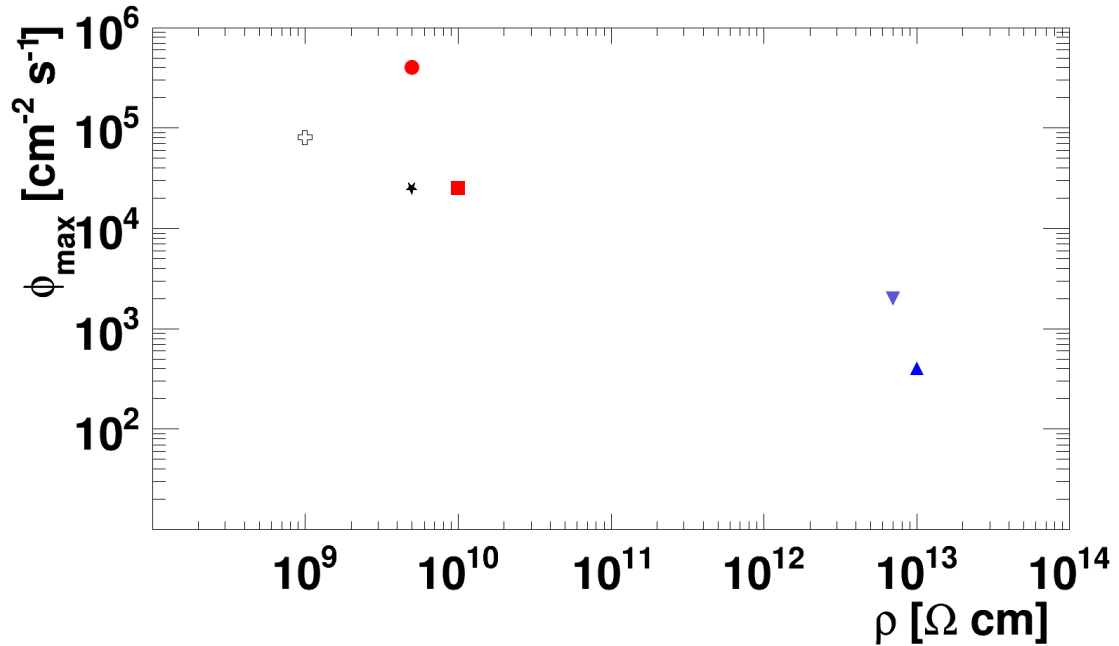


Figure 7.1.: World map of RPC rate capabilities developments. The maximum flux, at which the efficiency drops by 10% is plotted against the bulk resistivity of the material. The red circle is for CRPC2b, the red square is for CRPC3b, the upper triangle is for silica glass [22], the lower triangle is for warmed silica glass [90], the star is for semiconductor-doped glass [101] and the cross is for AL940CD ceramic [63].

discussed in detail in terms of efficiency and time resolution. The fluxes at which these RPCs can operate are unmatched in the field as of today. CRPC2b shows a time resolution  $\sigma \leq 120$  ps for fluxes of  $3 \times 10^5 \text{ cm}^{-2} \text{ s}^{-1}$ . The efficiency remains at 95% in electron beams and 70% in proton beams. It does not show a deterioration. The difference in the results between both types of incoming particles can be traced to set-up differences. CRPC3b has a time resolution  $\sigma \leq 100$  ps for fluxes of  $3 \times 10^5 \text{ cm}^{-2} \text{ s}^{-1}$ . The efficiency stays higher than 80% for fluxes up to  $5 \times 10^4 \text{ cm}^{-2} \text{ s}^{-1}$ .

These results can be compared with other high-rate RPC developments around the world. Figure 7.1 shows such a RPC world map. The high resistive materials like silica glass show poor rate capabilities. If the material is warmed the maximum flux attainable increases moderately. For low resistive materials like semiconductor-doped glass or AL940CD ceramics (no longer in production) or HZDR ceramics the rate capabilities increase. The frontier of  $10^6 \text{ cm}^{-2} \text{ s}^{-1}$  seems to be at reach for the case of the prototypes in this thesis.

Some questions remain open by the time this thesis is written. Many of these questions are specific for the high-rate region and have not been tackled until now. The gas purity is one of them. The current scheme of RPCs relies on diffusion of the gas through the gaps to refresh the gas supply. However it is not proven that at higher fluxes the diffusion

---

is enough. This matter will be addressed by an advanced prototype with direct gas flow in the gaps developed at HZDR. Another advanced prototype based on the information collected in the past years has been developed. CRPC6 features a differential readout and an increased number of gaps (six) while keeping the gap width at  $250\ \mu\text{m}$ . This detector is expected to be tested during 2014 under electron and photon irradiation. The hybrid RPC development is also ongoing. While the efficiency is promising, the time resolution needs to be improved to fulfil the CBM ToF requirements. A special grooving not only in the outer electrode but also in the floating ceramic plates, will allow for the increase of the voltage applied without an increase of the dark current. These detectors are under construction and will be tested at ELBE in 2014.

The primary motivation of this work was the ToF wall of the CBM experiment. The results presented in this thesis show that ceramic RPCs are suitable to cover the most forward part of the ToF wall. Furthermore, the Detector Technologies and Systems program of the Helmholtz Association provide access to unique facilities like the ELBE accelerator in which to perform high-precision time-of-flight detector tests.



# A. Flux estimation for non-uniform beams

The ideal case for testing a detector is to have uniform irradiation conditions covering the whole detector. In that case, the flux over the detector is the same. Furthermore, since the whole active area is covered, averages over the whole RPC can be calculated and the response of the whole counter estimated.

However, the beam at ELBE or COSY is not wide enough to cover the whole counters, neither it is uniform. In the case of the ELBE beam, the shape of the beam was measured several times. The beam shape is described by a Gaussian distribution in both transverse directions, giving an elliptical beam spot on the surface of the RPC. The COSY beam has a pencil shape with a slightly elliptical beam spot. The difficulty in calculating the average flux over a certain area resides in the normalization factor. We want to find an effective beam spot which gives an average flux equal to the flux under uniform irradiation. That is, our goal is to obtain

$$\bar{\phi}_{gauss} = \bar{\phi}_{unif}, \quad (\text{A.1})$$

for a certain area  $A$ . In our tests, the data measured by scintillating detectors allowed to measure rates. So let us consider the rate  $R_0$  measured by a scintillating plastic. The fluxes in both cases will be

$$\frac{R_0\gamma}{A} = \frac{R_0}{A}, \quad (\text{A.2})$$

where we introduce the factor  $\gamma$  to account for the geometrical differences in the profile. From our measurements we also know the shape of the beam. It is a 2-dimensional Gaussian with widths  $\sigma_x$  and  $\sigma_y$  (which are both measured). For clarity, let us consider a 1-dimensional case. That is, we have a 1-D Gaussian distribution illuminating a segment of length  $d$  of the RPC. In this case, our *linear* flux is

$$\frac{R_0\gamma}{d} = \frac{R_0}{d}. \quad (\text{A.3})$$

We will try now to determine the factor  $\gamma$ . A Gaussian distribution centred at the origin is given by

$$f(x) = \frac{1}{\sqrt{2\pi}\sigma_x} e^{-\frac{x^2}{2\sigma_x^2}} \quad (\text{A.4})$$

The rate at each spatial point is given by  $R(x) = R_0 f(x)$ . The average over the segment  $d$  is

| Limits      | $\gamma_{1d}$ | $\gamma_{2d}$ |
|-------------|---------------|---------------|
| $\sigma$    | 0.68          | 0.46          |
| $2\sigma$   | 0.95          | 0.90          |
| <i>FWHM</i> | 0.75          | 0.56          |

Table A.1.: Values for  $\langle R \rangle$  normalized to  $R_0$  as calculated by eq. (A.5) and eq. (A.8) for different integration limits.

$$\langle R \rangle = \int_{-d/2}^{d/2} R_0 f(x) dx \quad (\text{A.5})$$

The values of the integral can be found in mathematical tables in the literature. The integral gives a value  $\gamma$  dependant on the integration region. Therefore

$$\bar{R}_g = R_0 \gamma \quad (\text{A.6})$$

The 2-D case is very easy to calculate due to factorization. The distribution is then

$$f(x, y) = \frac{1}{2\pi\sigma_x\sigma_y} e^{-\frac{x^2}{2\sigma_x^2}} e^{-\frac{y^2}{2\sigma_y^2}} \quad (\text{A.7})$$

and the average rate is

$$\bar{R}_g = R_0 \int_{-d_y/2}^{d_x/2} \int_{-d_y/2}^{d_x/2} f(x, y) dx dy \quad (\text{A.8})$$

The two integrals are independent from each other, so one has again a one dimensional integration for each coordinate. The final value is another factor  $\gamma$ . A collection of results for typical integration limits is given in Table A.1.



## B. FEE influence in efficiency estimation

A strip RPC is usually read by both sides. This method offers the possibility of determining the time resolution independent of the position of the primary ionization cluster on a vertical plane along the strip. When using RPCs in large experiments, the information on both sides is also used to determine a point on the track, if the granularity allows it. This method relies on the amplifier properties to be the same in each electronic channel.

As explained in Chapter 4, FEE were used during testing of CRPCs. One disadvantage of the modules used is the large differences between modules and between channels in the same module. The properties of all the cards used were measured with a pulser of known properties. The amplitude amplification for each channel of each card is presented in Figure B.1.

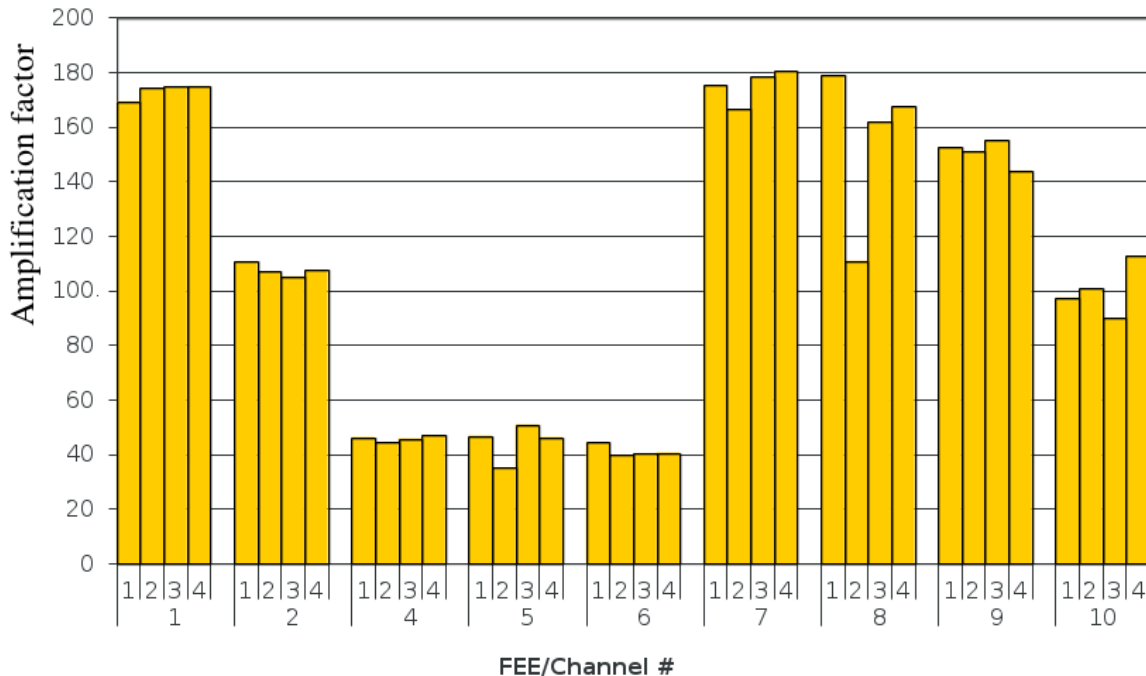


Figure B.1.: The amplitude amplification measured for each channel.

The amplification varies greatly between cards. The difference can be as large as a factor 4 like between card 7 and 6. This is an extremely important difference. The FEE amplify the signals and then discriminate. If one strip was read on one side by card 7 and the other by card 6, it can happen that signals that cross the threshold on one side do not cross it in the other.

A proof of this effect is seen on the profile of strips fired one each side. The measurement of the profile on the left side of an RPCs is shown in the upper panel of Figure B.2 and the corresponding right side in the lower panel. The events were selected by timing signals following the cuts described on Chapter 6. The left side shows a larger number of events recorded for the same number of triggers. The beam was centred on strip 9. The number of events for the left side of this strip amounts to about 18000 while the number of events on the right side is about 33000. This event number difference is attributed to the difference in amplification on both sides. Thus, using a logic AND between both sides of the strips will underestimate the efficiency due to the low amplification of some of the FEE. Whereas using the OR will provide a more accurate estimation.

It is possible to argue that using an OR will overestimate the efficiency due to be considering noise events as valid hits (there might be noise on the electronics or some noise signal that barely crosses the threshold on some cards). However, the cuts in place minimize this effect. A noise signal is by definition a random signal created in the detector not correlated to the arrival of the incoming particle. This would translate in a signal recorded in the TDC *outside* of the main peak and with zero charge (recorded in the QDC as pedestal).

A much more accurate measurement of the efficiency is expect to be reached with the new differential prototype using PADI as amplifier electronics.

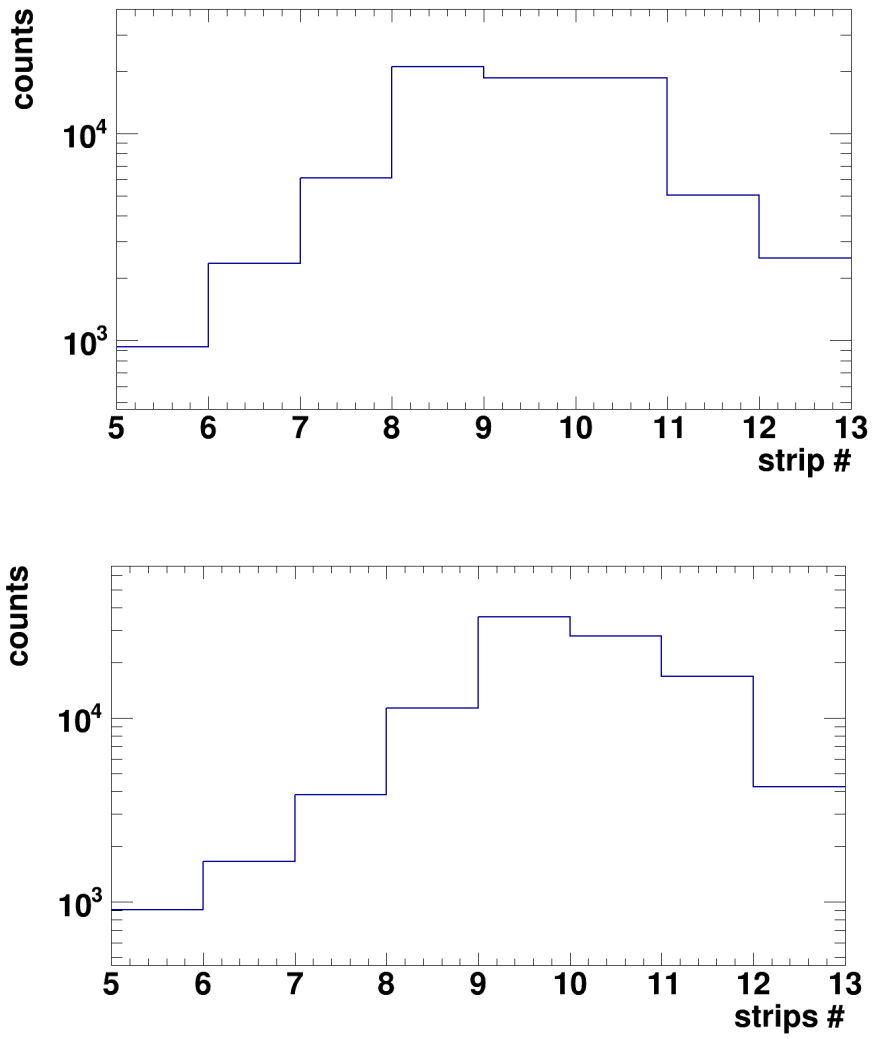


Figure B.2.: Upper panel: strips fired on the left side of CRPC3b. Lower panel: strips fired on the right side.



# Acknowledgements

I would like to thank Prof. Dr. Tomas Cowan, Director of the Institute of Radiation Physics at HZDR for allowing me to do my work at his institute. I would also like Prof. Dr. Burkhard Kämpfer, leader of the Hadron Physics department, for welcoming me into his group.

Special thanks go to Dr. Lothar Naumann for his everyday support while at HZDR. He introduced me to the world of particle detectors, of which he has a vast understanding. Without him, this thesis would not have been possible. To Dr. Roland Kotte I thank his support while setting up our trigger logic and for his special ability to always set the right timing window for the different components. Dr. Jörn Wüstenfeld has my thanks for his support in the most intricate code problems, be it FPGA, TDC or my own programs. Many a segmentation fault error has been averted thanks to him. To my fellow students Richard Peschke, Marcus Kaspar and Christian Wendisch for making every day an interesting one while at work. The technical staff at our Detector Laboratory, specially Daniel Stach and Jochen Hutsch deserve another mention. Daniel built many of the RPCs we tested and offered solutions and support during our tests. Jochen, may he rest in peace, nearly single-handedly built CRPC6 and solved many problems found during assembly.

The CBM-ToF group also receives my thanks for their interesting discussion in our meetings and the support during beam times. Dr. Alexander Akindinov, from ITEP, deserves also a mention. His deep understanding of RPC physics has undoubtedly improved our CRPC research.

Prof. Dr. Eckart Grosse, former director of the Institute for Radiation Physics, initiated originally the research on RPCs for nuclear and particle applications exploiting the unique test opportunities at ELBE. Many thanks to him.

Un párrafo especial en mi propio idioma no puede faltar. Lo escribo para agradecer a mis padres, Juan y Marisa, y a mis hermanos Hugo y Nicolás su continuo apoyo durante todos estos años. Sin ellos, yo no sería quien soy hoy en día.



# Bibliography

- [1] <http://www.world-nuclear.org/info/Non-Power-Nuclear-Applications/Radioisotopes/Radioisotopes-in-Industry/>.
- [2] P. W. Higgs, Phys. Rev. Lett. **13**, 508 (1964).
- [3] F. Englert and R. Brout, Phys. Rev. Lett. **13**, 321 (1964).
- [4] ATLAS Collaboration, “Observation of a new particle in the search for the Standard Model Higgs boson with the ATLAS detector at the LHC”, arXiv:1207.7214.
- [5] R. Santonico, R. Cardarelli, Nucl. Instr. Meth. **187**, 377 (1981).
- [6] R. Santonico and R. Cardarelli, Nucl. Instr. Meth. A **263**, 20 (1988).
- [7] E. Cerron Zeballos, Nucl. Instr. Meth. A **374**, 132 (1996).
- [8] C. Gustavino et al., Nucl. Instr. Meth. A **517**, 101 (2004).
- [9] G. Chiodini et al., Nucl. Instr. Meth. A **581**, 213 (2007).
- [10] A. Colaleo et al., Nucl. Instr. Meth. A **609**, 114 (2009).
- [11] M. Gagliardi, Nucl. Instr. Meth. A **661**, 45 (2012).
- [12] A. Aloisio et al., Nucl. Instr. Meth. A **360**, 340 (1995).
- [13] A. Di Ciaccio, Nucl. Instr. Meth. A **572**, 48 (2007).
- [14] G. Aielli et al., Nucl. Instr. Meth. A **533**, 193 (2004).
- [15] [http://www.atlas.ch/photos/atlas\\_photos/selected-photos/full-detector/ATLAS\\_Silver\\_White\\_MK.jpg](http://www.atlas.ch/photos/atlas_photos/selected-photos/full-detector/ATLAS_Silver_White_MK.jpg).
- [16] R. Arnaldi et al., Nucl. Instr. Meth. A **451**, 462 (2000).
- [17] S. Ahn et al., Nucl. Instr. Meth. A **661**, S41 (2012).
- [18] M. Gagliardi, Nucl. Instr. Meth. A **661**, S45 (2012).
- [19] P. Fonte et al., Nucl. Instr. Meth. A **443**, 201 (2000).
- [20] ALICE Collaboration, *ALICE Addendum to the Technical Design Report of the Time of Flight System (TOF)*, 2002.
- [21] A. N. Akindinov, Nucl. Instr. Meth. A **533**, 74 (2004).
- [22] D. Gonzalez-Diaz, PhD thesis (Universidade de Santiago de Compostela, 2006).
- [23] D. Belver et al., Nucl. Instr. Meth. A **602**, 687 (2009).
- [24] M. Kis et al., Nucl. Instr. Meth. A **646**, 27 (2011).
- [25] A. Schüttauf et al., Nucl. Instr. Meth. A **602**, 679 (2009).

- [26] [http://www.gsi.de/start/fair/forschung\\$\\_%7B%7D\\$an\\$\\_%7B%7D\\$fair/kernmateriephysik.htm](http://www.gsi.de/start/fair/forschung$_%7B%7D$an$_%7B%7D$fair/kernmateriephysik.htm).
- [27] P. Spiller, G. Franchetti, Nucl. Instr. Meth. A **561**, 305 (2006).
- [28] B. L. Friman et al. (Editors), *The CBM Physics Book* (Springer-Verlag, 2010).
- [29] M. Deveaux, J. Phys.: Conference Series **426**, 012020 (2013).
- [30] J. Heuser, W. Müller, et al., [*GSI Report 2013-4*] *Technical Design Report for the CBM Silicon Tracking System (STS)* (GSI, Darmstadt, 2013).
- [31] A. Senger, “Radiation dose calculations for the CBM detectors with FLUKA”, CBM Progress Report 2011.
- [32] M. Koziel et al., Nucl. Instr. Meth. A **732**, 515 (2013).
- [33] C. Höhne et al., Nucl. Instr. Meth. A **595**, 187 (2008).
- [34] A. Andronic, Nucl. Instr. Meth. A **563**, 349 (2006).
- [35] A. K. et al., Nucl. Instr. Meth. A **718**, 418 (2013).
- [36] G. Avoni et al., Nucl. Instr. Meth. A **580**, 1209 (2007).
- [37] R. Dzhelyadin et al., Nucl. Instr. Meth. A **581**, 384 (2007).
- [38] M. C. S. Williams, J. Phys. G: Nucl. Part. Phys. **39**, 123001 (2012).
- [39] The CBM ToF Group, *The CBM Time-of-Flight Wall Technical Design Report*.
- [40] I. Deppner et al., Nucl. Instr. Meth. A **661**, S121 (2012).
- [41] P-A. Loizeau, CBM Collaboration Meeting September 2010.
- [42] L. Naumann et al., Nucl. Instr. Meth. A **635**, 113 (2011).
- [43] M. Petris et al., Nucl. Instr. Meth. A **602**, 679 (2012).
- [44] W. Blum, W. Riegler, L. Rolandi, *Particle Detection With Drift Chambers* (Springer-Verlag, 2008).
- [45] A. N. Akindinov et al., Nucl. Instr. Meth. A **531**, 515 (2004).
- [46] A. Akindinov et al., Nucl. Instr. Meth. A **533**, 93 (2004).
- [47] G. Carboni et al., Nucl. Instr. Meth. A **533**, 159 (2004).
- [48] C. Lippmann, “The Physics of Resistive Plate Chambers” (Johann Wolfgang Goethe-Universität Frankfurt, 2003).
- [49] W. Riegler, C. Lippmann, Nucl. Instr. Meth. A **518**, 86 (2004).
- [50] C. Lippmann, W. Riegler, Nucl. Instr. Meth. A **533**, 11 (2004).
- [51] C. Lippmann, W. Riegler, Nucl. Instr. Meth. A **508**, 19 (2003).
- [52] I. B. Smirnov, Nucl. Instr. Meth. A **554**, 474 (2005).
- [53] R. Veenhof, Nucl. Instr. Meth. A **419**, 726 (1998).
- [54] C. Grupen and B. Shwartz, *Particle Detectors* (Cambridge University Press, 2008).
- [55] H. Raether, *Electron avalanches and breakdown in gases* (Butterworths, 1964).



- 
- [56] M. Kaspar, “Aufbau einer Messanordnung zur Simulation des Verhaltens von Widerstandsplattenzählern (RPC)” (Wstsächsische Hochschule Zwickau, 2012).
- [57] S. Ramo, *Proceedings of the IRE* **27**, 584 (1939).
- [58] I. Deppner, “Development of a fully differential Multi-gap Resistive Plate Chamber for the CBM Experiment”, PhD thesis (Rupert-Carola Universität Heidelberg, 2013).
- [59] M. Kis et al., *Nucl. Instr. Meth. A* **646**, 27 (2001).
- [60] M. Bogomilov, *Nucl. Instr. Meth. A* **508**, 152 (2003).
- [61] A. Akindinov et al., *Nucl. Instr. Meth. A* **661**, 98 (2012).
- [62] J. Wang et al., *Nucl. Instr. Meth. A* **713**, 40 (2013).
- [63] L. Lopes et al., *Nucl. Phys. B (Proc. Supl.)* **158**, 66 (2006).
- [64] C. Lu, *Nucl. Instr. Meth. A* **602**, 761 (2009).
- [65] R. Riedel, I. Chen, *Ceramic Science and Technology. Volume 1: structures* (Verlag, 2011).
- [66] R. Riedel, I. Chen, *Ceramic Science and Technology. Volume 3: Synthesis and Processing* (Verlag, 2011).
- [67] D. Stach, “Entwicklung und Test von Widerstandsplattenzählern hoher Ratenfestigkeit und Zeitauflösung” (Hochschule für Technik und Wirtschaft, 2007).
- [68] *Keithley 485 Picoammeter Data Sheet*, 2009.
- [69] W. J. e. a. Kim, *J. Appl. Phys.* **83** (1998).
- [70] L. Naumann et al., *Nucl. Instr. Meth. A* **628**, 138 (2011).
- [71] R. Peschke, “Charakterisierung der Ratenfestigkeit von Widerstandsplattenzählern” (Technische Universität Dresden, 2011).
- [72] V. A. Gapienko et al., *Instruments and Experimental Techniques* **56**, 265 (2013).
- [73] C. Gustavino, *Nucl. Instr. Meth. A* **527**, 471 (2004).
- [74] D. González-Díaz et al., *Nucl. Instr. Meth. A* **527**, 471 (2004).
- [75] D. Gonzalez-Diaz, *Nucl. Instr. Meth. A* **648**, 52 (2011).
- [76] A. Akindinov, *Nucl. Instr. Meth. A* **494**, 474 (2002).
- [77] W. Rogowski, *Arch. f. Elekt.* **12**, 1 (1923).
- [78] H. Kado, “Performance of the JADE Vertex Detector”, *Proceedings of the Workshop of Radiation Damage to Wire Chambers* (1986).
- [79] M. Ciobanu et al., *IEEE Transactions on Nuclear Science* **54**, 1201 (2007).
- [80] M. Ciobanu, *IEEE Transactions on Nuclear Science* **61**, 1015 (2014).
- [81] Particle Data Group, *Particle Physics Booklet*, 2010.
- [82] A. Bianco et al., *Nucl. Instr. Meth. A* **661**, 114 (2012).

- [83] *ELBE - Center for High-Power Radiation Sources*, <http://www.hzdr.de/db/Cms?pNid=145>.
- [84] [http://www.fz-juelich.de/ikp/EN/Forschung/Beschleuniger/\\_doc/COSY.html](http://www.fz-juelich.de/ikp/EN/Forschung/Beschleuniger/_doc/COSY.html).
- [85] [https://www.gsi.de/en/work/fairgsi/primary\\_beams/existierende\\_anlagen/heavy\\_ion\\_synchrotron\\_sis18.htm](https://www.gsi.de/en/work/fairgsi/primary_beams/existierende_anlagen/heavy_ion_synchrotron_sis18.htm).
- [86] L. Naumann et al., Patent: DE 102008054676, 2011.
- [87] J. Christiansen, *High Performance Time to Digital Converter*, 2004.
- [88] Gesellschaft für Schwerionenforschung, <http://www-win.gsi.de/daq/>.
- [89] G. Carboni et al., Nucl. Instr. Meth. A **498**, 135 (2003).
- [90] D. Gonzalez-Diaz et al., Nucl. Instr. Meth. A **555**, 72 (2005).
- [91] P. Fonte, JINST **8**, P11001 (2013).
- [92] R. Santonico, JINST **8**, P04023 (2013).
- [93] I. Crotty et al., Nucl. Instr. Meth. A **329**, 133 (1993).
- [94] M. Bertino et al., Nucl. Instr. Meth. A **283**, 654 (1989).
- [95] T. Francke et al., Nucl. Instr. Meth. A **508**, 83 (2003).
- [96] A. Blanco, Nucl. Instr. Meth. A **508**, 70 (2003).
- [97] A. Bertolin et al., Nucl. Instr. Meth. A **602**, 631 (2009).
- [98] G. Aielli et al., Nucl. Instr. Meth. A **714**, 115 (2013).
- [99] M. Couceiro et al., Nucl. Instr. Meth. A **661**, S156 (2012).
- [100] D. Gonzalez-Diaz et al., arXiv.1102.1389v1.
- [101] J. Wang et al., Nucl. Instr. Meth. A **621**, 151 (2010).

# List of Figures

|       |   |    |
|-------|---|----|
| 1.1.  | A 3D image of the ATLAS detector . . . . .  | 10 |
| 1.2.  | Detailed schematic of an ALICE timing RPC . . . . .   | 11 |
| 1.3.  | Qualitative representation of the phase diagram of strongly interacting matter . . . . .                          | 12 |
| 1.4.  | CBM modular electron/hadron and muon configurations . . . . .   | 14 |
| 1.5.  | Monte Carlo simulation results of the performance of the CBM-ToF Wall . . . . .                                   | 17 |
| 1.6.  | Flux simulations for the CBM-ToF Wall . . . . .   | 19 |
|       |   |    |
| 2.1.  | Depiction of an avalanche developing in a single-gap RPC . . . . .  | 22 |
| 2.2.  | Primary cluster simulation results as a function of the incoming particle momentum . . . . .                      | 24 |
| 2.3.  | Gas parameter simulation results for two gas mixtures . . . . .   | 26 |
| 2.4.  | RPC signal as seen in a digital oscilloscope . . . . .  | 29 |
|       |   |    |
| 3.1.  | Si <sub>3</sub> N <sub>4</sub> /SiC ceramic wafer during manufacturing . . . . .                                  | 36 |
| 3.2.  | Polished 20×20 cm <sup>2</sup> ceramic plate . . . . .  | 37 |
| 3.3.  | Measurement set-up for determining bulk-resistivity . . . . .   | 38 |
| 3.4.  | Microscope images of surface impurities . . . . .   | 39 |
| 3.5.  | Bulk resistivity dependence on the SiC weight . . . . .   | 40 |
| 3.6.  | Bulk resistivity $\rho$ as a function of the sintering process duration $t$ . . . . .                             | 41 |
| 3.7.  | Logarithm of the current $I$ versus the logarithm of the voltage $V$ for three plates . . . . .                   | 42 |
| 3.8.  | Bulk resistivity dependence on the applied voltage for three plates . . . . .                                     | 43 |
| 3.9.  | Bulk resistivity measured over nine points on a single plate . . . . .  | 45 |
| 3.10. | Bulk resistivity as a function of time for three thin ceramic probes . . . . .                                    | 46 |
| 3.11. | Transmission coefficient $ S_{21} $ as a function of the signal frequency for a line on a ceramic plate . . . . . | 48 |
| 3.12. | A scheme of the different layers on a Al <sub>2</sub> O <sub>3</sub> plate . . . . .                              | 50 |
| 3.13. | Microscope picture, about 2×3 mm <sup>2</sup> , of the metallic surface deposited over the ceramic . . . . .      | 51 |
| 3.14. | Roughness of the chromium layer with a copper substrate . . . . .   | 51 |
|       |   |    |
| 4.1.  | Photograph containing three HZDR RPC prototypes . . . . .   | 53 |
| 4.2.  | Scheme of a 20×20 cm <sup>2</sup> RPC . . . . .   | 54 |
| 4.3.  | Geometry used to calculate the fringe fields at the edge of a parallel plate condenser . . . . .                  | 56 |
| 4.4.  | Microscope pictures of Al <sub>2</sub> O <sub>3</sub> ceramic plate with a chromium layer . . . . .               | 58 |
| 4.5.  | Photograph of an RPC module with Al <sub>2</sub> O <sub>3</sub> electrodes . . . . .                              | 58 |
| 4.6.  | Engineer design of a two-gap RPC with Rogowski-shaped electrodes . . . . .  | 59 |

|       |  |    |
|-------|--|----|
| 4.7.  | 3-D reconstruction of a whisker over a chromium layer . . . . .  | 60 |
| 4.8.  | Photo of a burned region and acid trace around the burning point on a Chromium layer . . . . .   | 61 |
| 4.9.  | Photograph of discharge effects on the cathode metallic layer . . . . .  | 61 |
| 4.10. | Microscope images of rounded edge of a Si <sub>3</sub> N <sub>4</sub> /SiC plate . . . . .   | 62 |
| 4.11. | A depiction of the structures used for simulation the edge field on the semi-conducting ceramics electrodes . . . . .  | 63 |
| 4.12. | Results of a simulation of fringe fields for three edge types . . . . .  | 64 |
| 4.13. | Dark current density as a function of the electric field comparison for three different edge types . . . . .   | 65 |
| 5.1.  | Layout of the ELBE facility at HZDR. Status at January 2014 . . . . .  | 69 |
| 5.2.  | Extracted incoming electron rate as a function of the electron gun voltage .   | 70 |
| 5.3.  | The time distribution of the repetition frequency, $t_{RF+TDC}$ , of the accelerator   | 71 |
| 5.4.  | Experimental set-up for RPC testing with electron beams . . . . .  | 71 |
| 5.5.  | Emulsion plates exposed to the electron beam during two experiments . . .  | 73 |
| 5.6.  | Profiles obtained by scintillator measurement . . . . .  | 74 |
| 5.7.  | Beam spot measured with a fiber hodoscope . . . . .  | 75 |
| 5.8.  | Beam cross section obtained from RPC spectra . . . . .   | 76 |
| 5.9.  | Beam dimension measured with scintillators in different tests runs from September 2010 until November 2013 . . . . .   | 77 |
| 5.10. | Schema of the experimental set-up during the COSY run . . . . .  | 79 |
| 5.11. | On-line reconstruction of the beam spot for a proton beam measured with a fibre hodoscope . . . . .  | 80 |
| 6.1.  | Voltage drop in a single gas gap $\langle V_{gap} \rangle$ as a function of the local particle flux $\bar{\phi}_{local}$ . . . . .                                       | 83 |
| 6.2.  | Time-charge spectra before and after walk correction . . . . .   | 86 |
| 6.3.  | Current density, $J$ , as a function of electric field strength, $\langle E_{gap} \rangle$ . . . . .   | 87 |
| 6.4.  | Charge released by the avalanches, $q_{total}$ , as a function of the electric field strength, $\langle E_{gap} \rangle$ . . . . .                                       | 88 |
| 6.5.  | Efficiency as a function of the electric field in the gas gap for different fluxes   | 89 |
| 6.6.  | Combined time resolution of the RPC and FEE $\sigma_{RPC+FEE}$ as a function of the electric field in the gas gap $\langle E_{gap} \rangle$ . . . . .                    | 90 |
| 6.7.  | Efficiency, $\varepsilon$ , as a function of the electric field strength in the gap, $\langle E_{gap} \rangle$ for Al <sub>2</sub> O <sub>3</sub> ceramic RPCs . . . . . | 91 |
| 6.8.  | Efficiency as a function of incoming particle local flux, $\bar{\phi}_{local}$ for electron and proton irradiation . . . . .   | 92 |
| 6.9.  | Time resolution, $\sigma_{RPC+FEE}$ as a function of local incoming particle flux, $\bar{\phi}_{local}$  | 92 |
| 6.10. | Efficiency $\varepsilon$ as a function of the incoming particle flux $\bar{\phi}_{local}$ . . . . .  | 94 |
| 6.11. | Time resolution, $\sigma_{RPC+FEE}$ as a function of the incoming particle flux for different working conditions . . . . .   | 95 |
| 6.12. | Spatial resolution for CRPC prototypes under proton irradiation. Upper panel: CRPC2b. Lower panel: CRPC3b. . . . .   | 96 |

|  |     |
|--|-----|
| 6.13. Average cluster size as a function of the electric field for CRPC3b. The flux was $3.8 \times 10^3 \text{ cm}^{-2} \text{ s}^{-1}$ . . . . . | 97  |
| 7.1. World map of RPC rate capabilities developments. . . . .  | 100 |
| B.1. The amplitude amplification measured for each channel. . . . .  | 105 |
| B.2. Upper panel: strips fired on the left side of CRPC3b. Lower panel: strips fired on the right side. . . . .                                    | 107 |



# List of Tables

|      |  |     |
|------|--|-----|
| 1.1. | Classification of zones of the CBM-ToF wall . . . . .  | 18  |
| 3.1. | Values of $I_0$ and $\kappa$ obtained from fits to experimental data . . . . .   | 44  |
| 3.2. | Dielectric constant and tangent loss for $\text{Si}_3\text{N}_4/\text{SiC}$ composites and float glass                                   | 49  |
| 3.3. | Radiation dose calculated for several CBM detectors . . . . .  | 49  |
| 4.1. | Parameters of HZDR RPC prototypes with $\text{Si}_3\text{N}_4/\text{SiC}$ electrodes . . . . .   | 55  |
| 4.2. | Parameters for four different $\text{Al}_2\text{O}_3$ ceramic RPC prototypes . . . . .   | 59  |
| 5.1. | List of the scintillating sizes and purposes for detectors used in the RPC<br>test system . . . . .                                      | 72  |
| 5.2. | Beam dimensions measured with a fiber hodoscope for two different beam<br>rates . . . . .  | 74  |
| 5.3. | Comparison of the beam dimensions measured with scintillators and RPC .  | 77  |
| A.1. | Values for $\langle R \rangle$ normalized to $R_0$ as calculated by eq. (A.5) and eq. (A.8) for<br>different integration limits. . . . . | 104 |





# Erklärung

Hiermit versichere ich, dass ich die vorliegende Arbeit ohne unzulässige Hilfe Dritter und ohne Benutzung anderer als der angegebenen Hilfsmittel angefertigt habe; die aus fremden Quellen direkt oder indirekt übernommenen Gedanken sind als solche kenntlich gemacht. Die Arbeit wurde bisher weder im Inland noch im Ausland in gleicher oder ähnlicher Form einer anderen Prüfungsbehörde vorgelegt.

Alejandro Laso García  
20. Juli 2014